

**Variability, Symmetry, and Dynamics in Human Rhythmic  
Motor Control**

by

M. Mert Ankarali

A dissertation submitted to The Johns Hopkins University in conformity with the  
requirements for the degree of Doctor of Philosophy.

Baltimore, Maryland

April, 2015

© M. Mert Ankarali 2015

All rights reserved

# Abstract

How humans and other animals control rhythmic behaviors, and locomotion in particular, is one of the grand challenges of neuroscience and biomechanics. And yet remarkably few studies address the fundamental control-systems modeling of locomotor control. This thesis attempts to address several pieces of this grand challenge through the development of experimental, theoretical, and computational tools. Specifically, we focus our attention on three key features of human rhythmic motor control, namely *variability*, *symmetry*, and *dynamics*.

*Variability:* Little is known about how haptic sensing of discrete events, such as heel-strike in walking, in rhythmic dynamic tasks enhances behavior and performance. In order to discover the role of discrete haptic cues on rhythmic motor control performance, we study a virtual paddle juggling behavior. We show that haptic sensing of a force impulse to the hand at the moment of ball-paddle collision categorically improves performance over visual feedback alone, not by regulating the rate of convergence to steady state, but rather by reducing cycle-to-cycle variability.

*Symmetry:* Neglecting evident characteristics of a system can certainly be a mod-

## ABSTRACT

eling convenience, but it may also produce a better statistical model. For example, the dynamics of human locomotion is frequently treated as symmetric about the sagittal plane for modeling convenience. In this work, we test this assumption by examining the statistical consequences of neglecting (or not) bilateral asymmetries in the dynamics of human walking. Indeed, we show that there are statistically significant asymmetries in the walking dynamics of healthy participants ( $N=8$ ), but that by ignoring these asymmetries and fitting a symmetric model to the data, we arrive at a more consistent and predictive model of human walking.

*Dynamics:* Rhythmic hybrid dynamic behaviors can be observed in a wide variety of biological and robotic systems. Analytic (white-box) modeling tools of such systems are limited to the case when we have a full (and preferably simple) mathematical model that can accurately describe the system dynamics. In contrast, data-driven (block-box) system identification methods have the potential to overcome this fundamental limitation and could play a critical role in describing and analyzing the dynamics of rhythmic behaviors based on experimental data. And yet few tools exist for identifying the dynamics of rhythmic systems from input–output data. In this context, we propose a new formulation for identifying the dynamics of rhythmic hybrid dynamical systems around their limit-cycles by using discrete-time harmonic transfer functions.

Primary Reader: Noah J. Cowan

## ABSTRACT

Secondary Reader: Marin Kobilarov, and Tim Kiemel

# Acknowledgments

I think, I should start my acknowledgments from the time in which I had (hard) reset my academic clock (which was about to die), i.e. the day I first met with Prof. Uluc Saranli. It is highly possible that I wouldn't be writing my PhD dissertation today, if I had not met with him. I really thank Uluc for inspiring me with his endless energy and enthusiasm throughout the years that we have worked together. His vision, guidance, and energy helped me rediscover the passion and creativity that I had lost before, and my academic clock started ticking again.

Now let's move on to my Hopkins (i.e. PhD) journey. 2010 was a crazy and amazing year for me and my wife. When I go back to those days, I'm really proud that we survived well among all that rush. It was the year we got married (which is the first of the two best things ever happened in my life, for the second I had to wait 4 more years), and we had moved to Baltimore for starting our new journey; a new city, a new country, and a new life.

Obviously, throughout my PhD journey most influential person has been my adviser Prof. Noah Cowan. He has been an extraordinary adviser, mentor, and colleague

## ACKNOWLEDGMENTS

to me. His vision, passion, and most importantly belief in me (more than the one on myself) transformed me into a different level as a scientist that was above my expectations. Every time that I told him the phrases such as *can't*, *impossible*, *too hard*, he always objected me and forced me to be positive. I really thank Noah for his time, support, and encouragement during my years at Hopkins. He really helped me to pursue my dreams and he even pushed me to a level that is beyond my dreams.

Of course, I also got tremendous amount of extra support from a select group of people technically, scientifically, and mentally. First of all, I would like to thank to our collaborators Allison Okamura, Amy Bastian, and Tim Kiemel whose vision, ideas, and support made this dissertation possible. I would also like to thank my thesis committee Amy Bastian, Marin Kobilarov, and Tim Kiemel for their valuable comments and discussions.

I would also like to give my special thanks to my LIMBS lab friends, past and present, Alican Demir, Erin Sutton, Manu Madhav, Robert Nickl, Ravikrishnan Jayakumar, Sarah Stamper, Eric Tytell, John Swensen, and Eatai Roth. I would also like to thank my friends in LCSR and Mechanical Engineering Department, especially to Berk Gonenc, Tutkun Sen, Osman Yogurtcu, and Jonathan Bohren. My life has been much easier and more fun with my friends in Baltimore.

I would like to express my sincere gratitude to the Siebel Foundation for selecting me to join their exceptional community and awarding me with their prestigious Siebel scholarship. This award once again reminded me that I'm on the right track towards

## ACKNOWLEDGMENTS

achieving my goals.

I also thank to my family, my loving mother (Sevinc Ankarali), Orhan Beser, Sevgi Hasturk, and Selcuk Hasturk for their love, support, and encouragement throughout the years that we were far away from them. I can not even imagine how hard it would be to be far away from your kids for such a long time.

Finally, but forever I owe my loving thanks to my wife, Ela Ankarali, and our lovely daughter Ezgi Piril Ankarali whose birth is the second of the two best things happened in my life. My wife deserves every bit of praise regarding my accomplishments as a PhD candidate. I don't think there is another person in this world who would support me, love me, and make the same sacrifices for me as she did during my years at Hopkins. She has been an amazing wife and friend to me, I am extremely lucky to be married with such a magnificent lady.

# Dedication

*to my beloved wife, Ela Ankarali, and lovely daughter, Ezgi Piril Ankarali*

# Contents

<b>Abstract</b>	<b>ii</b>
<b>Acknowledgments</b>	<b>v</b>
<b>List of Tables</b>	<b>xiv</b>
<b>List of Figures</b>	<b>xv</b>
<b>1 Introduction</b>	<b>1</b>
1.1 Modeling Rhythmic Behaviors . . . . .	2
1.2 Thesis Organization . . . . .	5
1.2.1 Variability . . . . .	5
1.2.2 Symmetry . . . . .	6
1.2.3 Dynamics . . . . .	6
<b>2 Haptic Feedback Reduces Rhythmic Variability</b>	<b>8</b>
2.1 Introduction . . . . .	9

# CONTENTS

2.1.1	Juggling as a Model System in Neuroscience and Robotics . . .	12
2.1.2	Dissemination . . . . .	14
2.2	Materials and Methods . . . . .	15
2.2.1	Experiments . . . . .	16
2.2.2	Experimental Setup and Virtual Reality Implementation . . .	17
2.2.2.1	Experimental Apparatus . . . . .	17
2.2.2.2	Mechanical System Model and Virtual Reality Imple- mentation . . . . .	18
2.2.3	Task Performance . . . . .	22
2.2.4	Nominal Behavior and Nominal (Open-loop) Stability . . . . .	24
2.2.5	Closed-Loop System Identification . . . . .	28
2.2.6	Mean First Passage Time . . . . .	30
2.3	Results . . . . .	37
2.3.1	Subjects Believe Haptic Feedback Improves Their Performance	37
2.3.2	Haptic Feedback Improves Performance . . . . .	37
2.3.3	Nominal Stability is Fragile and Unchanged by Haptic Feedback	39
2.3.4	Closed-Loop Eigenvalues are Stable, but Unchanged by Haptic Feedback . . . . .	41
2.3.5	Haptic Feedback Improves Mean First Passage Time . . . . .	43
2.4	Discussion . . . . .	47
2.4.1	Stability: Convergence or Persistence? . . . . .	47

## CONTENTS

2.4.2	Sensing of Hybrid Transitions for State Estimation . . . . .	52
2.4.3	“Perfect-Time” Control . . . . .	55
<b>3</b>	<b>Walking dynamics are symmetric (enough)</b>	<b>57</b>
3.1	Introduction . . . . .	58
3.1.1	Limit-Cycle Dynamics and Symmetry . . . . .	61
3.1.2	Dissemination . . . . .	62
3.2	Methods . . . . .	62
3.2.1	Kinematic Data . . . . .	63
3.2.2	Events and Section Data . . . . .	66
3.2.3	Fitting Section Maps . . . . .	69
3.3	Statistical Approach . . . . .	70
3.3.1	Extending Monte Carlo Cross-Validation . . . . .	70
3.4	Results . . . . .	76
3.4.1	Symmetric vs. Asymmetric Modeling . . . . .	78
3.4.1.1	Step Maps . . . . .	78
3.4.1.2	Stride Maps . . . . .	79
3.4.1.3	Model Uncertainty . . . . .	81
3.4.2	Step Return Maps vs. Stride Return Maps . . . . .	83
3.5	Discussion . . . . .	84
<b>4</b>	<b>System Identification of Rhythmic Systems</b>	<b>89</b>

## CONTENTS

4.1	Introduction . . . . .	90
4.1.1	Dissemination . . . . .	93
4.2	Hybrid Dynamical System Formulation with Exogenous Input . . . . .	93
4.3	Mapping Between Poincaré Sections . . . . .	96
4.4	Harmonic Transfer Functions (HTF) for LDTP Systems . . . . .	99
4.5	Identification of HTF of LDTP Systems . . . . .	101
4.5.1	Identification via Single Cosine Inputs . . . . .	101
4.5.2	Identification via Sums of Cosine Inputs . . . . .	103
4.6	Results and Discussion . . . . .	106
4.6.1	Example Model System . . . . .	106
4.6.2	Phase Coordinates and Set of Poincaré Sections . . . . .	108
4.6.3	Simulation Results . . . . .	109
4.6.3.1	Non-parametric Harmonic Transfer Functions . . . . .	109
4.6.3.2	Phase Coordinates Affect Zeros, not Poles . . . . .	111
4.6.3.3	Estimation of Poincaré Return Map Eigenvalues . . . . .	111
<b>5</b>	<b>Conclusion</b>	<b>116</b>
<b>A</b>	<b>Appendix for Chapter 2</b>	<b>119</b>
A.1	Virtual Versus Physical Paddle Juggling . . . . .	119
A.2	Causal vs Non-causal Impact Acceleration Estimation . . . . .	121
<b>B</b>	<b>Appendix for Chapter 3</b>	<b>124</b>

## CONTENTS

B.1	Verification of Results by Extended Leave-One-Out (LOO) Bootstrap	124
B.2	Results for LOO Bootstrap . . . . .	128
B.2.1	Symmetric vs Asymmetric Modeling . . . . .	128
B.2.2	Step Return Maps vs. Stride Return Maps . . . . .	130
	<b>Bibliography</b>	<b>133</b>
	<b>Vita</b>	<b>158</b>

# List of Tables

2.1	Notation in Chapter 2 . . . . .	19
2.2	Mean impact accelerations ( $\ddot{p}_{\text{impact}}$ [m/s <sup>2</sup> ]) in different studies . . . . .	40
2.3	Eigenvalues of the Nominal Behavior . . . . .	41
3.1	Catalog of normal, $\mathcal{N}$ , and associated mirrored, $\mathcal{M}$ , datasets combinations used in our extended CV analysis. . . . .	75
B.1	Percentage decrease of model uncertainty when using symmetric modeling (and therefore doubling the data set). . . . .	130
B.2	Percentage increase in prediction error when using stride maps instead of step maps. . . . .	131

# List of Figures

1.1	<b>Illustration of a stable smooth 3D rhythmic dynamical system.</b> The black closed orbit is the limit cycle of the system. The two-dimensional cross-section illustrate a Poincaré section. The red curve represents a sample trajectory starting from an initial condition located at $\Sigma$ . As illustrated in the figure, the trajectory converges to the limit cycle. . . . .	4
2.1	<b>Virtual paddle juggling using a haptic interface.</b> The one-degree-of-freedom (1-DOF) haptic device measures the vertical displacement of a subject's hand, and uses this to control the position of a virtual paddle. A ball is rendered to the computer screen. When the ball strikes the paddle, a brief force impulse can be provided depending on the experimental condition. The goal is to bounce the ball (gray circle) under the influence of gravity so that it reaches apex (bold plus sign) within a goal region (between the parallel horizontal lines) using a virtual paddle (horizontal rectangle). . . . .	15
2.2	<b>Sample data obtained with our experimental setup.</b> Paddle and ball trajectories are depicted as solid and dotted curves, respectively. Users were instructed to maintain the ball within the goal region (gray). The initial apex of the ball is outside the goal region for this illustrative example (in experiments, the first apex was set to the middle of the goal region). But, the user achieves successful rhythmic juggling within $t \approx 3$ s and maintains this throughout the trial. . . . .	16

LIST OF FIGURES

2.3 **Haptic feedback does not enhance nominal stability.** (A) Impact acceleration statistics of each individual. Markers and error bars indicate the means and standard deviations. (B) Combined statistics of impact accelerations based on grouping the mean impact acceleration of each individual with respect to haptic condition. Shaded light gray region in both figures illustrates the open-loop stable trajectories according to (2.3) for  $\alpha = 0.8$ . Haptic and no haptic feedback conditions are depicted by solid gray and hollow black markers respectively. . . . . 26

2.4 **Passage time and computational modeling for MFPT.** (A) Data from a single example trial (not used for analysis) showing the ball height (dark gray) paddle height (light gray). Four cycles (five consecutive apex heights) are shown (filled circles at peaks of ball height). Here, the user failed to keep the apex height of the ball within the goal region at the fourth cycle. Accordingly, passage time (# of cycles) for this trial was 4. (B) Discretization process for model-based MFPT computation. We discretized the state space (apex height of the ball) into a finite set of representative states (bins). By convention the first state was assigned to the whole failure region (shown in light gray). Thus for our juggling paradigm, the first state corresponds to apex heights that lie above or below the goal region. All other states are equally spaced within the goal region. 50 bins were used to compute the MFPT; increasing the number of bins to 100 produced negligible differences in numerical values (less than 0.01%) . . . . . 31

2.5 **Haptic feedback enhances performance.** Performance in two metrics PO (Percentage of outlier apex heights, hollow markers) and CV (coefficient of variation, solid markers), was significantly improved with haptic feedback; larger values of these metrics indicate inferior performance. Each marker compares the performances (based on one of the metrics) of a single individual for the two haptic conditions. Performance was enhanced by haptic feedback for points lying below the 45° line. . . . . 38

2.6 **Haptic feedback does not enhance closed-loop eigenvalues.** The closed-loop eigenvalues identified from experiments with and without haptic feedback are not significantly different. Each marker on the figure corresponds to an individual's closed-loop eigenvalues without (abscissa) and with (ordinate) haptic feedback. 45° line indicates ideal agreement in eigenvalues of conditions with and without haptic feedback. . . . . 42

LIST OF FIGURES

2.7 **Direct and model-based MFPT estimates agree.** Markers indicate the MFPT estimates (the horizontal axis is model-based, and the vertical axis is direct estimation—see Methods) for all users and both haptic conditions (with and without haptic timing cue). The 45° solid black line would indicate ideal agreement between direct and model-based MFPT estimation. Vertical and horizontal error bars indicate the 95% confidence bounds for the direct and model-based MFPT estimates, respectively. . . . . 44

2.8 **Haptic feedback enhances metastability (MFPT).** Markers indicate the MFPT values without (horizontal axis) and with (vertical axis) haptic feedback. Direct and model-based MFPT estimates are depicted by solid light gray and hollow dark gray markers respectively. 46

2.9 **Simplified schematic representation of juggling behavior with different hypotheses on the role of haptic feedback.** Dashed lines represent (slow) parametric or “structural” tuning of the dynamics. Solid lines represent (fast) dynamical signals.  $z$  and  $\hat{z}$  represent the actual and estimated (continuous and discrete) states of the dynamics, respectively.  $u$  is the control input to the juggling dynamics which is regulated by the feedforward and feedback controllers. In principle, haptic sensing information could be used for tuning or regulation of feedforward (nominal) motor patterns (dashed light gray line), regulation of feedback controllers (dashed dark gray line) and/or state estimation (solid line). We found that neither the feedforward pattern nor the feedback gains were altered by the presence of haptic feedback. This suggests that haptic feedback serves mostly a state-estimation-like role that reduces uncertainty, thus improving performance in paddle juggling. . . . . 49

2.10 **Reducing noise is more effective for increasing MFPT than regulating eigenvalues.** The MFPT is shown as a function of the eigenvalue and uncertainty of a scalar stochastic dynamical system with additive white Gaussian noise (see Eq. (2.7)). Upper and lower failure limits are symmetric with respect to the origin. Uncertainty is measured in the form of a normalized standard deviation, which is computed by dividing the standard deviation by the size of the goal region ( $b_{\max} - b_{\min}$ ). Darker means more stable (i.e. higher MFPT) in the contour plots. . . . . 52

LIST OF FIGURES

3.1 **Visualization of leg angle vector  $\theta$ .** The left leg (blue) and right leg (red) alternate between stance and swing phase over the course of a stride. The variables  $\theta_{fL}$ ,  $\theta_{aL}$ ,  $\theta_{kL}$ , and  $\theta_{hL}$  correspond to the left foot, ankle, knee, and hip angles respectively. The corresponding right leg angles,  $\theta_{fR}$ ,  $\theta_{aR}$ ,  $\theta_{kR}$ , and  $\theta_{hR}$ , are not labeled. The 8 leg angles and their respective angular velocities form the 16-dimensional state vector. 65

3.2 **Types of input–output pairs analyzed in this thesis.**  $L$  and  $R$  represent the Poincaré sections associated with heel-strike events of the left and right legs. (a) Left-to-right step maps (top) and right-to-left step maps (bottom). Step maps are denoted using straight arrows. (b) Left-to-left stride maps (top) and right-to-right stride maps (bottom). Stride maps and step maps are distinguished throughout the thesis by shape (straight versus curved arrows, respectively). . . . . 68

3.3 **Illustration of the subsets  $\mathcal{V}$ ,  $\mathcal{F}_{\text{NCV}}$ ,  $\mathcal{F}_{\text{MCV}}$ , and  $\mathcal{F}_{\text{CCV}}$  after random splitting during an iteration of extended cross validation methods.** The normal dataset,  $\mathcal{N}$ , is randomly split into the normal training set  $\mathcal{F}_{\text{NCV}}$  and the common test set  $\mathcal{V}$ .  $\mathcal{F}_{\text{MCV}}$  shares the same indices as  $\mathcal{F}_{\text{NCV}}$  but is drawn from the mirrored dataset,  $\mathcal{M}$ . The training set for the CCV is simply the union of the other two training sets:  $\mathcal{F}_{\text{CCV}} = \mathcal{F}_{\text{NCV}} \cup \mathcal{F}_{\text{MCV}}$ . Note that the subset  $\mathcal{M} \setminus \mathcal{F}_{\text{MCV}}$  (greyed out) is not used in any of the three CV computations. . . . . 76

3.4 **Illustration of extended CV dataset partitioning.** (a) For step-to-step data, the normal dataset ( $\mathcal{N}$ ) comprises all left-to-right step ordered pairs, whereas the mirrored dataset ( $\mathcal{M}$ ) comprises all right-to-left step ordered pairs. (b) For stride-to-stride data, the normal dataset ( $\mathcal{N}$ ) comprises all left-to-left stride ordered pairs, whereas the mirrored dataset ( $\mathcal{M}$ ) comprises all right-to-right stride ordered pairs. In both cases, for each iteration, a common test set ( $\mathcal{V}$ , green arrows), used for all CV methods, is randomly sampled from the normal dataset. The training sets, however, are unique to each method. NCV: the remainder of the normal dataset is used for training ( $\mathcal{F}_{\text{NCV}}$ , blue arrows). MCV: the training set ( $\mathcal{F}_{\text{MCV}}$ , red arrows) is obtained using the same indices (dashed lines) as for  $\mathcal{F}_{\text{NCV}}$ . CCV: the union of the test sets for NCV and MCV, comprise the combined training data ( $\mathcal{F}_{\text{CCV}} = \mathcal{F}_{\text{NCV}} \cup \mathcal{F}_{\text{MCV}}$ , red and blue arrows). . . . . 77

LIST OF FIGURES

3.5 **Walking is asymmetric, but neglecting this can nevertheless improve fitting.** (a) Step-to-step maps. At all speeds, the mean mirrored cross validation errors (light grey diamonds) were significantly worse than for normal cross validation, indicating that steps were indeed asymmetric. Despite this left–right asymmetry, the mean combined cross validation errors were not significantly different than for normal cross validation at the two fastest walking speeds tested, and, more surprisingly, were actually *lower* at the slowest walking speed. The slopes of the fitted lines (dashed) determine the relative increase ( $m > 1$ ) or decrease ( $m < 1$ ) in CV error relative to the NCV error. (b) Stride-to-stride maps. By the same statistical measure, strides were also asymmetric at all speeds, but less substantially so. Moreover, the mean CCV error was lower than mean NCV error at all speeds. . . . 80

3.6 **Model uncertainty at all three speeds was lower when symmetry was assumed in both (A) step-to-step and (B) stride-to-stride maps.** Each marker compares the model uncertainty with asymmetry and with symmetry of a single individual. Dashed line denotes the best fitted line (passing through the origin) to the comparison markers. The percentage improvement is given by  $(1 - m) \times 100$ , where  $m$  is the slope of the fitted line. . . . 83

3.7 **Illustration of the CCV errors of step return maps and stride return maps.** Each marker compares the CCV errors of step and stride return maps of a single individual. Dashed lines illustrate the best fitted lines (passing through the origin) to the comparison markers with  $m$  being the associated slope of the line. . . . 85

4.1 **Illustration of a stable rhythmic hybrid dynamical system with two charts, i.e.  $\mathcal{I} = \{0, 1\}$ .** For simplicity, each chart has the same dimension, and is a subset of  $\mathbb{R}^3$ . The limit cycle of the system (black) is discontinuous. The two-dimensional surface (green) illustrates a hybrid transition (patch) boundary in which the transition is continuous (no jump in continuous variables of the state space) but not necessarily differentiable. The pair of surfaces (purple) connected by dashed lines illustrate a hybrid transition boundary in which the transition is discontinuous. The two-dimensional cross-sections (grey) illustrate the  $N$  Poincaré sections chosen by the experimenter. (These can be the hybrid boundaries, but in this example are chosen not to be.) The red curve represents a sample trajectory starting from an initial condition located at  $\Sigma_0$ . As illustrated in the figure, in the absence of external inputs trajectory converges to the limit cycle. . . . 113

4.2 **Schematic of the hopper model** . . . . 114

LIST OF FIGURES

4.3 **Non-parametric estimates of  $|H_0(z)|$ ,  $|H_1(z)|$  and  $|H_{-1}(z)|$ .** Magnitude plots in the top row (A, B, and C) represents the HTFs between the input and  $\delta y_M$ , where as bottom row (D, E, and F) belongs to the HTFs between the input and  $\delta \dot{y}_M$ . First (A and D), second (B and E) and third column (C and F) represents the HTFs where the phase coordinates are selected using isochrons, kinematic phase I, and kinematic phase II respectively. . . . . 114

4.4 **Non-parametric and parametric estimates of  $|H_0(z)|$ s.** Figures in the top row indicates the magnitude plots, where as the ones in the bottom row indicates the phase plots. Green and red curves represents the magnitude and phase plots for the HTFs from input to  $\delta y_M$  and from input to  $\delta \dot{y}_M$  respectively. Black curves the magnitude and phase plots of the estimated parametric transfer functions. First (A), second (B), and third column (C) represents the HTFs where the phase coordinates are selected using isochrons, kinematic phase I, and kinematic phase II respectively. . . . . 115

A.1 **Non-causal filtering biases the estimate of impact acceleration with haptic feedback.** Markers indicate estimated impact accelerations (abscissa and ordinate belong to causal and non-causal estimates, respectively). Hollow dark markers and solid light markers correspond to scenarios without and with haptic feedback, respectively. The 45° solid black line would indicate ideal agreement between causal and non-causal estimates. . . . . 123

B.1 **We reach the same conclusion if compare bootstrap based results, illustrated in this figure, and cross-validation-based results, illustrated in Fig 3.5.** Walking dynamics is statistically asymmetric, but neglecting this by training a model on the combined data can nevertheless improve statistical performance. (a) Step-to-step maps. At all speeds, the mean mirrored LOO bootstrap errors (light grey diamonds) were significantly worse than for normal cross validation, indicating that steps were indeed asymmetric. Despite this left–right asymmetry, the mean combined LOO bootstrap errors are significantly *lower* at all speeds. The slopes of the fitted lines (dashed) determine the relative increase ( $m > 1$ ) or decrease ( $m < 1$ ) in LOO Bootstrap error relative to the Normal LOO Bootstrap error. (b) Stride-to-stride maps. By the same statistical measure, strides were also asymmetric at all speeds, but less substantially so. Moreover, the mean CLB error was lower than mean NLB error at all speeds. . . . 132

# Chapter 1

## Introduction

The fundamental objective of this thesis is to discover the rules by which the human nervous systems controls rhythmic dynamic behaviors—and locomotion in particular. Addressing this grand challenge in neuroscience and biomechanics is critical in the long term since it will provide a foundation on which to build new locomotor rehabilitation techniques, neural prosthetic interface designs, engineered systems for (forceful) human-computer interaction, and robust bio-inspired engineering systems.

Human locomotion emerges from a control system: a nervous system connected to a body via muscles and sensors, all operating in closed loop. Few studies address the fundamental control-systems modeling of rhythmic motor control in humans. On the other hand, there is a long history of modeling of human motor control in the context of goal-directed tasks [81, 156]. Locomotion is not a point-to-point movement, and so, while some insight may certainly extend from the static to the rhythmic, we

## CHAPTER 1. INTRODUCTION

know little about the human rhythmic motor control from a computational point of view [138].

Locomotion is essential for quality of life of individuals suffering from motor deficits, and yet it is clear that there is a scientific void in our computational understanding of this fundamental scientific problem. Towards this ultimate goal, I address three important aspects—variability, symmetry, and dynamics—in human rhythmic motor control through a combination of experimental, computational, modeling, and theoretical analyses. I formulate and test new metrics and methods to find the factors that influence the closed-loop neuromechanical system during rhythmic tasks the most.

### 1.1 Modeling Rhythmic Behaviors

In this thesis, the fundamental approach to analyzing and modeling rhythmic dynamic behaviors centers around treating the underlying behavior as a nonlinear rhythmic dynamical system operating around a stable attracting limit cycle. This type of modeling approach has been successful for robotic [2, 8, 33, 46] and biological systems, from the level of individual neurons to whole-organism behavior [10, 37, 62, 86, 129, 141]. A limit cycle is an *isolated* periodic orbit that is a solution to the equations governing the nonlinear dynamical system [72]. The term *isolated* means that all neighboring trajectories around periodic-orbit are not closed. A limit cycle

## CHAPTER 1. INTRODUCTION

is said to be stable if all trajectories in a sufficiently small neighborhood of the limit cycle converge to it. Fig. 1.1 illustrates a 3D stable (smooth) rhythmic dynamical system and its limit-cycle.

One of the most powerful and useful tools used in the analysis [2, 67], control [29, 71], and identification [9, 129] of rhythmic dynamic system is Poincaré theory. A Poincaré section,  $\Sigma$ , is a co-dimension 1 submanifold that is transverse to the flow of the dynamical systems. A Poincaré (return) map,  $P : \Sigma \rightarrow \Sigma$ , is obtained by integrating the flow from  $\Sigma$  back to itself [72, 86].

A return map reduces the continuous (or hybrid) dynamical system into a lower dimensional discrete-time system that describe the behavior in terms of cycle-to-cycle transitions. Many of the essential properties of the behavior are preserved by this discrete-time dynamical system [85]. The intersection of the limit cycle with the Poincaré section is an isolated fixed point of the return map. The limit cycle is asymptotically stable if and only if this fixed point is stable. Our second fundamental modeling approximation in this thesis is based on the Hartman-Grobman theorem (or linearization theorem), which states that local flow around any hyperbolic fixed point is homeomorphic to the one governed by its linearization around the fixed point itself. Thus, we assume that the dynamic behaviors that we analyze in this paper remain within a local region where the linear dynamics dominate, and we fit linear models to data on Poincaré sections to analyze different rhythmic human behaviors (i.e. juggling in Chapter 2 and walking in Chapter 3).

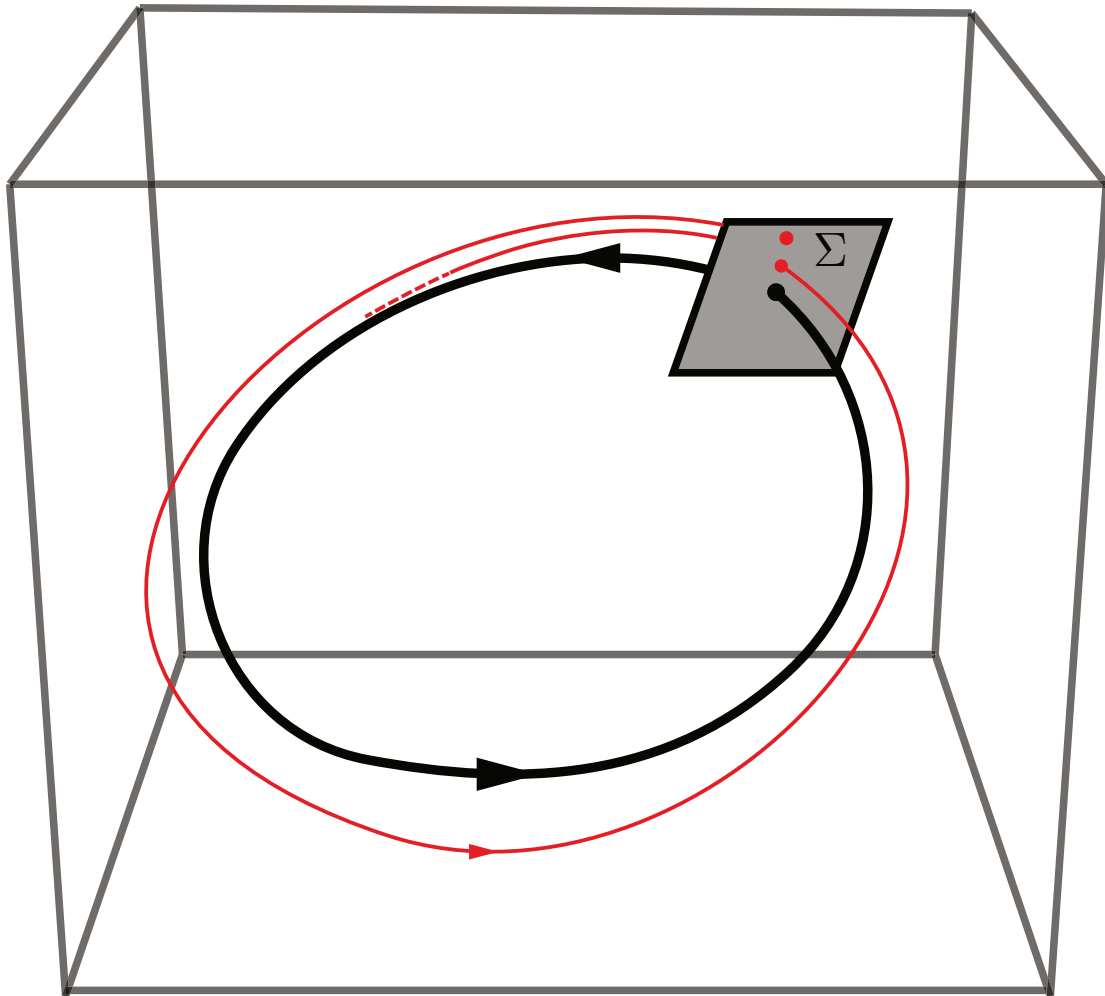


Figure 1.1: **Illustration of a stable smooth 3D rhythmic dynamical system.** The black closed orbit is the limit cycle of the system. The two-dimensional cross-section illustrate a Poincaré section. The red curve represents a sample trajectory starting from an initial condition located at  $\Sigma$ . As illustrated in the figure, the trajectory converges to the limit cycle.

## 1.2 Thesis Organization

In the following chapters, we examine three important features—variability, symmetry, and dynamics—of rhythmic motor control in humans. First, in Chapter 2, we explore the connection between haptic feedback and *variability* in rhythmic behaviors using a virtual “paddle juggling” experimental paradigm. Second, in Chapter 3, we analyze the statistical consequences of assuming or not bilateral *symmetry* during dynamic modeling of human walking. Finally, in Chapter 4, we introduce a new method for input–output system identification of the *dynamics* of rhythmic hybrid systems.

### 1.2.1 Variability

Little is known about how haptic feedback, particularly during discrete events, such as the heel-strike event during walking, enhances rhythmic behavior. To determine the effect of haptic cues on rhythmic motor performance, we investigate the integration of visual and haptic information during a “virtual paddle juggling” behavior. We show that the timing and state cues afforded by haptic feedback decrease the nervous system’s uncertainty of the state of the ball to enable more accurate control but that, to our initial surprise, the convergence rate of the the system to the steady-state is unaltered.

## 1.2.2 Symmetry

Dynamical systems modeling often involves neglecting certain characteristics of a physical system as a modeling convenience. For example, in the dynamics of locomotion, the musculoskeletal system is commonly treated as symmetric about the sagittal plane. But, to what extent are these modeling approaches “correct” (or at least “useful”)? We propose a new technique for evaluating the statistical consequences of assuming (or not) bilateral symmetry in locomotor systems that are “approximately” symmetric about the sagittal plane. We verify that there are statistically significant asymmetries in the dynamics of human walking, but nevertheless show that ignoring these asymmetries results in a more consistent and predictive model.

## 1.2.3 Dynamics

Rhythmic hybrid dynamic behaviors can be observed in a wide variety of biological and robotic systems. Powerful analytical and numerical tools exist in order to control and analyze such systems. Analytic (white-box) modeling tools are limited to the case when we have a full (and preferably simple) mathematical model that can accurately describe the system dynamics. On the other hand, input-output (black-box) system identification methods provide a powerful complement for modeling and analyzing general dynamical systems and they have been widely used for many engineering applications. However, few tools exist for identifying the dynamics

## CHAPTER 1. INTRODUCTION

of rhythmic systems from *input-output* data, and yet such methods could be very helpful in our understanding of human rhythmic motor control. In this context, we propose a new formulation for rhythmic hybrid dynamic systems using discrete time harmonic transfer functions that enables us to perform input-output system ID in the frequency domain.

## Chapter 2

# Haptic Feedback Reduces

# Rhythmic Variability

Stability and performance during rhythmic motor behaviors such as locomotion are critical for survival across taxa: falling down would bode well for neither cheetah nor gazelle. Little is known about how haptic feedback, particularly during discrete events such as the heel-strike event during walking, enhances rhythmic behavior. To determine the effect of haptic cues on rhythmic motor performance, we investigated a virtual paddle juggling behavior, analogous to bouncing a table tennis ball on a paddle. Here, we show that a force impulse to the hand at the moment of ball-paddle collision categorically improves performance over visual feedback alone, not by regulating the rate of convergence to steady state (e.g. via higher gain feedback or modifying the steady-state hand motion), but rather by reducing cycle-to-cycle (i.e.

steady state) variability. This suggests that the timing and state cues afforded by haptic feedback decreases the nervous system’s uncertainty of the ball’s state to enable more accurate control, but that the feedback gain itself is unaltered. This decrease in variability leads to a substantial increase in the mean first passage time, a measure of the long-term metastability of a stochastic dynamical system. Rhythmic tasks such as locomotion and juggling involve intermittent contact with the environment (i.e. hybrid transitions). Timing of such transitions is generally easy to sense via haptic feedback and potentially would be more precise than the one provided by visual feedback due to the significant delays in human vision. This additional precise timing information may improve metastability, equating to less frequent falls or other failures depending on the task.

## 2.1 Introduction

Terrestrial locomotion [86] and other rhythmic motor control tasks such as juggling [137] and finger tapping [169], often involve *hybrid transitions*, namely discrete changes in the contact configuration of the animal with its surrounding environment. There is important information conveyed in the timing of these transitions: a measurement of an early or late hybrid transition carries information about the state of the body and/or environment.

We hypothesize that providing sensory feedback to the nervous system regard-

ing the timing and state of these transitions can enhance motor control performance. Specifically, we investigate the role of haptic cues during virtual paddle “juggling”. A similar juggling paradigm has been extensively explored by Sternad and colleagues [130, 131, 137, 152, 162], laying the theoretical and experimental foundation upon which the current study is built. In a theoretical model of paddle juggling, Schaal et al. [137] showed that if the nominal motor pattern, measured in terms of the “average” periodic trajectory of the paddle during steady-state juggling, exhibits negative accelerations<sup>1</sup> at the time of ball–paddle collision, then the system would be open-loop stable; in other words, if the nominal paddle motion were replayed in open-loop (in a Gedankenexperiment), then small perturbations to the ball would diminish over time, and the ball would return, asymptotically, to its nominal bouncing height. This is often referred to as “open-loop stability” in the literature but this term is misleading because human hand motions are clearly *not* executed in an open-loop fashion. Indeed, the human paddle juggling behavior is a closed-loop system that relies on active sensory feedback (vision and haptic feedback). Both our own data and prior studies [130, 147, 148, 162, 163] support the fact that active sensory feedback plays a significant role in the human paddle juggling task. Thus, when referring to the stability of the nominal motor pattern, this thesis adopts the term *nominal stability*.

Sternad et al. [152] drew the intriguing conclusion that nominal stability seemed to improve in the presence of haptic feedback. To the best of our knowledge, this

---

<sup>1</sup>Note that the nominal paddle velocity at the time of impact still has to be positive (upward direction) for a successful limit-cycle behavior

## CHAPTER 2. HAPTIC FEEDBACK REDUCES RHYTHMIC VARIABILITY

observation—that a change in the availability of enriched sensory information causes subjects to adopt a different nominal pattern—has not been repeated in another behavior or in the same behavior by a different research group.

In the present study, we re-examine the role of haptic feedback in juggling. Our juggling task is virtual: users “juggle” by using this virtual paddle controlled via a haptic interface to repeatedly hit a virtual ball on a computer screen. The haptic timing cue is provided in the form of a brief mechanical impulse imparted to the subject’s hand via the haptic paddle.

We indeed confirmed that the haptic timing information improves juggling performance as previously reported, but we were unable to corroborate previous findings [152] that nominal stability depends on the availability of haptic information. More surprisingly, we also found no difference in the closed-loop convergence rate in the two haptic conditions. So, haptic feedback did not change the closed-loop “gain” nor the nominal pattern, contradicting previous findings. As described in the Discussion (See Section 2.4) and Appendix A, there are several possible reasons for this discrepancy, including the differences in the experimental setup between our work and that of Sternad et al. [152], although it appears likely that the difference arises from complexities in estimating paddle acceleration at impact (see Appendix). Irrespective of these differences, our results show that rhythmic motor performance can be enhanced due to a haptic timing cue, despite no apparent change to the nominal (“open-loop”) or closed-loop convergence rates.

How does haptic feedback improve performance without affecting either closed-loop or nominal convergence rate? In an effort to understand the closed-loop mechanism underlying the significant performance improvement haptic feedback affords over vision alone, we adopted a stability metric, the Mean-First-Passage-Time (MFPT), that incorporates not only the deterministic dynamics, but also the stochastic nature of the system [154]. This metric has been used to describe the long-term metastability of rhythmic locomotion of robotic systems [27]. There are two primary ways to improve metastability (that is, to increase the MFPT). One way is to decrease the noise, and the other is to increase the convergence rate. We illustrate later in this thesis that decreasing the noise (e.g. sensory or motor) can have a much more dramatic effect on improving the MFPT than quickening convergence.

If long-term metastability were enhanced by a haptic timing cue, despite no change in convergence rate, it would suggest that the haptic cue enhanced the estimate of the ball and paddle state, thus reducing the nervous system’s uncertainty. By contrast, increasing the feedback gain itself would increase the convergence rate.

### **2.1.1 Juggling as a Model System in Neuroscience and Robotics**

How animals control rhythmic behavior—such as locomotion and juggling—is one of the grand challenges in neuroscience. It has been examined at all levels of bio-

## CHAPTER 2. HAPTIC FEEDBACK REDUCES RHYTHMIC VARIABILITY

logical organization from individual ionic currents [44], to central pattern generating networks [90, 120], to whole-organism dynamics [86], and it has been analyzed using behavior [120], physiology [82], and modeling [37, 86].

Yet, detailed computational models of rhythmic motor behavior remain limited. Indeed, while the tools for this type of analysis are emerging [128, 129], they are still in their infancy. Perhaps more importantly, rhythmic motor behaviors may recruit different computational circuits than those used during discrete motor tasks [139]. Thus, it is essential to rigorously quantify rhythmic motor behavior and create models of such behaviors without assuming that lessons learned for discrete motions will apply.

Our main goal in this work is to understand the rules of rhythmic motor coordination. Terrestrial locomotion generally involves extremely complicated biomechanics, and even the simplest and most impoverished models are challenging to analyze [86, 140] and control [8, 29]. Yet, several studies on neuromechanical systems [34, 41, 83, 158] highlight the role of biomechanics in decoding the neural circuits that control locomotion. To overcome these challenges and to isolate neural systems from biomechanics, this chapter considers a virtual one-dimensional paddle juggling task, which has extremely simple mechanical dynamics compared to other tasks such as walking, running, or flying.

Juggling has been addressed from several perspectives, including nonlinear dynamics [32, 72, 86, 157], robotics and control [22, 23, 171], and human movement anal-

ysis [47, 118, 131, 147, 148, 162]. From the human movement analysis point of view, several researchers [130, 131, 137, 162, 163] have investigated the same simplified juggling task we consider here, in which a ball is stabilized in the air by hitting it upwards with a paddle. Despite its apparent simplicity, rhythmically bouncing a ball raises fundamental questions common to the study of general rhythmic movements (including walking). To rhythmically juggle a ball requires fine tuning of the movements of the hand in order to hit the ball with the appropriate velocity, at the right place, and at the right time. The result of successful juggling is a hybrid dynamical system that displays limit-cycle-like behavior, just as with walking. The wide interest in this behavior likely arises from its simplicity, experimental tractability, and relevance to neural control. Of course, this simplicity is relative as juggling can exhibit surprisingly complex behavior (thanks to its hybrid dynamic nature): Guckenheimer [72] showed that a ball bouncing on a periodically driven planar surface exhibits a wide variety of motions, including steady states, period bifurcations, strange attractors, and chaotic motion.

### 2.1.2 Dissemination

The work presented in Chapter 2 has been reported at several scientific meetings [11, 12], and in a journal paper [10]. Figures and the text in this chapter of the dissertation appeared in these publications.

## 2.2 Materials and Methods

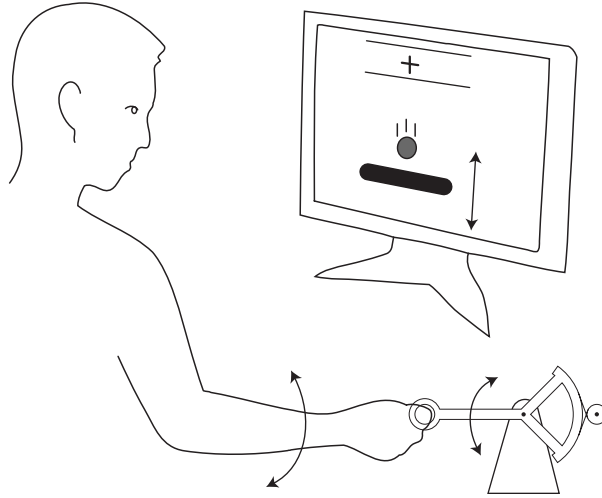


Figure 2.1: **Virtual paddle juggling using a haptic interface.** The one-degree-of-freedom (1-DOF) haptic device measures the vertical displacement of a subject’s hand, and uses this to control the position of a virtual paddle. A ball is rendered to the computer screen. When the ball strikes the paddle, a brief force impulse can be provided depending on the experimental condition. The goal is to bounce the ball (gray circle) under the influence of gravity so that it reaches apex (bold plus sign) within a goal region (between the parallel horizontal lines) using a virtual paddle (horizontal rectangle).

In order to analyze human motor control of a rhythmic behavior, we used a one-degree-of-freedom (1-DOF) haptic device and a virtual environment (Fig. 2.1) [10]. In our experiments, subjects manipulated a haptic paddle with their hand, causing a virtual paddle to move up and down on the computer screen and “juggled” by using this virtual paddle to repeatedly hit a virtual ball, much like bouncing a table tennis ball. The paddle and ball physics were simulated and conveyed to the participant haptically via force impulses at impact rendered with the 1-dof haptic interface and visually via rendered ball and paddle movement on a computer screen (Fig. 2.1). The

goal was to cause the ball to reach its apex between two horizontal lines. Example data acquired from this system is depicted in Fig. 2.2. In the Appendix A, we describe the rationale for using a virtual juggling setup over a physical juggling setup.

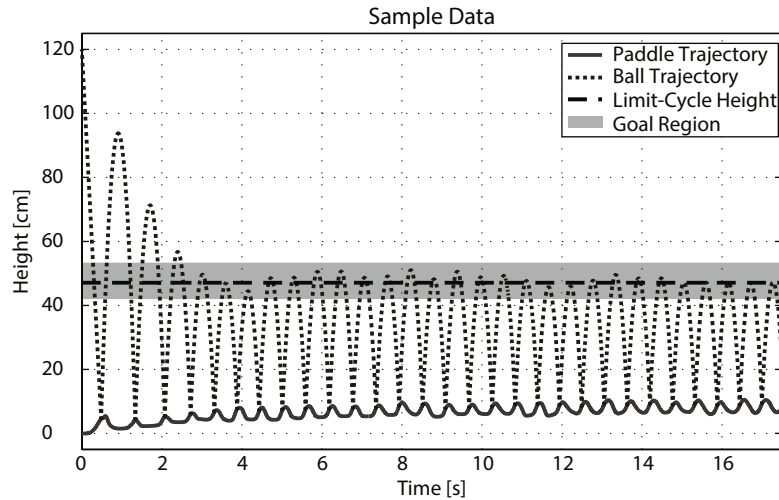


Figure 2.2: **Sample data obtained with our experimental setup.** Paddle and ball trajectories are depicted as solid and dotted curves, respectively. Users were instructed to maintain the ball within the goal region (gray). The initial apex of the ball is outside the goal region for this illustrative example (in experiments, the first apex was set to the middle of the goal region). But, the user achieves successful rhythmic juggling within  $t \approx 3$  s and maintains this throughout the trial.

## 2.2.1 Experiments

Eighteen college- and graduate-school-aged participants (2 Female, 16 Male) attempted to perform the given juggling task. The experiments were approved by the Johns Hopkins University Institutional Review Board (IRB). Each experiment consists of a demonstration session, four training sessions and two final data collection sessions. The duration of each session was 2.5 min. Between each session, participants

were given 30 sec rest to prevent fatigue.

During the demonstration session the experimenter explained how to use the haptic device to the participant and then performed a brief demonstration of the juggling task. For training and data collection sessions, we asked participants to bounce the ball so as to repeatedly cause the ball to reach its apex within the goal region. In training sessions, the subjects performed the task with and without haptic feedback based on a fixed order: 1) without haptic feedback, 2) with haptic feedback, 3) without haptic feedback, 4) with haptic feedback.

The purpose of the training sessions was to enable subjects acclimate to the environment and behavior. In the data collection sessions, one session was performed without haptic feedback and the other session was performed with haptic feedback. Half of the subjects started the data collection sessions without haptic feedback, and the other half started with haptic feedback.

### **2.2.2 Experimental Setup and Virtual Reality Implementation**

#### **2.2.2.1 Experimental Apparatus**

The haptic device measured the displacement of a user's hand, which was mapped to the position of the virtual racket on the screen. Depending on the experimental condition, the haptic paddle could simulate the virtual ball-paddle collision by pro-

## CHAPTER 2. HAPTIC FEEDBACK REDUCES RHYTHMIC VARIABILITY

viding a force impulse to the hand. The juggling paddle was coupled to a DC motor (A-max 26 Series–110170, Maxon Precision Motors, Inc., Fall River, MA) with a back-drivable capstan mechanism. Haptic force feedback was simulated via generating an impulsive torque to the motor shaft. In order to generate the desired torque on the DC motor, a PCI-DAS6014 DAQ card (Measurement Computing Corporation, Norton, MA 02766) is used for sending voltage commands to a current amplifier based on an OPA544 power op-amp (Texas Instruments, Inc., Dallas, Texas 75243) that drives the DC motor. The DC motor was also equipped with a HEDS 5540 quadrature laser encoder (Avago Technologies US Inc., San Jose, CA) which was used for measuring the rotation in the motor shaft. In order to read the encoder inputs a PCI-QUAD04 encoder card (Measurement Computing Corporation, Norton, MA 02766) is used. The virtual reality part of the system was developed in the C# programming language environment (Microsoft Corporation, Redmond, WA 98052), and the loop rate of the whole system was 1 kHz.

### **2.2.2.2 Mechanical System Model and Virtual Reality Implementation**

Paddle juggling, like many other rhythmic dynamic tasks, is a hybrid dynamical system. Roughly speaking, a hybrid dynamic system is one for which smooth dynamics are punctuated with discrete “jumps” triggered by threshold functions [76]. In this context, we divide the ball dynamics into two parts: a continuous flight phase

Table 2.1: Notation in Chapter 2

Parameter	Units	Description
System parameters		
$g$	$\text{m/s}^2$	Gravitational acceleration
$\alpha$		Ball-paddle coefficient of restitution
$b_{\max}$	m	Upper limit of goal region
$b_{\min}$	m	Lower limit of goal region
Continuous-time variables		
$t$	s	Time
$b$	m	Height of ball
$\dot{b}$	m/s	Velocity of ball
$\dot{b}^-$	m/s	Velocity of ball just before the collision
$\dot{b}^+$	m/s	Velocity of ball just after the collision
$p$	m	Position of paddle
$\dot{p}$	m/s	Velocity of paddle
$\ddot{p}$	$\text{m/s}^2$	Acceleration of paddle
Discrete-time variables at specific events		
$k$		Index of apex events
$t_k$	s	Time of $k^{\text{th}}$ ball apex event
$b_{\text{apex}}[k]$	m	Apex height at $k^{\text{th}}$ cycle
$b_{\text{ss}}$	m	Steady-state value of ball apex height
$x[k]$	m	Deviation of ball apex height around steady-state
$\ddot{p}_{\text{impact}}$	$\text{m/s}^2$	Acceleration of paddle at collision

## CHAPTER 2. HAPTIC FEEDBACK REDUCES RHYTHMIC VARIABILITY

describing the dynamics of flight, and a discrete transition phase describing the state transitions due to collision between the paddle and the ball. Table 2.1 provides the notation we use throughout the chapter. Neglecting aerodynamic drag, flight dynamics of the ball take the form

$$\ddot{b} = -g, \tag{2.1}$$

subject to appropriate position and velocity initial conditions, where  $b$ ,  $\dot{b}$  and  $\ddot{b}$  denote the height, velocity and acceleration of the ball respectively. To implement the physics digitally on a computer, we discretized the continuous dynamics in (2.1). Let  $t_k$  denote the time of the  $k^{\text{th}}$  time step, and let

$$\mathbf{z}_k = \begin{bmatrix} b(t_k) \\ \dot{b}(t_k) \end{bmatrix}$$

denote a discrete-time state variable. Then,

$$\mathbf{z}_{k+1} = \begin{bmatrix} 1 & \Delta t_k \\ 0 & 1 \end{bmatrix} \mathbf{z}_k + \begin{bmatrix} -\frac{1}{2}g\Delta t_k^2 \\ -g\Delta t_k \end{bmatrix},$$

where  $\Delta t_k = t_{k+1} - t_k$  is the time between two sampling instants. In real ball-paddle dynamics, a collision event is triggered when the ball hits the paddle, which occurs

## CHAPTER 2. HAPTIC FEEDBACK REDUCES RHYTHMIC VARIABILITY

when the following conditions are satisfied:

$$b = p,$$

$$\dot{b} < \dot{p},$$

(where  $p, \dot{p}$  and  $\ddot{p}$  the height, velocity and acceleration of the paddle respectively)

which were approximated in discrete-time (to implement in virtual reality) as the

first discrete time,  $t_k$ , for which

$$b(t_k) < p(t_k),$$

$$\dot{b}(t_k) < \dot{p}(t_k).$$

The ball position and velocity were simulated and were therefore known to the numerical precision of the computer, but the paddle position and velocity were estimated in real time from optical encoder measurements. To estimate paddle velocity, encoder position data was low-pass-filtered and passed through a backward difference filter.

To model the discrete transition due to collision between the paddle and the ball, we assumed that the collisions were purely elastic and the mass of the paddle was infinite such that the paddle velocity was not affected by the collision. Based on these assumptions, using the coefficient of restitution rule, the discrete transition at

the collision instant was defined as

$$\begin{aligned} b^+ &= b^-, \\ \dot{b}^+ &= -\alpha\dot{b}^- + (1 + \alpha)\dot{p}, \end{aligned} \tag{2.2}$$

where  $\alpha$  is the coefficient of restitution. In the experiments with haptic feedback, we applied an impulsive force (short duration 10 ms, constant magnitude) proportional to the impact velocity to the haptic paddle,  $v_{\text{imp}} = \dot{p} - \dot{b}$ , (with a gain of 0.1 Ns/m) immediately after collision. We manually tuned the amplitude and duration of the haptic feedback in our preliminary analysis based on the authors' perception of the haptic experience, such that the haptic feedback was noticeable, natural, and within the capabilities of our haptic device hardware.

### 2.2.3 Task Performance

We asked the participants ( $N = 18$ ) of our experiment to keep the apex height of the ball within a goal region, and they performed the task both with and without haptic feedback. In order to ease the task for the participants, we displayed a plus sign showing the last apex height of the ball (Fig. 2.1). We also asked the participants their opinions about the difficulty level of completing the task with and without haptic feedback.

First, we analyzed the importance of haptic feedback based on two performance measures: percentage of outliers (PO) and coefficient of variation (CV). Percentage

## CHAPTER 2. HAPTIC FEEDBACK REDUCES RHYTHMIC VARIABILITY

of outliers corresponds to the percentage of apex heights that are not inside the goal region. Lower PO values indicate good performance. CV is the coefficient of variation of apex height values, which is found by dividing the standard deviation of the data set to the mean value and multiplying by 100. CV captures the variability of the behavior.

Since our goal was to study successful rhythmic juggling behavior, we excluded the unsuccessful experimental data. Two of the subjects were unable to produce successful rhythmic juggling regardless of haptic condition, and their performance was unacceptably poor in both cases for both metrics (PO values  $> 80\%$  and CV values  $> 60\%$ ). A third subject achieved stable juggling with haptic feedback (PO = 19.8% and CV = 6.2%), but this subject failed to produce successful rhythmic juggling without haptic feedback (PO = 70.2% and CV = 85.3%). Since this subject produced no useful data without haptic feedback, we excluded all of the subject's data from our statistical analysis (although this subject supports our general finding that haptic feedback enhances performance). As a result, we analyzed the data of 15 subjects.

## 2.2.4 Nominal Behavior and Nominal (Open-loop)

### Stability

Nominal stability, also called open-loop or passive dynamic stability, is an important concept in rhythmic dynamic behaviors [32, 48] and it has been analyzed extensively, especially for legged locomotion [62, 66, 67, 113].

In previous studies on paddle juggling behavior, researchers extensively investigated nominal (“open-loop”) stability [137, 152, 162, 163]: nominal stability in paddle juggling would imply that if the average motor pattern were recorded, and played repeatedly, then small errors in ball motion would diminish over time, even without sensory feedback. The open-loop juggling model initially introduced by Schaal et al. [137] requires that the paddle motion has to be strictly time periodic and the paddle has to hit the ball with an upward velocity. Under these conditions, ball bouncing becomes a nonlinear dynamical system, operating near a limit cycle [86]. One way to test for stability is to analyze the eigenvalues of the Poincaré return map [8, 69, 75]; if the eigenvalues all have magnitudes less than unity, then the system is (locally) asymptotically stable.

Schall et al. [137] showed that under the conditions described above, open-loop stability of the juggling pattern is guaranteed if and only if the acceleration of the

paddle at the impact ( $\ddot{p}_{\text{impact}}$ ) satisfies

$$-2g \frac{1 + \alpha^2}{(1 + \alpha)^2} < \ddot{p}_{\text{impact}} < 0. \quad (2.3)$$

In human subject trials with a physical (not virtual) paddle juggling system, Schaal et al. [137] and Sternad et al. [152] found that in fact subjects adopt impact accelerations that satisfy the constraint in (2.3), suggesting that paddle juggling is nominally stable. One major issue associated with negative impact acceleration is that it unavoidably creates a deviation from optimal nominal input effort (which is achieved at zero acceleration [152]). In other words, there is a trade-off between open-loop stability and nominal energetic cost. Previous results [137,152,162] suggest that humans sacrifice energetic optimality in order to achieve nominal stability.

In this study, we analyzed impact accelerations with and without haptic feedback (Fig. 2.3(A)). Previously, Sternad et al. [152] analyzed nominal stability during ball bouncing and also compared impact accelerations with and without haptic feedback ( $N = 3$  participants).

Let  $T$  denote the period of the nominal paddle trajectory. To analyze nominal stability, we only require characterization of the paddle trajectory in the vicinity of ball–paddle collision. For each impact time,  $t_k$ , we measured the paddle position over a 0.1s time interval,  $[t_k - 0.1s, t_k]$ . We applied a causal smoothing filter, `rlowess`, in Matlab (Mathworks Inc., Natick MA) to the paddle position data and estimated

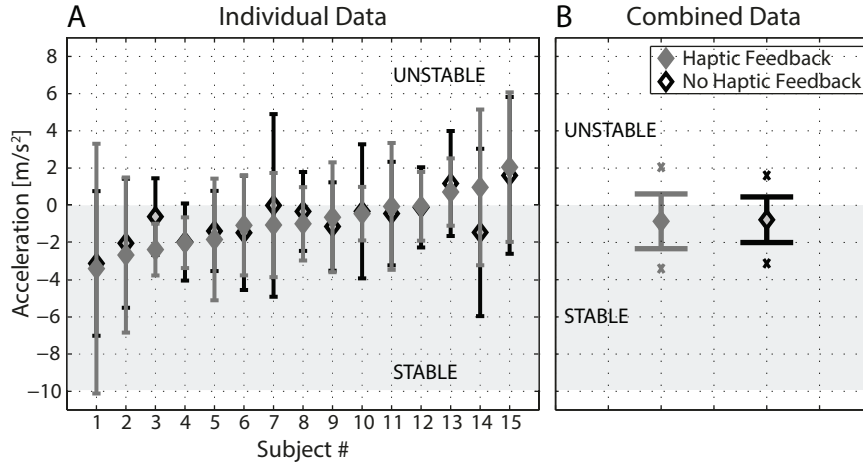


Figure 2.3: **Haptic feedback does not enhance nominal stability.** (A) Impact acceleration statistics of each individual. Markers and error bars indicate the means and standard deviations. (B) Combined statistics of impact accelerations based on grouping the mean impact acceleration of each individual with respect to haptic condition. Shaded light gray region in both figures illustrates the open-loop stable trajectories according to (2.3) for  $\alpha = 0.8$ . Haptic and no haptic feedback conditions are depicted by solid gray and hollow black markers respectively.

velocities using a central difference approximation. These velocity estimates were further smoothed (rlowess in Matlab).

After filtering, we fit a third-order polynomial to the smoothed velocity data:

$$v[\hat{t}] = a_0 + a_1\Delta t + a_2\Delta t^2 + a_3\Delta t^3, \quad (2.4)$$

$$\Delta t = t - t_k, \quad (2.5)$$

where  $a_0, a_1, a_2, a_3$  were the paddle trajectory polynomial coefficients, averaged across impacts within a single trial. In addition to limit-cycle analysis, we used these polynomials to derive the impact accelerations as described above.

## CHAPTER 2. HAPTIC FEEDBACK REDUCES RHYTHMIC VARIABILITY

As an alternative to this filtering and estimation method, one might have used simple non-causal linear filters (which have the benefit of introducing zero phase lag) to the paddle data for the experiments with haptic feedback [137, 152, 162, 163]. However, our analysis in the Appendix shows that the rapid negative force applied to the paddle at impact generated a small but significant negative acceleration, and non-causal filters therefore produced consistent biases to the velocity and acceleration estimates at the impact instant.

Computation of the limit cycle also required the period  $T$ . One possible estimation of the period would be the average of the elapsed times between successive impacts. However, this method produces estimates for the limit-cycle period that do not, in general, satisfy the constraint that the ball must have the same speed before and after impact, i.e.  $|\dot{b}^+| = |\dot{b}^-|$ . Enforcing this constraint, we computed the period of the limit cycle as

$$T = \frac{2(1 + \alpha)}{g(1 - \alpha)} \dot{p}_{\text{impact}}. \quad (2.6)$$

Open-loop stability based on the acceleration constraints from Equation (2.3) provides a categorical result—stable or unstable—not a graded measure of stability. Thus, we estimated the nominal (linearized) return-map eigenvalues that measure convergence (or divergence) rate of the limit cycle. In order to find eigenvalues, we first found the states of the system—paddle position, ball position, and ball velocity—at

the instant of impact. We numerically estimated the linearized return map (Jacobian matrix) by using a finite-difference approximation. The eigenvalues of this Jacobian matrix characterize nominal stability.

## 2.2.5 Closed-Loop System Identification

As explained in Section 1.1, we use Poincaré theory and assume that the closed-loop juggling behavior is a rhythmic dynamical system operating near a limit cycle. Thus, we fit a linear dynamical system model of the apex-to-apex dynamics as an estimate of the closed-loop linearized Poincaré return map. We assume that, in our experiments, subjects remain within a local region where the linear dynamics dominate. Based on our assumptions and motivations we fit a linear stochastic dynamical system—an auto regressive (AR) Gaussian model—to the apex height data for each subject and for each haptic condition. A first-order AR model takes the form

$$x[k] = ax[k - 1] + e[k] , \quad e[k] \sim \mathcal{N}(0, \sigma^2), \quad (2.7)$$

where  $x[k] = b_{\text{apex}}[k] - b_{ss}$  is the relative displacement of the ball apex height at time  $k$ , measured with respect to  $b_{ss}$ , the steady-state apex height. We estimated the parameters in ((2.7)) using least-squares that minimizes the following loss function

$$E = \sum_{k=1}^N \hat{e}[k]^2. \quad (2.8)$$

## CHAPTER 2. HAPTIC FEEDBACK REDUCES RHYTHMIC VARIABILITY

In addition to the first-order AR model in (2.7), we also tested zeroth- and second-order AR models and computed the loss functions in (2.8). Note that zeroth-order AR model simply treats the evolution of apex heights as a pure noise process centered around the nominal height. We compared the quadratic losses provided by both zeroth-, first- and second-order models, (i.e.  $E_0$ ,  $E_1$ , and  $E_2$ ), by evaluating the relative improvement at each order increase,  $100|E_{n+1} - E_n|/E_{n+1}$ , which must be traded off with the addition of extra parameters. The mean improvement of the first-order model with respect to zeroth-order model was substantial (20%), whereas the mean improvement of the second-order model with respect to the first-order model was negligible (2%). Thus we selected the first-order AR model for our data analysis. The order of the fitted model can also be considered as the dimension of the slow, template dynamics [61, 129] that emerge in the closed-loop behavior. The parameter  $a$  in (2.7) is the eigenvalue of the dynamics which measures convergence rate, namely the slowest time constant associated with recovery to equilibrium, one of the most common metrics for quantifying stability of dynamical systems.

Our fitted AR model is a “black-box” model that makes fewer assumptions than the open-loop juggling model by [137]. However since it is a linear model there could be nonlinear affects that can not be captured by our model. There could be nonlinear control strategies such as the “mirror law” [22] or robust hybrid stabilization [74]. However, we approximate the system in a local region around the goal, where the linear dynamics likely dominate.

## 2.2.6 Mean First Passage Time

Mean first passage time (MFPT) is a stability metric that incorporates time and stochasticity and has been recently applied to legged locomotion [27]. Recently Milton et al. [115,116] used MFPT to measure performance in a human balance control task and Venkadesan et al. [161] used MFPT in the context of a hand manipulation task; however these tasks are not rhythmic hybrid dynamical systems, thus our methods and approach regarding MFPT generally build more directly upon the derivations by Byl and Tedrake [27].

The MFPT is also referred to as the mean time between failures. For juggling, the passage time refers to the number of cycles until the apex of the ball fails to land in goal region; in the example depicted in Fig. 2.4(A), the passage time is 4 cycles because the ball apex first lands outside the goal region on the fourth successive cycle. Note that passage time in our task is a discrete random variable, unlike the interpretation in some previous studies [115,116,161], where passage time is measured in seconds and is a continuous random variable.

The MFPT metric is the probabilistic expectation of the passage time. Of course, this must be estimated from data. We propose two different estimation methods for the MFPT: estimation directly from failure events and estimation based on a stochastic dynamical model.

The first method is a direct statistical approach, which does not require a stochastic dynamical model for the system. For a given trial, we record all the observed

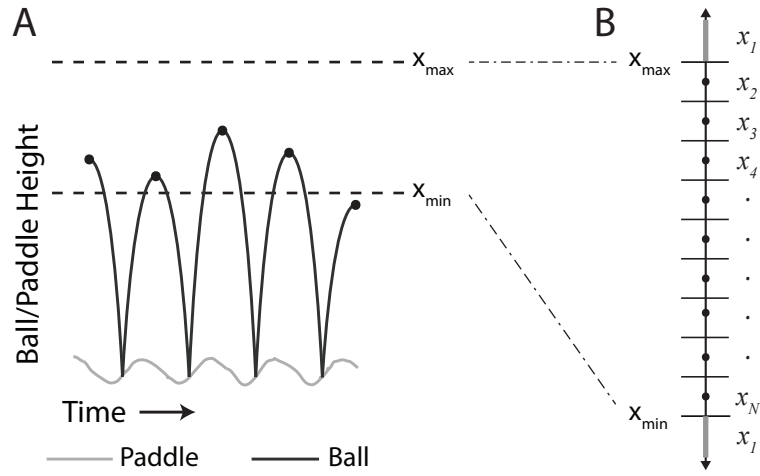


Figure 2.4: **Passage time and computational modeling for MFPT.** (A) Data from a single example trial (not used for analysis) showing the ball height (dark gray) paddle height (light gray). Four cycles (five consecutive apex heights) are shown (filled circles at peaks of ball height). Here, the user failed to keep the apex height of the ball within the goal region at the fourth cycle. Accordingly, passage time (# of cycles) for this trial was 4. (B) Discretization process for model-based MFPT computation. We discretized the state space (apex height of the ball) into a finite set of representative states (bins). By convention the first state was assigned to the whole failure region (shown in light gray). Thus for our juggling paradigm, the first state corresponds to apex heights that lie above or below the goal region. All other states are equally spaced within the goal region. 50 bins were used to compute the MFPT; increasing the number of bins to 100 produced negligible differences in numerical values (less than 0.01%)

## CHAPTER 2. HAPTIC FEEDBACK REDUCES RHYTHMIC VARIABILITY

passage times (times between failures). Let  $\{k_{p,1}, k_{p,2}, \dots, k_{p,N}\}$  be the set of observed passage times. Our goal is to estimate the MFPT,  $\mu_{\text{mfpt}}$ , from data. The sample mean of the data gives such an estimate:

$$\hat{\mu}_{\text{mfpt}} = \frac{1}{N} \sum_{i=1}^N k_{p,i}. \quad (2.9)$$

Assuming that passage times are independent and identically distributed geometric random variables, Equation (2.9) corresponds to the maximum likelihood estimate, namely  $\hat{\mu}_{\text{mfpt}} = E[\mu_{\text{mfpt}}]$ . Direct estimation via the sample mean in Equation (2.9) is simple, but may require many failures to obtain a low-variance estimate. Unfortunately, failure is often a rare event so this method may be impractical. Estimating mean time between falls in human locomotion, for example, would require waiting until subjects actually fall, which is challenging due to safety and other reasons. For our juggling experiments, the goal (hitting the ball to reach apex within a desired region) was designed so that subjects typically fail at least 2-3 times in a single experiment (often more). However, there are many trials for which we have few enough failures that large uncertainty in MFPT estimate is inescapable via the direct sample-mean estimate.

To overcome this issue, we developed a second, model-based, method built upon the derivations by Byl and Tedrake [27]. They estimated MFPT for a simulated robotic system, and thus the equations of motion (including noise terms) and the

## CHAPTER 2. HAPTIC FEEDBACK REDUCES RHYTHMIC VARIABILITY

feedback control laws were completely specified. However, in the present work, our goal is to estimate MFPT from experimental data—no model is known *a priori*. So, to apply the technique, we first must fit a stochastic dynamic model to behavioral data. We use the first-order AR model fitted to the data; see Equation (2.7) above. This model must be augmented to include a definition of failure (passage). For our experimental setup, failure is defined as the first apex event that exceeds the limits of the goal region; see Figure 2.4. In other words, the state  $x[k]$  is a failure if  $x > x_{\max}$  or  $x < x_{\min}$  (where  $x_{\max} = b_{\max} - b_{ss}$  and  $x_{\min} = b_{\min} - b_{ss}$ ).

In order to compute MFPT from this model requires the assumption that there exists a dominant metastable distribution<sup>2</sup> [27, 154], which we now assume. The state (apex height) evolution in Equation (2.7) represents a discrete-time, continuous-state Markov process. For computational purposes, we discretize the state space into a finite set of states as illustrated in Fig. 2.4(B). After that we compute the stochastic state transition matrix,  $\mathbf{T}$ :

$$\mathbf{T}_{ij} = \Pr(X[n] = x_j | X[n-1] = x_i) . \quad (2.10)$$

$\mathbf{T}_{ij}$  is the probability of going to  $j^{\text{th}}$  state from  $i^{\text{th}}$  state. Since  $x_1$  corresponds to the

---

<sup>2</sup>The metastable distribution is the stationary distribution conditioned on having not absorbed by the failure state.

failure region, we consider it as the absorbing state, such that

$$T_{11} = 1, T_{1j} = 0 \forall j \neq 1. \quad (2.11)$$

For all other elements we use the AR model in Equation (2.7) to complete the stochastic state distribution matrix. The  $n$ -step dynamics are revealed by the Chapman–Kolmogorov equation,

$$\mathbf{p}[n] = \mathbf{p}[n - 1]\mathbf{T}, \quad (2.12)$$

where  $\mathbf{p}[n]$  is the state distribution vector defined as

$$p_i[n] = \Pr(X[n] = x_i). \quad (2.13)$$

Assuming that the second-largest eigenvalue of  $\mathbf{T}$  is less than one, this absorbing Markov chain will have a unique stationary distribution, with the entire probability mass in the absorbing state. Since there is only one absorbing state and it is possible to jump to the absorbing state from any state (due to properties of Gaussian noise), our system inherently satisfies this assumption. The stochastic state transition matrix

$T$  in our problem takes the following specific form

$$T = \begin{bmatrix} 1 & \mathbf{0} \\ \mathbf{r} & \bar{T} \end{bmatrix} \quad (2.14)$$

with  $T \in \mathbb{R}^{N \times N}$ ,  $\bar{T} \in \mathbb{R}^{(N-1) \times (N-1)}$ ,  $\mathbf{0} \in \mathbb{R}^{1 \times (N-1)}$ ,  $\mathbf{r} \in \mathbb{R}^{(N-1) \times 1}$ . The dynamics of escape to the absorbing state can be investigated using eigenmode analysis [27]. Let us order the eigenvalues of  $T$ ,  $\lambda_i$ , in order of decreasing magnitude. The transition matrix from an absorbing Markov chain will have  $\lambda_1 = 1$ , with (left) eigenvector  $v_1 = [1 \ 0 \ \cdots \ 0]$  representing the stationary distribution on the absorbing state. The magnitude of the remaining eigenvalues ( $0 \leq |\lambda_i| < 1, \forall i > 1$ ) describe the transient dynamics and escape rate to the stationary distribution.

We assume that the second-largest eigenvalue,  $\lambda_2$ , (which is also the largest eigenvalue of  $\bar{T}$ , i.e.  $\lambda_2 = \bar{\lambda}_1$ ) is close to (but still less than) 1,  $\lambda_2 \lesssim 1$  and also  $\lambda_2 \gg |\lambda_3|$ , which means that initial conditions (in eigenmodes 3 and higher) decay quickly, and eigenvector of  $\bar{T}$  ( $\bar{v}_1$ ) associated with  $\bar{\lambda}_1 = \lambda_2$  describes the long-living (metastable) distribution of the state. The metastable distribution is given by  $\bar{v}_1$ —the eigenvector associated with largest eigenvalue of  $\bar{T}$  with proper normalization. Under these circumstances MFPT is approximated by

$$\hat{\mu}_{\text{mfpt}} \approx \frac{1}{1 - \lambda_2}. \quad (2.15)$$

## CHAPTER 2. HAPTIC FEEDBACK REDUCES RHYTHMIC VARIABILITY

Note that the sub-matrix  $\bar{T}$  is a positive matrix (not to be confused with positive-definite matrix), such that based on Perron-Frobenius theorem the largest eigenvalue of  $\bar{T}$  ( $\bar{\lambda}_1$ ) is always positive, and the magnitudes of all other eigenvalues are strictly lower than  $\bar{\lambda}_1$ , i.e.  $\bar{\lambda}_1 \in \mathbb{R}^+$  and  $\bar{\lambda}_1 > |\bar{\lambda}_i| \forall i > 1$ .

Making use of (2.15) is practically equivalent to assuming that metastable distribution is a good summary of the initial conditions. In fact, if the initial condition is a random variable that is drawn from the metastable distribution, (2.15) is the exact MFPT of the system. By assuming that  $|\lambda_3| \ll \lambda_2 \lesssim 1$ , the distribution will tend to quickly converge to the metastable distribution, making (2.15) a good approximation.

In order to test the reliability of the metastable distribution, we computed the MFPT starting from different initial conditions and generated confidence bounds on the MFPT estimate given by (2.15). The vector of MFPTs ( $\vec{\mu}_{\text{mfpt}}$ ) for all non-absorbing states can be computed as

$$\vec{\mu}_{\text{mfpt}} = \begin{bmatrix} \hat{\mu}_{\text{mfpt},2} \\ \vdots \\ \hat{\mu}_{\text{mfpt},N} \end{bmatrix} = (I - \bar{T})^{-1} \mathbf{1} \quad (2.16)$$

where  $\mathbf{1} = [1 \ \cdots \ 1]^T$  and  $\hat{\mu}_{\text{mfpt},i}$  denotes the MFPT starting from initial condition  $x_i$ . Specifically, we computed the 5<sup>th</sup> and 95<sup>th</sup> percentiles of  $\vec{\mu}_{\text{mfpt}}$  in order to form a confidence bound on (2.15).

## 2.3 Results

### 2.3.1 Subjects Believe Haptic Feedback Improves Their Performance

After completing the experimental session, all participants completed a brief questionnaire on their perception of task difficulty with and without haptic feedback. Among the fifteen participants whose data were not excluded, thirteen participants reported that the task seemed easier with haptic feedback. Two (out of fifteen) subjects reported no apparent difference in both cases. Among the three participants whose data were excluded, one subject reported that the task seemed easier without haptic feedback. This subject was also one of the subjects who failed to perform the task in both haptic conditions. The other subject who failed to perform the task in both haptic conditions was among the group that reported no apparent difference in both haptic conditions. Finally, the subject who did well with haptic feedback, but failed to achieve rhythmic juggling without haptic feedback, reported that the task was easier with haptic feedback.

### 2.3.2 Haptic Feedback Improves Performance

Each subject (excluding the three whose data was not included) performed better with haptic feedback in at least one performance metric (see Fig. 2.5). Based on the

## CHAPTER 2. HAPTIC FEEDBACK REDUCES RHYTHMIC VARIABILITY

PO metric, each subject performed better with haptic feedback and the difference in performance was statistically significant ( $p < 0.00001$ , paired t-test). For the CV metric, all but one subject also performed better with haptic feedback and this performance improvement was also statistically significant ( $p < 0.001$ , paired t-test).

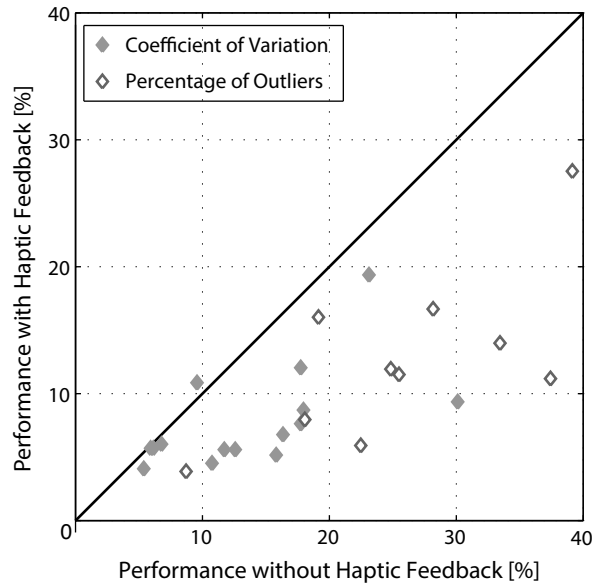


Figure 2.5: **Haptic feedback enhances performance.** Performance in two metrics PO (Percentage of outlier apex heights, hollow markers) and CV (coefficient of variation, solid markers), was significantly improved with haptic feedback; larger values of these metrics indicate inferior performance. Each marker compares the performances (based on one of the metrics) of a single individual for the two haptic conditions. Performance was enhanced by haptic feedback for points lying below the 45° line.

### 2.3.3 Nominal Stability is Fragile and Unchanged by Haptic Feedback

Impact accelerations illustrated in Fig. 2.3(A) show that majority (thirteen out of fifteen) of the participants did not adopt predominantly negative mean impact accelerations in either haptic condition, contradicting previous results [152]. According to [152], the impact acceleration is predominantly negative if it satisfies  $\ddot{p}_{\text{impact}} \in [-6, -2] \text{ m/s}^2$ . For the experiments with haptic feedback, they reported a median impact acceleration across all individuals of  $\ddot{p}_{\text{impact}} = -4.16 \text{ m/s}^2$ , whereas for the no haptic feedback experiments the median impact acceleration is  $\ddot{p}_{\text{impact}} = -0.31 \text{ m/s}^2$ . Even in a recent juggling study [162] from same group, reported mean impact acceleration with haptic feedback is not predominantly negative ( $\ddot{p}_{\text{impact}} = -1.75 \text{ m/s}^2$ , mean across 7 individuals and 4 different coefficient of restitution values), but this study did not compare impact accelerations with and without haptic feedback.

In our experiments, all subjects exhibited many positive impact accelerations, even for those whose average impact accelerations were negative. So, while the mean impact accelerations across individuals for both haptic conditions were slightly (but statistically significantly,  $p < 0.05$  one sided t-test) negative (see Table 2.2), nominal stability does not appear to be a robust strategy: for 21 out of 30 trials (15 Subjects  $\times$  2 Haptic Conditions), 25% or more of the impact accelerations were positive. Indeed, statistics of the data from Wei et al. [162] suggest similarly non-robust nominal

stability; even though the mean impact acceleration of each individual was negative in that study, for five out of seven participants at least 15% of the impact accelerations were positive.

Table 2.2: Mean impact accelerations ( $\ddot{p}_{\text{impact}}$  [m/s<sup>2</sup>]) in different studies

	Our Study	Sternad et al. [152]	Wei et al. [162]
Haptic Feedback	-0.863	-4.16	-1.75
No Haptic Feedback	-0.778	-0.31	–

We examined whether haptic feedback changes nominal stability by comparing the mean impact accelerations for each individual between the two haptic conditions, as shown in Fig. 2.3(B). We found no statistically significant difference ( $p > 0.4$ , paired t-test). Thus, haptic feedback cannot be shown to have had an effect on nominal stability, which contradicts previous conclusions [152].

Table 2.3 lists the magnitude of the largest eigenvalues for each subject and condition, computed based on limit cycle estimates (see Methods). Many subjects achieved a nominal eigenvalue of 0.8 (based on the average impact acceleration) in both haptic conditions, corresponding to the best (smallest) nominal eigenvalue possible, given the coefficient of restitution used in our experiments ( $\alpha = 0.8$ ) [137]. As for our nominal stability analysis based on paddle accelerations (see Fig. 2.3), we observed no significant improvement in the open-loop eigenvalues with the addition of haptic feedback ( $p > 0.65$ , paired sign test). Note that the eigenvalue distribution was non-normal because a significant fraction of the eigenvalues were concentrated at the coefficient of restitution of 0.8, and thus we used the more conservative signed test

rather than a t-test, which is not based on normality.

Table 2.3: Eigenvalues of the Nominal Behavior

	$ \lambda _{\max}$							
Subject #	1	2	3	4	5	6	7	8
HF	0.8	0.8	0.8	0.8	2.00	1.54	0.8	0.8
No HF	0.8	0.8	0.8	0.8	1.82	0.8	0.8	0.8
Subject #	9	10	11	12	13	14	15	
HF	0.94	1.43	0.8	0.8	0.8	0.8	0.94	
No HF	0.84	1.65	0.8	0.8	1.00	0.8	0.8	

Also, although we did not observe predominately negative accelerations in paddle trajectories (Fig. 2.3), the “typical” subject seems to achieve the best possible nominal eigenvalue in both haptic conditions. However, this observed nominal stability is fragile since many accelerations for each subject lies in the open-loop unstable region (nominal eigenvalue greater than 1).

### 2.3.4 Closed-Loop Eigenvalues are Stable, but Unchanged by Haptic Feedback

Nominal stability—which was not dependent upon the haptic condition—could not explain the performance enhancement afforded by haptic feedback during rhythmic juggling. Thus we examined the closed-loop dynamics. Specifically, we fitted a first-order AR model to the apex height time-series data (see Methods) and analyzed the closed-loop eigenvalues to quantify the stability of the behavior. The closed-loop eigenvalues of each subject are illustrated in Fig. 2.6.

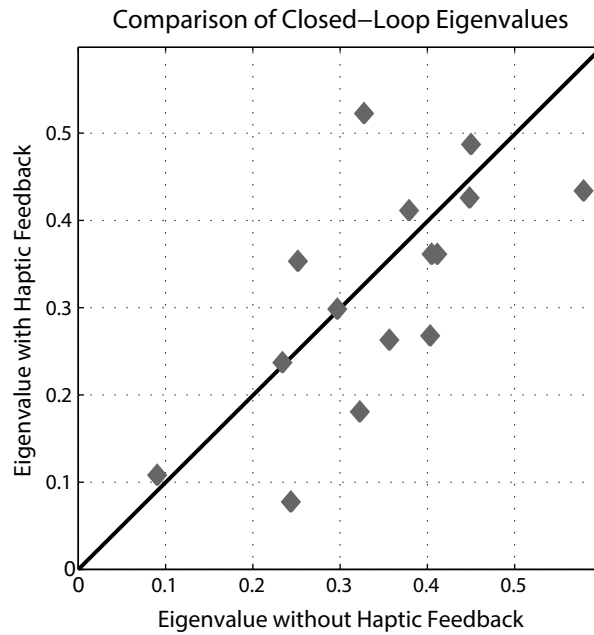


Figure 2.6: **Haptic feedback does not enhance closed-loop eigenvalues.** The closed-loop eigenvalues identified from experiments with and without haptic feedback are not significantly different. Each marker on the figure corresponds to an individual's closed-loop eigenvalues without (abscissa) and with (ordinate) haptic feedback. 45° line indicates ideal agreement in eigenvalues of conditions with and without haptic feedback.

Comparing the closed-loop eigenvalues with the nominal eigenvalues listed in Table 2.3 reveals that the least stable closed-loop eigenvalue in both haptic conditions,  $\lambda_{\max} = 0.58$ , is significantly more stable than the best eigenvalue,  $\lambda_{\text{best}} = 0.8$ , that could be achieved in open loop. Clearly, active sensory feedback control played a critical role in this juggling task. Similarly, Wei et al. [162, 163] and Ronsse et al. [130] observed that a purely passive model failed to explain measurements of closed-loop behavior in terms of “relaxation times” (convergence rate), thus indicating the existence of active error corrections.

Even though active feedback control clearly plays a role for the behavior, we observed no statistically significant trend in closed-loop eigenvalues between the two haptic conditions ( $p > 0.3$ , paired t-test). In fact, about half (seven of fifteen) of the subjects had more stable eigenvalues without haptic feedback. The results based on both the closed-loop and open-loop eigenvalues suggests that haptic feedback was not used by the nervous system to regulate the convergence rate in this juggling task, and the performance improvement must be explained by other means.

### 2.3.5 Haptic Feedback Improves Mean First Passage Time

MFPT provides a measure of stochastic stability for the closed-loop behavior. We verified the consistency of the two independent MFPT estimation methods (see

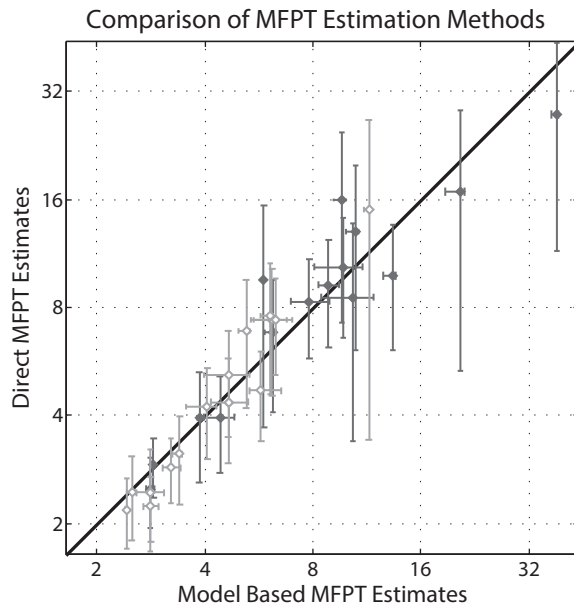


Figure 2.7: **Direct and model-based MFPT estimates agree.** Markers indicate the MFPT estimates (the horizontal axis is model-based, and the vertical axis is direct estimation—see Methods) for all users and both haptic conditions (with and without haptic timing cue). The 45° solid black line would indicate ideal agreement between direct and model-based MFPT estimation. Vertical and horizontal error bars indicate the 95% confidence bounds for the direct and model-based MFPT estimates, respectively.

## CHAPTER 2. HAPTIC FEEDBACK REDUCES RHYTHMIC VARIABILITY

Methods) by directly comparing them. Since each estimation method used the same data in categorically different ways, there were differences in the estimates; however, there was a strong correlation between estimates obtained via the two distinct methods (see Fig. 2.7). The 95% confidence bounds (direct estimates) overlapped with the model-based estimate in all cases. Thus, the two methods were independent, but mutually consistent, ways to assess the stochastic stability of the behavior.

We also observed the statistics of the  $\lambda_2$  and  $\lambda_3$  (second and third largest eigenvalues of  $T$  in (2.14), respectively) distributions obtained from our experimental data. The mean and standard deviations of the  $\lambda_2$  and  $\lambda_3$  data were  $(\mu_2, \sigma_2) = (0.8, 0.1)$  and  $(\mu_3, \sigma_3) = (0.15, 0.09)$  respectively; given that these eigenvalues are bounded between 0 and 1,  $\lambda_3$  was much lower than  $\lambda_2$ , as expected. In order to test further the reliability of (2.15) (i.e. model-based MFPT estimates), we scrutinized our assumptions by computing 95% confidence bounds on (2.15). The confidence bounds (Fig. 2.7) indicated that the uncertainty of the model based method was much lower than the uncertainty of the direct estimation method.

As shown in Fig. 2.8, each subject's MFPT was higher (i.e. more stable) with haptic feedback and the differences were significant ( $p < 10^{-4}$ , direct method and  $p < 0.005$ , model-based method; paired t-test).

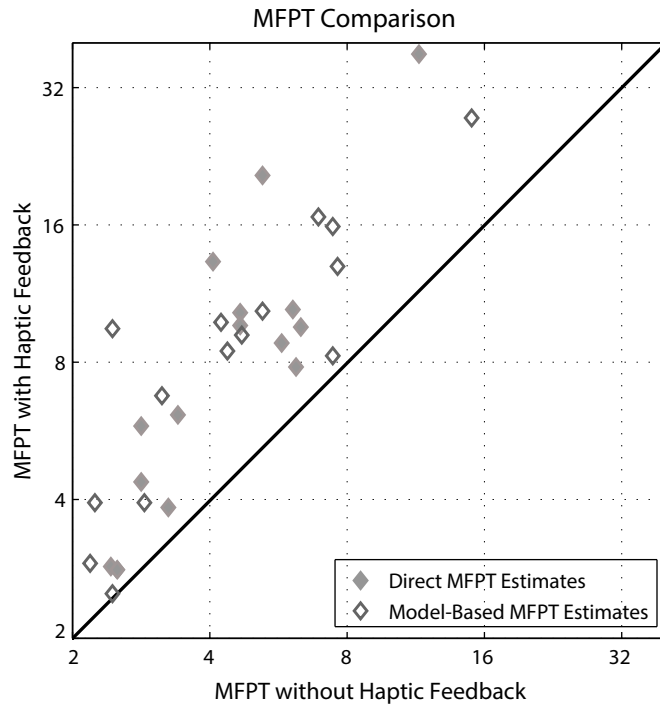


Figure 2.8: **Haptic feedback enhances metastability (MFPT)**. Markers indicate the MFPT values without (horizontal axis) and with (vertical axis) haptic feedback. Direct and model-based MFPT estimates are depicted by solid light gray and hollow dark gray markers respectively.

## 2.4 Discussion

What is the mechanism by which the haptic cue at the instant of ball–paddle collision improves juggling performance? We suspected that the haptic cue would quicken convergence. Surprisingly, however, haptic feedback had no significant effect on the convergence rate as measured by either the nominal or closed-loop eigenvalues of the dynamics in our study. Instead, we found that long-term metastability—namely, the *persistence* of the system—was enhanced. The haptic timing cue is a measurement that decreases the nervous system’s uncertainty of the ball’s state. Decreasing noise may improve stability as measured by persistence, while potentially having very little effect on convergence rate. Indeed, it may not be the speed of convergence, but rather the infrequency of failures that matters most for a great many behaviors.

### 2.4.1 Stability: Convergence or Persistence?

It has long been hypothesized that human motor control policies are derived from an economic policy made by the nervous system, such as optimizing energetic cost, reward rate, and stability [81, 94, 99, 121, 143]. However, little is known about how stability might affect the neural controller or how stability might be evaluated in such a cost function.

The most common measure of system stability is the tendency of a system to

## CHAPTER 2. HAPTIC FEEDBACK REDUCES RHYTHMIC VARIABILITY

return to steady-state after a perturbation. This tendency can be measured in terms of a system's eigenvalues. Thus, it is natural to hypothesize that one of the goals of the nervous system is to effectively regulate the eigenvalues of the closed-loop behavior. If this measure of stability were important, then one might predict faster convergence rates in the presence of haptic feedback. In paddle juggling, we investigated the two main possible ways of regulating the convergence rate. One way is shaping the nominal paddle trajectories without adjusting the feedback controller, and the other way is regulating the feedback controller itself. The human nervous system might choose either (or both) ways to tune the stability of the behavior. Different hypotheses on the role of haptic feedback for human paddle juggling behavior are illustrated in Fig. 2.9.

In contrast to previous results [152], we observed no statistically significant change in nominal patterns, suggesting that haptic feedback did not enhance nominal stability (Fig. 2.3). Perhaps this is not so surprising: it seems counterintuitive that adding haptic sensory information would decrease optimality. Recall that increasing nominal stability of the nominal pattern requires higher (absolute) negative accelerations at impact; thus immediately before impact the paddle (and arm) must reach a peak velocity that is actually substantially *higher* than the impact velocity. Producing faster arm motions than nominally necessary likely wastes energy. However, since it is possible to regulate convergence rate in rhythmic ball motion using active closed-loop neural feedback without changing the nominal trajectories, there may be no need to

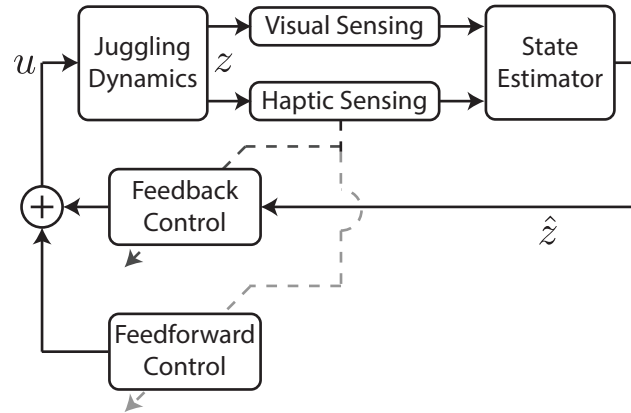


Figure 2.9: **Simplified schematic representation of juggling behavior with different hypotheses on the role of haptic feedback.** Dashed lines represent (slow) parametric or “structural” tuning of the dynamics. Solid lines represent (fast) dynamical signals.  $z$  and  $\hat{z}$  represent the actual and estimated (continuous and discrete) states of the dynamics, respectively.  $u$  is the control input to the juggling dynamics which is regulated by the feedforward and feedback controllers. In principle, haptic sensing information could be used for tuning or regulation of feedforward (nominal) motor patterns (dashed light gray line), regulation of feedback controllers (dashed dark gray line) and/or state estimation (solid line). We found that neither the feedforward pattern nor the feedback gains were altered by the presence of haptic feedback. This suggests that haptic feedback serves mostly a state-estimation-like role that reduces uncertainty, thus improving performance in paddle juggling.

## CHAPTER 2. HAPTIC FEEDBACK REDUCES RHYTHMIC VARIABILITY

sacrifice energetic optimality for nominal stability. So, we investigated the stability of the closed-loop system (Fig. 2.9) by analyzing its eigenvalues.

The closed-loop eigenvalues illustrated in Fig. 2.6 verify our hypothesis that the closed-loop dynamics are dramatically more stable than the nominal eigenvalues. Indeed, the slowest closed-loop eigenvalue extracted from all trials was significantly more stable than the best possible nominal eigenvalue of 0.8. However, the addition of haptic feedback did not change the closed-loop stability (Fig. 2.6). Taken together, these results strongly suggest that haptic feedback provided at the moment of ball–paddle collision had no significant effect in convergence rate (in either nominal or closed-loop). Thus, the regulation of convergence rate cannot explain the difference in performance in between two haptic conditions.

Rate of convergence to an equilibrium point, while commonly used and easy to quantify, is hardly the only measure of stability that is relevant to rhythmic behaviors [32,124]. Moreover, different stability measures may yield qualitatively different results. For example, [32] showed that open-loop linear stability does not correlate well with the size of the domain of attraction for an open-loop juggling model. More recently, [27] applied the MFPT as a stability metric to quantify long-term metastability. The MFPT can be thought of as the tendency of a system to *persist* for long periods of time, rather than the tendency of a system to *converge*.

Eigenvalues again play a role, but here the eigenvalue of interest,  $\lambda_2$  (see (2.15)), is the one associated with the (statistical) “escape rate” of the system—the associ-

## CHAPTER 2. HAPTIC FEEDBACK REDUCES RHYTHMIC VARIABILITY

ated MFPT is given by  $\hat{\mu}_{\text{mfpt}} = 1/(1 - \lambda_2)$ . We suspect that the eigenvalues of the dynamics fail to explain the performance improvement with added haptic feedback due to their deterministic nature; they cannot capture stochastic characteristics of the real system. So, we adopted the MFPT as stability metric because it embraces the inherent stochasticity of the system. All biological systems suffer from some uncertainty or stochasticity, thus MFPT—i.e. *persistence*—may be a useful alternative to traditional eigenvalues—i.e. convergence—as a measure of stability. Indeed, our analysis with MFPT shows that haptic feedback enhanced the long-term closed-loop metastability as measured via the MFPT (Figure 2.8).

We suspect that the primary effect of haptic feedback in this task was to mitigate noise or uncertainty (a natural consequence of adding additional sensory information), thereby enhancing persistence of the dynamics and ultimately improving subject performance in the task.

To illustrate the profound effect of decreasing uncertainty on metastability and persistence, as compared to aggressively regulating the convergence rate, in Fig. 2.10 we illustrate the dependence of MFPT on two parameters—the eigenvalue and the uncertainty—of a scalar stochastic dynamical system with additive white Gaussian noise. Uncertainty in Fig. 2.10 is measured in the form of a normalized standard deviation (standard deviation divided by the vertical size of the goal region). As shown, a decrease in normalized standard deviation is dramatically more effective than a decrease in the eigenvalue in terms of improving MFPT-based stability. In other

words, minimizing the deterministic eigenvalues (which may be highly suboptimal) is ineffective compared to mitigating noise, and thus the first goal of additional sensory measurements may be to reduce uncertainty, not regulate convergence rate.

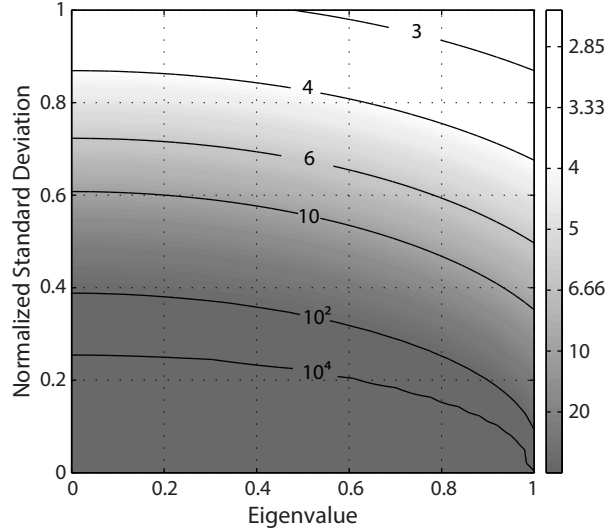


Figure 2.10: **Reducing noise is more effective for increasing MFPT than regulating eigenvalues.** The MFPT is shown as a function of the eigenvalue and uncertainty of a scalar stochastic dynamical system with additive white Gaussian noise (see Eq. (2.7)). Upper and lower failure limits are symmetric with respect to the origin. Uncertainty is measured in the form of a normalized standard deviation, which is computed by dividing the standard deviation by the size of the goal region ( $b_{\max} - b_{\min}$ ). Darker means more stable (i.e. higher MFPT) in the contour plots.

## 2.4.2 Sensing of Hybrid Transitions for State Estimation

Rhythmic motor control tasks, such as legged locomotion, often involve *hybrid transitions*, namely discrete changes in the contact configuration of an animal with

its surrounding environment. When a rhythmic system operates near a limit cycle (see Methods), these hybrid transitions punctuate the system dynamics at particular instants in *phase* [128], a measure of the time elapsed since the beginning of a cycle, relative to the overall cycle time. Sensing the timing and state of hybrid transitions may enhance rhythmic motor control performance.

Haptic sensing plays a critical role in motor control, as has been shown for rhythmic finger movements [55, 153, 168] and continuous haptic feedback during dynamic manipulation tasks [60, 88]. However, surprisingly few neuroscience studies address how haptic feedback—especially provided by hybrid transitions—enhances neural control during dynamic rhythmic behaviors such as juggling [152].

To furnish a mechanistic explanation for how haptic sensing may enhance performance in this rhythmic dynamical task, it is natural to interpret our results in terms of state estimation and feedback control [97, 138]. In this context, one possibility is that the nervous system may process haptic cues at hybrid transitions to improve state estimation, thereby reducing uncertainty, as has been demonstrated in legged robotic systems [78, 107]. The estimated states could be used by a separate controller whose goal may be regulating energy, cost of transport, stability etc. This interpretation resembles the “separation principle” in the linear-quadratic-Gaussian (LQG) control problem [15]. LQG is an optimization problem where the goal is to minimize a cost function for linear systems that suffer from uncertainty in the form of additive Gaussian noise, and the solution involves a combination of a Kalman filter and linear-

## CHAPTER 2. HAPTIC FEEDBACK REDUCES RHYTHMIC VARIABILITY

quadratic regulator (LQR). The Kalman filter optimally estimates the states and the LQR optimally applies state feedback—based only on state estimates—to control the plant. A loose analogy can be drawn between the LQG problem and our paddle-juggling control problem: adding haptic feedback in the juggling problem amounts to adding an additional sensor measurement. Assuming linear dynamics around the nominal trajectory, and applying the separation principle, then only the estimator, i.e. the Kalman filter, would be affected by the number of measurements, and the state feedback gains would remain the same. Our data suggest that this mechanism could be at play for the human motor control of paddle juggling. Indeed, it has been shown that the human nervous system integrates haptic cues with other sensory modalities in a statistically optimal fashion for estimating the size of an object [56] and for synchronizing finger motions [55, 168]. Thus, it is possible that humans may integrate haptic and visual feedback under a Kalman-filter-like strategy to estimate the states of the ball (and hand) in paddle juggling behavior while keeping the controllers fixed. Our findings suggest that haptic cues during hybrid transitions improve state estimation and a separate controller uses these state estimates for control, in a manner not dissimilar from a separate Kalman filter plus a LQR controller for a linear control system.

However, the separation principle does not necessarily apply to nonlinear systems such as juggling. For example, since the removal of sensory information can decrease the reliability of sensor-based state estimates, the nervous system may rely on shaping

nominal paddle motions to improve nominal stability and less on sensory feedback. [152] reported the reverse of this in paddle juggling, where the *addition* of haptic feedback caused steady-state hand trajectories to become more nominally stable, but also energetically more costly. We were unable to reproduce this result.

### 2.4.3 “Perfect-Time” Control

Almost all control system formulations implicitly depend on the assumption that time can be perfectly observed. What happens if this assumption is violated, i.e. if the chronometer is imperfect? Perhaps due to the remarkable precision of engineered clocks, this question has been largely ignored. Neural control systems in nature, by contrast, exhibit significant temporal variability [18]. Thus, while neglecting uncertainty in time leads to accurate control systems for many engineering applications, perfect timekeeping may be a poor assumption for the modeling and analysis of biological control systems. And yet, all computational models of human motor control implicitly assume that time is known to the neural controller [81, 98, 143, 144, 155], including our own prior work [31].

Both open- and closed-loop controllers may be time varying, thus both categories of control policies may suffer from the imperfections in chronometry. For example, Lamperski and Cowan [101, 102] extended the finite-horizon LQR problem to account for temporal uncertainty, and showed that in this context the classical solution produces suboptimal results. Open-loop control policies, such as for juggling [137], even

more sharply illustrate the potential problems in assuming perfect timekeeping. An open-loop control policy is typically formulated as a function that maps the time  $t$  into control input  $u(t)$ . However, time must be measured and/or estimated; is it appropriate to call this *open-loop* control, or rather *perfect-time feedback* control [104]? Indeed, it is even possible for a system that has been stabilized using open-loop (perfect-time feedback control) to be destabilized by small imperfections in timing [104].

Open-loop control is appealing because it potentially obviates the need for complex computations and active feedback [62, 66, 67, 113, 137]. Since the animal nervous system does not have access to a precise master clock, the nervous system must estimate and process time [17, 24, 51], likely integrating feedback from sensory stimuli. Carver et al. [30] showed that even for a simplified model of motor control, time estimation requires complex computations. Thus, “open-loop” control does not, after all, eliminate the need for feedback or complex computations, since time itself must be estimated. Perhaps sensory feedback provided during hybrid transitions not only enhances state estimates, but also enhances time estimates, therefore decreasing uncertainty in both feedback and feedforward control, ultimately enhancing long-term metastability. Recently, Studenka et al. [153] showed that adding event based tactile feedback in a rhythmic circle drawing task can enhance the structure of timing variability supporting our theory regarding the connection between haptic feedback and human timing.

## Chapter 3

# Walking dynamics are symmetric (enough)

Many biological phenomena such as locomotion, circadian cycles and breathing are quasi-periodic in nature and can be modeled as rhythmic dynamical systems. Dynamical systems modeling often involves neglecting certain characteristics of a physical system as a modeling convenience. For example, human locomotion is frequently treated as symmetric about the sagittal plane. In this work, we test this assumption by examining human walking dynamics around the steady-state (limit-cycle). Here we extend statistical cross validation and bootstrapping techniques in order to examine whether there are statically significant asymmetries, and even if so, test the consequences of assuming bilateral symmetry anyway. Indeed, we verify that there are significant asymmetries in the dynamics of human walking, but nevertheless show

that ignoring these asymmetries results in a more consistent and predictive model. In general, neglecting evident characteristics of a system can be more than a modeling convenience—it can produce a better model.

## 3.1 Introduction

The concept of symmetry has helped shape our understanding of engineering and biology alike. The Roman text “De architectura” by Vitruvius and the eponymous “Vitruvian Man” by Leonardo Da Vinci exemplify the influence of symmetry in animals and humans on man-made works of art and engineering. Symmetry serves to simplify and reduce complexity, making it a powerful tool in computational and analytical applications. The ubiquity of bilateral (left–right, sagittal plane) symmetry in animals is genetically encoded [58], and from an engineering point of view, building machines with bilateral symmetry is justified by the fact that the left–right axis is unbiased either by gravity or by direction of movement. However, genetic encoding of symmetry manifests itself imperfectly: numerous factors, such as differences in contralateral limb lengths, dominance of “leggedness” and handedness, and developmental processes break perfect symmetry, and enhance asymmetry.

Various measures and indices of asymmetry have been used to argue that human locomotion is bilaterally symmetric or asymmetric (for reviews, see [87,133]). Symmetry is thought to confer some advantages on motor abilities (e.g. improved energetic

### CHAPTER 3. WALKING DYNAMICS ARE SYMMETRIC (ENOUGH)

efficiency [57, 100, 112]). The common trend among previous work is the comparison of kinetic and/or kinematic gait parameters between the right and left halves of the body, i.e. joint angles [59, 80, 92, 126], ranges [77, 151] and velocities [105], stride lengths [35, 36, 77, 126], ground reaction forces [79, 84, 114, 159], EMG profiles [14, 28, 111, 122], limbs forces and moments [16, 45, 103, 160], or center-of-mass oscillations [42, 43, 70]. However, as Sadeghi et. al. [133] state, “. . . can we argue that it is acceptable to conclude that able-bodied gait is asymmetrical just because of the existence of statistically significant differences between two corresponding parameters (which we call local asymmetry) calculated from the right and left limbs?” During human walking, do steps from left-to-right and right-to-left recover significantly differently from perturbations? Indeed, there are differences in leg dominance—e.g. preferred kicking leg—that might lead to different responses from step-to-step.

Aside from demonstrating asymmetry (or not) in gait parameters, we found no studies examining the potential benefits of *neglecting* evident asymmetries. If there is a step-to-step dynamical asymmetry, does fitting a model from stride to stride (two step) rather than step to step (one step) better capture the dynamics of human walking? Of course, no single physical system has perfect “symmetry”. Thus symmetric models are inherently wrong for any physical system, but may nevertheless be useful for simplifying both the modeling and analysis.

“Essentially all models are wrong, but some are useful” wrote George E. P. Box in his seminal book [20]. According to Box, the important practical concern regarding

### CHAPTER 3. WALKING DYNAMICS ARE SYMMETRIC (ENOUGH)

the models of physical phenomena is “how wrong do they have to be to not be useful?” With regard to bilateral asymmetry in human walking, we attempt to frame this concern as follows. How wrong is it to neglect asymmetry from a statistical point of view? And how useful is symmetric modeling in terms of predictive power and simplicity? In most cases correctness and usefulness are directly related, and they are tested simultaneously. However, in the context of data-driven modeling of human walking dynamics, the “wrongness” and “usefulness” of assuming symmetry are related but have critical, nuanced differences. The methods presented in this thesis allows us to independently (statistically) address these differences.

In this chapter, we test the assumption of bilateral symmetry in the dynamics of human walking. As an example, consider fitting linear models to two distinct data sets (e.g. “left steps” and “right steps”) and testing these models in terms of their respective ability to predict isolated validation data from just the one of the data sets, say “left steps”. If walking were perfectly symmetric, both the left-step (“correct”) model and right-step (“wrong”) model would perform indistinguishably in left-step validation. However, we show that there are statistically significant asymmetries in the dynamics of human walking in healthy subjects in the sense that the “wrong” model performs statistically worse than the “correct” model in validation. Despite these asymmetries, we also show that a more consistent and predictive model of the dynamics is obtained by assuming symmetry, and pooling all the data from both left and right steps to form a generic model. Quite surprisingly, this fit significantly out-

performs the mapping fitted to only left steps even when predicting left-step data. This is good news because in addition to our finding that it is statistically better to neglect asymmetry, it is also practically and theoretically convenient to assume symmetry. These advantages lead us to conclude that the assumption of symmetry in walking dynamics, though clearly wrong in a platonic sense, is nevertheless more useful for all practical purposes.

### 3.1.1 Limit-Cycle Dynamics and Symmetry

As explained in Section 1.1, our approach to analyzing and modeling walking involves treating the underlying behavior as a rhythmic dynamical system operating around a stable limit cycle and we further use Poincaré theory in our analysis of rhythmic walking dynamics. The specific Poincaré section that we adopt for human walking is the heel strike event, as explained in Section 3.2.2. Here, we define symmetry in the context of limit-cycle modeling of walking and consider what kind of symmetries (and asymmetries) can be addressed using this approach.

In our modeling approach, there are two core elements: the limit-cycle of the rhythmic system which characterizes the steady-state behavior, and the dynamics (both deterministic and stochastic) around the limit-cycle. In this study, we are interested in the latter.

Beyond its utility for approximation, bilateral symmetry of the (steady-state) limit-cycle trajectory may have physiological significance, such as reducing metabolic

## CHAPTER 3. WALKING DYNAMICS ARE SYMMETRIC (ENOUGH)

cost [57, 100, 112]. Indeed, the kinematic and kinetic variables that are the focus of the majority of studies that address human [133] or animal [119, 123] locomotor symmetry are steady-state (periodic) variables that correspond to the limit cycle of a dynamic model.

Here, we consider the dynamics near, but *off of* the limit cycle, using data from Poincaré sections to estimate return maps. Hence our analysis is not based on the steady-state parameters of gait, but how the gait deviates from and recovers to these steady-state parameters. To the best of our knowledge, this is the first study that analyzes the *dynamical* symmetry of biological rhythmic systems. We validate our methods in data from normal human walking experiments. These methods are also applicable to robotic or biological locomotor behavior with approximately symmetric gait patterns.

### 3.1.2 Dissemination

Figures and the text presented in Chapter 3 have been reported in a preprint on arXiv [9].

## 3.2 Methods

The system of interest is human treadmill walking. This data set is obtained for eight healthy young adult participants, at three different belt speeds (0.5, 1.0, and 1.5

m/s). We required the subjects to cross their arms in order to continuously record the marker positions. The Johns Hopkins Institutional Review Board approved all protocols and all subjects gave informed written consent prior to participation.

### 3.2.1 Kinematic Data

We placed infrared (IR) markers on subjects' left and right shoulder, hip, knee, ankle, and toe. Markers were tracked in 3D using Optotrak (Northern Digital) at 100 Hz. The marker data was used to calculate the four sagittal plane angles on each side as illustrated in Figure 3.1. The raw angular data was smoothed with a fifth-order, zero-phase-lag (non-causal) Butterworth filter to remove measurement noise and ease angular velocity estimation. In order to estimate angular velocities, a central difference filter and another zero-phase-lag Butterworth filter was applied to the smoothed angular data. We assume that the smoothed angles (8) and angular velocities (8) form a 16 dimensional state space for walking. The state vector includes angles (rad),

$$\begin{aligned}
 \boldsymbol{\theta}_L(t) &= \begin{bmatrix} \theta_{fL} & \theta_{aL} & \theta_{kL} & \theta_{hL} \end{bmatrix}^T, \\
 \boldsymbol{\theta}_R(t) &= \begin{bmatrix} \theta_{fR} & \theta_{aR} & \theta_{kR} & \theta_{hR} \end{bmatrix}^T, \\
 \boldsymbol{\theta}(t) &= \begin{bmatrix} \boldsymbol{\theta}_L(t) \\ \boldsymbol{\theta}_R(t) \end{bmatrix}
 \end{aligned} \tag{3.1}$$

### CHAPTER 3. WALKING DYNAMICS ARE SYMMETRIC (ENOUGH)

and angular velocities (rad/s),

$$\begin{aligned}
 \dot{\boldsymbol{\theta}}_{\mathbf{L}}(t) &= \begin{bmatrix} \dot{\theta}_{fL} & \dot{\theta}_{aL} & \dot{\theta}_{kL} & \dot{\theta}_{hL} \end{bmatrix}^T, \\
 \dot{\boldsymbol{\theta}}_{\mathbf{R}}(t) &= \begin{bmatrix} \dot{\theta}_{fR} & \dot{\theta}_{aR} & \dot{\theta}_{kR} & \dot{\theta}_{hR} \end{bmatrix}^T, \\
 \dot{\boldsymbol{\theta}}(t) &= \begin{bmatrix} \dot{\boldsymbol{\theta}}_{\mathbf{L}}(t) \\ \dot{\boldsymbol{\theta}}_{\mathbf{R}}(t) \end{bmatrix}.
 \end{aligned} \tag{3.2}$$

Subscripts  $f$ ,  $a$ ,  $k$ , and  $h$  stand for foot, ankle, knee, and hip, respectively.  $L$  and  $R$  mnemonically denote the left and right legs.

In order to analyze the data independently from the physical units, the state space was non-dimensionalized based on the time constant associated with pendular walking [4, 19, 49, 134]:

$$\begin{aligned}
 \bar{\boldsymbol{\theta}} &= \boldsymbol{\theta} \\
 \bar{\dot{\boldsymbol{\theta}}} &= \dot{\boldsymbol{\theta}} \sqrt{\frac{l_0}{g}},
 \end{aligned} \tag{3.3}$$

where the bar represents the corresponding non-dimensionalized variable,  $g$  is the gravitational acceleration, and  $l_0$  is the leg length of the subject, which is estimated from the marker positions on right hip and ankle.

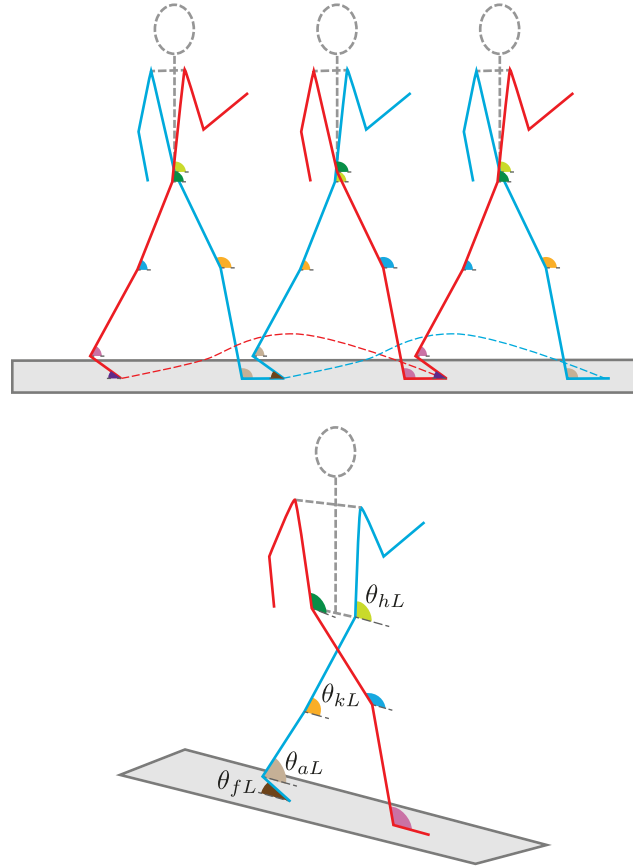


Figure 3.1: **Visualization of leg angle vector  $\theta$ .** The left leg (blue) and right leg (red) alternate between stance and swing phase over the course of a stride. The variables  $\theta_{fL}$ ,  $\theta_{aL}$ ,  $\theta_{kL}$ , and  $\theta_{hL}$  correspond to the left foot, ankle, knee, and hip angles respectively. The corresponding right leg angles,  $\theta_{fR}$ ,  $\theta_{aR}$ ,  $\theta_{kR}$ , and  $\theta_{hR}$ , are not labeled. The 8 leg angles and their respective angular velocities form the 16-dimensional state vector.

### 3.2.2 Events and Section Data

The treadmill used in this study features a split belt<sup>1</sup> that mechanically decouples the vertical ground reaction forces caused by each foot. Each belt is instrumented with a separate load cell, facilitating the estimation of the timing of heel-strike events. We chose heel-strike events as Poincaré sections for the analyses.

Let  $t[k]$  be the times of heel strike events, where  $k \in \mathcal{K} = \{1, 2, 3, \dots, k_{\max}\}$ , with  $k_{\max}$  being the total number of heel-strike events of both legs in one walking trial. For example, if the first heel-strike event ( $k = 1$ ) corresponds to the left leg, sets of odd ( $\mathcal{K}_L$ ) and even ( $\mathcal{K}_R$ ) integer indices from 1 to  $k_{\max}$  correspond to the left and right heel-strike events, respectively, such that  $\mathcal{K} = \mathcal{K}_L \cup \mathcal{K}_R$ . Over one stride of walking, there are two Poincaré sections of interest at heel-strike events. The measurement of the state vector at these Poincaré sections is given as follows:

$$\mathbf{z}[k] = \begin{bmatrix} \bar{\boldsymbol{\theta}}(t[k]) \\ \dot{\bar{\boldsymbol{\theta}}}(t[k]) \end{bmatrix}. \quad (3.4)$$

During steady-state walking and in the absence of noise, the periodic orbit would remain on the limit cycle:

$$\begin{aligned} \mathbf{z}[m] &= \boldsymbol{\mu}_L, \quad \forall m \in \mathcal{K}_L \\ \mathbf{z}[m'] &= \boldsymbol{\mu}_R, \quad \forall m' \in \mathcal{K}_R \end{aligned} \quad (3.5)$$

---

<sup>1</sup>While the belts of the treadmill can be driven at different speeds, this study addresses bilateral symmetry so both belts were driven at the same speed.

### CHAPTER 3. WALKING DYNAMICS ARE SYMMETRIC (ENOUGH)

where  $\boldsymbol{\mu}_L$  and  $\boldsymbol{\mu}_R$  are the fixed-points with respect to each of the two distinct Poincaré sections. Note that assuming bilateral symmetry implies that these two fixed points are identical up to a relabeling [33, 50, 106, 167]. This relabeling can be expressed as a linear mapping of right-heel-strike coordinates:

$$M : \begin{bmatrix} \bar{\boldsymbol{\theta}}_L(t[k]) \\ \bar{\boldsymbol{\theta}}_R(t[k]) \\ \dot{\bar{\boldsymbol{\theta}}}_L(t[k]) \\ \dot{\bar{\boldsymbol{\theta}}}_R(t[k]) \end{bmatrix} \mapsto \begin{bmatrix} \bar{\boldsymbol{\theta}}_R(t[k]) \\ \bar{\boldsymbol{\theta}}_L(t[k]) \\ \dot{\bar{\boldsymbol{\theta}}}_R(t[k]) \\ \dot{\bar{\boldsymbol{\theta}}}_L(t[k]) \end{bmatrix}, \quad \forall k \in \mathcal{K}_R, \quad (3.6)$$

where

$$M = \begin{bmatrix} 0 & I_{4 \times 4} & 0 & 0 \\ I_{4 \times 4} & 0 & 0 & 0 \\ 0 & 0 & 0 & I_{4 \times 4} \\ 0 & 0 & I_{4 \times 4} & 0 \end{bmatrix}. \quad (3.7)$$

As explained in Section 1.1 our approach to modeling human walking centers around fitting linear maps between Poincaré sections around the associated fixed points. First, we estimated the fixed points via

$$\begin{aligned} \hat{\boldsymbol{\mu}}_L &= \frac{1}{|\mathcal{K}_L|} \sum_{k \in \mathcal{K}_L} \mathbf{z}[k], \\ \hat{\boldsymbol{\mu}}_R &= \frac{1}{|\mathcal{K}_R|} \sum_{k \in \mathcal{K}_R} \mathbf{z}[k], \end{aligned} \quad (3.8)$$

CHAPTER 3. WALKING DYNAMICS ARE SYMMETRIC (ENOUGH)

where  $|\mathcal{K}_L|$  and  $|\mathcal{K}_R|$  denote the cardinality of sets  $\mathcal{K}_L$  and  $\mathcal{K}_R$  respectively. Note that *kinematic* asymmetry could be measured directly in terms of the difference between respective fixed points  $\hat{\boldsymbol{\mu}}_L$  and  $\hat{\boldsymbol{\mu}}_R$ . While potentially of interest, the current study focuses on *dynamical* asymmetry (measured in terms of the section maps), and thus we computed the residuals by subtracting the estimated fixed points from the section data:

$$\begin{aligned} \mathbf{q}_L[k] &= \mathbf{z}[k] - \hat{\boldsymbol{\mu}}_L, & k \in \mathcal{K}_L, \\ \mathbf{q}_R[k] &= \mathbf{z}[k] - \hat{\boldsymbol{\mu}}_R, & k \in \mathcal{K}_R. \end{aligned} \tag{3.9}$$

Section maps were estimated using these residuals. A section map from  $\mathbf{q}_L$  to the subsequent  $\mathbf{q}_R$  is denoted as  $L \mapsto R$ . We fit two categories of section maps: step-to-step ( $L \mapsto R$  and  $R \mapsto L$ ) and stride-to-stride ( $L \mapsto L$  and  $R \mapsto R$ ). See Fig. 3.2.

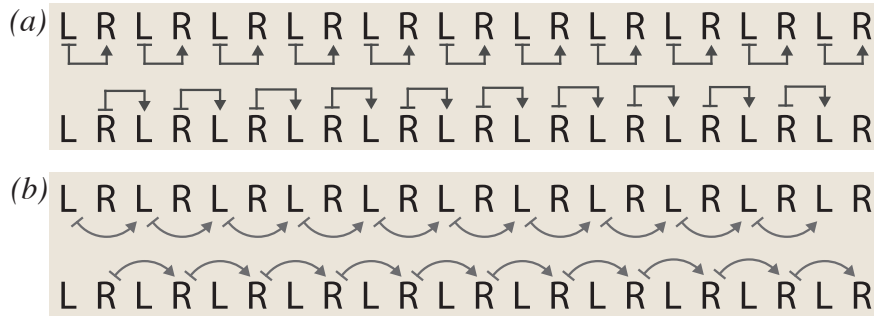


Figure 3.2: **Types of input–output pairs analyzed in this thesis.**  $L$  and  $R$  represent the Poincaré sections associated with heel-strike events of the left and right legs. (a) Left-to-right step maps (top) and right-to-left step maps (bottom). Step maps are denoted using straight arrows. (b) Left-to-left stride maps (top) and right-to-right stride maps (bottom). Stride maps and step maps are distinguished throughout the thesis by shape (straight versus curved arrows, respectively).

### 3.2.3 Fitting Section Maps

To fit the section maps for each category explained above, we stack all the appropriate residuals ( $\mathbf{q}_L$  and/or  $\mathbf{q}_R$ ) in matrices  $X$  (input) and  $Y$  (output):

$$X = [x_1, \dots, x_N]^T, Y = [y_1, \dots, y_N]^T, x_i, y_i \in \mathbb{R}^d, \quad (3.10)$$

where  $x_i$  and  $y_i$  represent residuals ( $\mathbf{q}$ ) from sections evaluated in the data. For example, to fit the  $L \mapsto R$  step-to-step map, one would set the columns of  $X$  and  $Y$  as follows:

$$\begin{aligned} x_1 &= q_L[1], & y_1 &= q_R[2], \\ x_2 &= q_L[3], & y_2 &= q_R[4], \\ &\vdots & &\vdots \\ x_N &= q_L[2N - 1], & y_N &= q_R[2N]. \end{aligned} \quad (3.11)$$

The linear section maps are modeled as follows:

$$y_i = Ax_i + \delta_i, \quad \forall i, \quad (3.12)$$

$$Y = XA^T + \Delta, \quad (3.13)$$

where  $\delta_i$  is additive noise. The section map can be estimated via least squares:

$$\hat{A} = (X^\dagger Y)^T. \quad (3.14)$$

where  $X^\dagger$  is the Moore-Penrose pseudoinverse of  $X$ .

## 3.3 Statistical Approach

We extended classical cross validation and bootstrapping techniques in order to examine the symmetry in the walking dynamics. This section describes the cross-validation approach. Details of the bootstrap approach can be found in the Appendix B.

### 3.3.1 Extending Monte Carlo Cross-Validation

Classical cross validation (CV) involves fitting a model to a *training set* of input–output data, and validating the model by comparing its predictions on a complementary *test set* of input–output data. In classical CV, there exists  $n$  pairs of input–output data which are then split into a training (fitting) set ( $n_f$  pairs) and complementary test (validation) set ( $n_v = n - n_f$  pairs). The training set is used for model fitting. The fitted model is then applied to the inputs of the test set to generate output predictions; the error metric between the predicted and actual outputs is the *cross-validation error* (CVE). The CVE is used to evaluate the performance of the model. CV methods are commonly used for selecting models based on their predictive ability [109, 125, 145, 170]. A fairly recent review paper by Arlot and Celisse [13] nicely summarizes different cross-validation methods and discusses their powers and also

### CHAPTER 3. WALKING DYNAMICS ARE SYMMETRIC (ENOUGH)

limitations.

A critical question when using a CV method is how to split the data [145]. Assuming no replacement, there exists  $\binom{n}{n_v}$  different ways of splitting the data set. The most popular CV method, often called leave-one-out cross validation (LOOCV), uses  $n_v = 1$ , because it incurs the least computational cost. However, LOOCV is inconsistent (asymptotically biased) [145], and its performance is poor in practice if the sample size is large. However for  $n_v \gg 1$  and  $(n - n_v) \gg 1$ , computing cross validation for all  $\binom{n}{n_v}$  possibilities can be computationally expensive. One way of decreasing the computational complexity is to apply  $k$ -fold cross validation [13, 96].

In  $k$ -fold CV, the data is initially split into  $k$  mutually exclusive, equal-sized subsets, and a LOO-type analysis is performed at the level of the subsets. Note that  $k$ -fold CV is computationally much more feasible than testing all possible ways of splitting up the data, but there is a trade-off: picking small  $k$  increases the variance of the CVE estimate, while picking large  $k$ , which tends toward LOOCV, is biased for large sample sizes.

A common way to overcome the artificial trade-off between bias and variance imposed by  $k$ -fold CV, and still offer computational tractability, is Monte-Carlo cross validation (MCCV) [145]. MCCV randomly splits the data  $m$  times with fixed  $n_f$  and  $n_v$  (size of training and test sets respectively) over the  $m$  iterations. For each iteration, the CVE is computed using the respective training and test sets; the overall CVE is estimated using the mean of these  $m$  CVEs. If  $\frac{n}{n_v} \ll m \ll \binom{n}{n_v}$ , MCCV estimates

### CHAPTER 3. WALKING DYNAMICS ARE SYMMETRIC (ENOUGH)

the CVE with a computationally feasible sample size, and with negligible variance compared to the estimate provided by  $k$ -fold CV. Also, since we fit the model more times ( $m \gg k$ ), MCCV provides a better mechanism for estimating model uncertainty than  $k$ -fold CV.

As mentioned before, the model being fit to input–output data in our case is a linear map. Suppose there are  $n$  pairs of input–output data,  $(x_i, y_i)$ , where  $i \in \mathcal{I} = \{1, 2, 3, \dots, n\}$ . Split this data into a training set  $\mathcal{F} \ni (x_f, y_f)$  comprising  $n_f$  pairs, and test set  $\mathcal{V} \ni (x_v, y_v)$  comprising  $n_v$  pairs. Define  $X_{\mathcal{F}}$  as the matrix whose rows are  $x_f^T$ , and define  $Y_{\mathcal{F}}$ ,  $X_{\mathcal{V}}$ , and  $Y_{\mathcal{V}}$  similarly. We use the following definition of CVE from  $\mathcal{F}$  to  $\mathcal{V}$ :

$$\text{CVE}_{\mathcal{F} \rightarrow \mathcal{V}} := \frac{\|Y_{\mathcal{V}} - X_{\mathcal{V}}A_{\mathcal{F}}^T\|^2}{\|Y_{\mathcal{V}}\|^2} \quad (3.15)$$

where  $\|\cdot\|$  denotes the Frobenius norm and

$$A_{\mathcal{F}} := \left( X_{\mathcal{F}}^\dagger Y_{\mathcal{F}} \right)^T \quad (3.16)$$

is the least-squares solution (3.14) given the training data  $\mathcal{F}$ .

Our extension of this classical CV is for systems that may exhibit discrete symmetry. We focus our discussion and notation on human walking, but these methods are applicable to other forms of locomotion that involve nearly bilaterally symmetric gaits, e.g. walking and trotting, but not clearly asymmetric gaits, e.g. galloping [38].

### CHAPTER 3. WALKING DYNAMICS ARE SYMMETRIC (ENOUGH)

In classical Monte Carlo CV, at each iteration, one CVE is computed using (3.15), where as in our extended CV method we compute three types of CVEs. Each CVE computation uses the same test set, but the models are fit using three different training sets.

Each application of extended CV requires a “normal” set,  $\mathcal{N}$ , and an equal size “mirrored” set,  $\mathcal{M}$ . In this thesis, we analyze four different  $(\mathcal{N}, \mathcal{M})$  pairs, which are generated using the input–output data types illustrated in Fig. 3.2, i.e. step-to-step transitions ( $\{L \mapsto R\}$  and  $\{R \mapsto L\}$ ) and stride-to-stride transitions ( $\{L \mapsto L\}$  and  $\{R \mapsto R\}$ ). For example, if the normal data set comprises the left-to-right step transitions,  $\mathcal{N} = \{L \mapsto R\}$ , the associated mirrored dataset is  $\mathcal{M} = \{R \mapsto L\}$ . Similarly, for strides, if  $\mathcal{N} = \{L \mapsto L\}$  represents the set of all transitions from left heel strike to the subsequent left heel strike, then  $\mathcal{M} = \{R \mapsto R\}$  are the corresponding right-to-right transitions. All  $(\mathcal{N}, \mathcal{M})$  combinations are listed in Table 3.1.

The normal and mirrored sets *each* include  $n$  mutually exclusive input–output pairs, denoted by  $(x_i, y_i) \in \mathcal{N}$  and  $(\hat{x}_i, \hat{y}_i) \in \mathcal{M}$ , respectively where  $i \in \mathcal{I} = \{1, 2, \dots, n\}$ . Each iteration of extended CV randomly splits this index set  $\mathcal{I}$  into a training index set  $\mathcal{I}_f$  and test index set  $\mathcal{I}_v$  in a manner identical to classical CV:  $\mathcal{I}_f \cup \mathcal{I}_v = \mathcal{I}$  and  $\mathcal{I}_f \cap \mathcal{I}_v = \emptyset$ . The three types of CVE computations described below draw the test set from the normal dataset:

$$\mathcal{V} = \{(x_v, y_v) \in \mathcal{N} \mid v \in \mathcal{I}_v\}. \quad (3.17)$$

CHAPTER 3. WALKING DYNAMICS ARE SYMMETRIC (ENOUGH)

*Normal Cross Validation (NCV)* is the same as classical Monte Carlo CV, in that the training data are also drawn from  $\mathcal{N}$ :

$$\mathcal{F}_{\text{NCV}} = \{(x_f, y_f) \in \mathcal{N} \mid f \in \mathcal{I}_f\}. \quad (3.18)$$

This set is used for fitting the linear model  $A_{\mathcal{F}_{\text{NCV}}}$  using (3.16). Given  $A_{\mathcal{F}_{\text{NCV}}}$ , the CVE is computed on the common test set  $\mathcal{V}$  using (3.15). For NCV, the mirrored data  $\mathcal{M}$  is not used.

*Mirrored Cross Validation (MCV)* draws the training data from the mirrored dataset  $\mathcal{M}$ , using the same training index set  $\mathcal{I}_f$  as NCV:

$$\mathcal{F}_{\text{MCV}} = \{(\hat{x}_f, \hat{y}_f) \in \mathcal{M} \mid f \in \mathcal{I}_f\}. \quad (3.19)$$

As before, this set is used for computing the linear model  $A_{\mathcal{F}_{\text{MCV}}}$  using (3.16). The common test set  $\mathcal{V}$  is used for computing the CVE. In MCV, we are using the “wrong” training data (mirrored), which will be critical to detect dynamical asymmetry in walking. Note that the size (and in fact the indices) of the training data in both MCV and NCV are the same.

*Combined Cross Validation (CCV)* uses training data that is the union of the training sets from NCV and MCV:

$$\mathcal{F}_{\text{CCV}} = \mathcal{F}_{\text{NCV}} \cup \mathcal{F}_{\text{MCV}}. \quad (3.20)$$

### CHAPTER 3. WALKING DYNAMICS ARE SYMMETRIC (ENOUGH)

And, as before, this data is used to fit the linear model  $A_{\mathcal{F}_{CCV}}$  and the common test set  $\mathcal{V}$  is used for calculating the CVE. Thus the model is fitted on data pooled from both  $\mathcal{N}$  and  $\mathcal{M}$ , while the test data remains the same. Note that CCV uses twice as much data for fitting as either NCV or MCV.

Fig. 3.3 illustrates the set partitioning for one iteration of extended cross validation for a general dataset. Fig. 3.4(a) illustrates one iteration of the extended cross validation algorithms on step data, where the normal dataset is  $\mathcal{N} = \{L \mapsto R\}$  and the mirrored dataset is  $\mathcal{M} = \{R \mapsto L\}$ . Fig. 3.4(b) illustrates one iteration of the extended cross validation algorithms on stride data where  $\mathcal{N} = \{L \mapsto L\}$  and  $\mathcal{M} = \{R \mapsto R\}$ .

Table 3.1: Catalog of normal,  $\mathcal{N}$ , and associated mirrored,  $\mathcal{M}$ , datasets combinations used in our extended CV analysis.

	$\mathcal{N}$	$\mathcal{M}$
Step	$\{L \mapsto R\}$	$\{R \mapsto L\}$
	$\{R \mapsto L\}$	$\{L \mapsto R\}$
Stride	$\{L \mapsto L\}$	$\{R \mapsto R\}$
	$\{R \mapsto R\}$	$\{L \mapsto L\}$

The comparison between NCV and MCV will be critical for statistically testing the symmetry of human walking. Since both NCV and MCV have training sets of the same size and MCV uses mirrored data, the difference in CVEs offer a direct measure of dynamical asymmetry. For a symmetric system NCV and MCV errors should be statistically indistinguishable. If there are asymmetries, we should observe higher MCV errors than NCV errors.

However, this comparison alone is not enough to address all concerns because

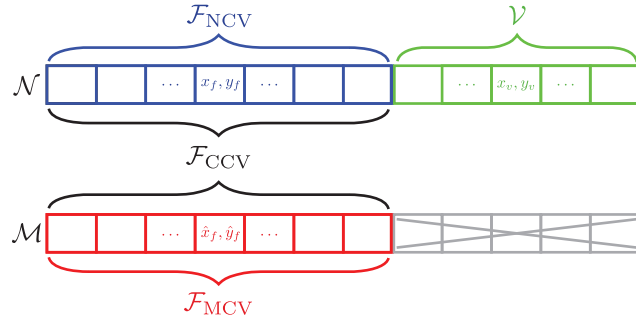


Figure 3.3: **Illustration of the subsets  $\mathcal{V}$ ,  $\mathcal{F}_{\text{NCV}}$ ,  $\mathcal{F}_{\text{MCV}}$ , and  $\mathcal{F}_{\text{CCV}}$  after random splitting during an iteration of extended cross validation methods.** The normal dataset,  $\mathcal{N}$ , is randomly split into the normal training set  $\mathcal{F}_{\text{NCV}}$  and the common test set  $\mathcal{V}$ .  $\mathcal{F}_{\text{MCV}}$  shares the same indices as  $\mathcal{F}_{\text{NCV}}$  but is drawn from the mirrored dataset,  $\mathcal{M}$ . The training set for the CCV is simply the union of the other two training sets:  $\mathcal{F}_{\text{CCV}} = \mathcal{F}_{\text{NCV}} \cup \mathcal{F}_{\text{MCV}}$ . Note that the subset  $\mathcal{M} \setminus \mathcal{F}_{\text{MCV}}$  (greyed out) is not used in any of the three CV computations.

the main advantage of assuming symmetry is that we double the amount of data by combining the normal and mirrored data sets and fitting a single model. We introduce a potential bias by neglecting the asymmetries in the behavior, but reduce the variance in the estimation by simply doubling the amount of data used for fitting. From this perspective, comparison between NCV and CCV will be critical for statistically testing predictive powers of asymmetric and symmetric modeling approaches, which is an effective way testing the “usefulness” of the symmetry assumption.

### 3.4 Results

The results presented here are based on the methods presented in Section 3.3.1 which rely on Monte-Carlo sampling and cross-validation. The results presented

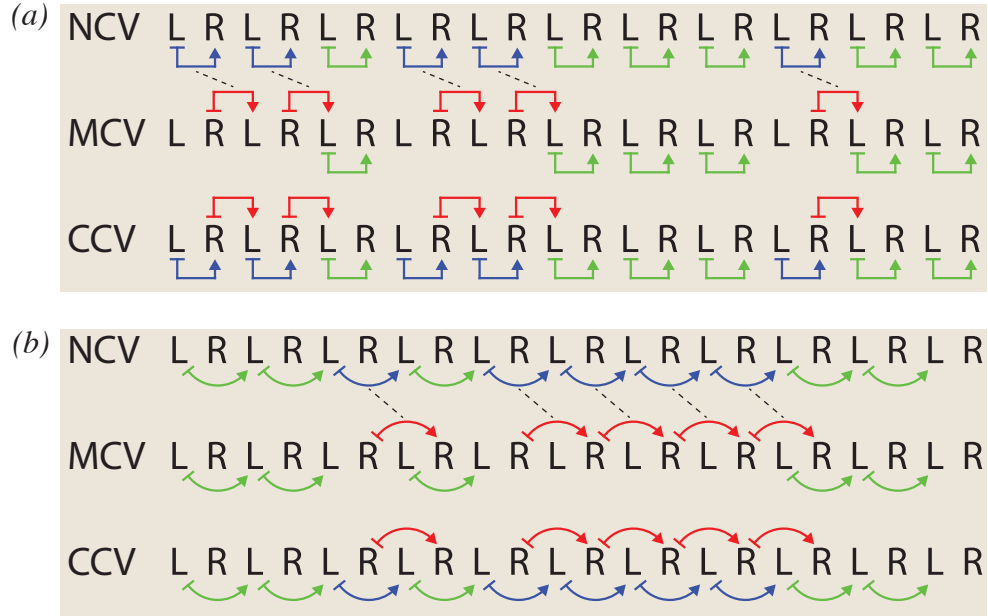


Figure 3.4: **Illustration of extended CV dataset partitioning.** (a) For step-to-step data, the normal dataset ( $\mathcal{N}$ ) comprises all left-to-right step ordered pairs, whereas the mirrored dataset ( $\mathcal{M}$ ) comprises all right-to-left step ordered pairs. (b) For stride-to-stride data, the normal dataset ( $\mathcal{N}$ ) comprises all left-to-left stride ordered pairs, whereas the mirrored dataset ( $\mathcal{M}$ ) comprises all right-to-right stride ordered pairs. In both cases, for each iteration, a common test set ( $\mathcal{V}$ , green arrows), used for all CV methods, is randomly sampled from the normal dataset. The training sets, however, are unique to each method. NCV: the remainder of the normal dataset is used for training ( $\mathcal{F}_{\text{NCV}}$ , blue arrows). MCV: the training set ( $\mathcal{F}_{\text{MCV}}$ , red arrows) is obtained using the same indices (dashed lines) as for  $\mathcal{F}_{\text{NCV}}$ . CCV: the union of the test sets for NCV and MCV, comprise the combined training data ( $\mathcal{F}_{\text{CCV}} = \mathcal{F}_{\text{NCV}} \cup \mathcal{F}_{\text{MCV}}$ , red and blue arrows).

below were qualitatively similar (and stronger in one case) to those obtained using the bootstrap method—see Appendix.

We set the sample size of Monte-Carlo iterations to  $m = 1000$  based on pilot experiments, which showed that increasing the sample size beyond this had a negligible effect on cross validation error. In each iteration, 20% ( $\frac{n_v}{n} = 0.2$ ) of the normal data set,  $\mathcal{N}$ , was withheld for validation. Training sets for the three CV computations were drawn from the remaining data according to the procedure detailed in Section 3.3.1.

### 3.4.1 Symmetric vs. Asymmetric Modeling

The question being addressed in this thesis is not just the symmetry versus asymmetry of the dynamics of human walking, but also the statistical consequences of choosing one approach over the other. We applied our extended cross-validation method (Section 3.3.1) to expose these consequences.

#### 3.4.1.1 Step Maps

To apply the extended CV to step-to-step transitions, we analyzed both combinations of normal and mirrored data:  $(\mathcal{N}, \mathcal{M}) = (\{L \mapsto R\}, \{R \mapsto L\})$  and  $(\mathcal{N}, \mathcal{M}) = (\{R \mapsto L\}, \{L \mapsto R\})$ ; see Table 3.1. For each category of cross validation—NCV, MCV, and CCV—we averaged the errors for both combinations of  $(\mathcal{N}, \mathcal{M})$ .

Fig. 3.5(a) compares MCV and CCV errors to NCV error from step-to-step data. MCV errors are (statistically) significantly higher than NCV errors at all speeds

## CHAPTER 3. WALKING DYNAMICS ARE SYMMETRIC (ENOUGH)

( $p_{1.5m/s} = 0.004$ ,  $p_{1m/s} = 0.008$  and  $p_{0.5m/s} = 0.004$ ; one-sided Wilcoxon rank-sign test). This shows that our data is indeed dynamically asymmetric between  $L \mapsto R$  and  $R \mapsto L$ .

The comparison of CCV and NCV errors illuminates a different perspective (Figure 3.5(a)). For speeds of 1.5 m/s and 1.0 m/s CCV and NCV errors were statistically indistinguishable ( $p_{1.5m/s} = 0.38$  and  $p_{1m/s} = 0.84$ ; Wilcoxon rank-sign test), suggesting that for these speeds, the predictive power of a model that assumes symmetry is just as great as one that embraces the asymmetry. More surprisingly, the average CCV error for the slowest speed tested was (statistically) significantly lower than the average NCV error ( $p_{0.5m/s} = 0.0039$ . Wilcoxon one-sided rank-sign test) for the slowest speed (0.5m/s). In other words, assuming symmetry (CCV) produces a single step-to-step model that has greater predictive power than is achieved by refining the analysis to produce separate  $\{L \mapsto R\}$  and  $\{R \mapsto L\}$  step maps.

### 3.4.1.2 Stride Maps

We analyzed the dynamical symmetry and the statistical consequences of symmetric modeling on the stride-to-stride transitions. Similar to before, we analyzed two different  $(\mathcal{N}, \mathcal{M})$  combinations,  $(\mathcal{N}, \mathcal{M}) = (\{L \mapsto L\}, \{R \mapsto R\})$  and  $(\mathcal{N}, \mathcal{M}) = (\{R \mapsto R\}, \{L \mapsto L\})$ ; see Table 3.1. And again, for each category of cross validation, we averaged the CV errors for both combinations of normal and mirrored data. As in the previous section, we first compared NCV and MCV errors to test if the

CHAPTER 3. WALKING DYNAMICS ARE SYMMETRIC (ENOUGH)

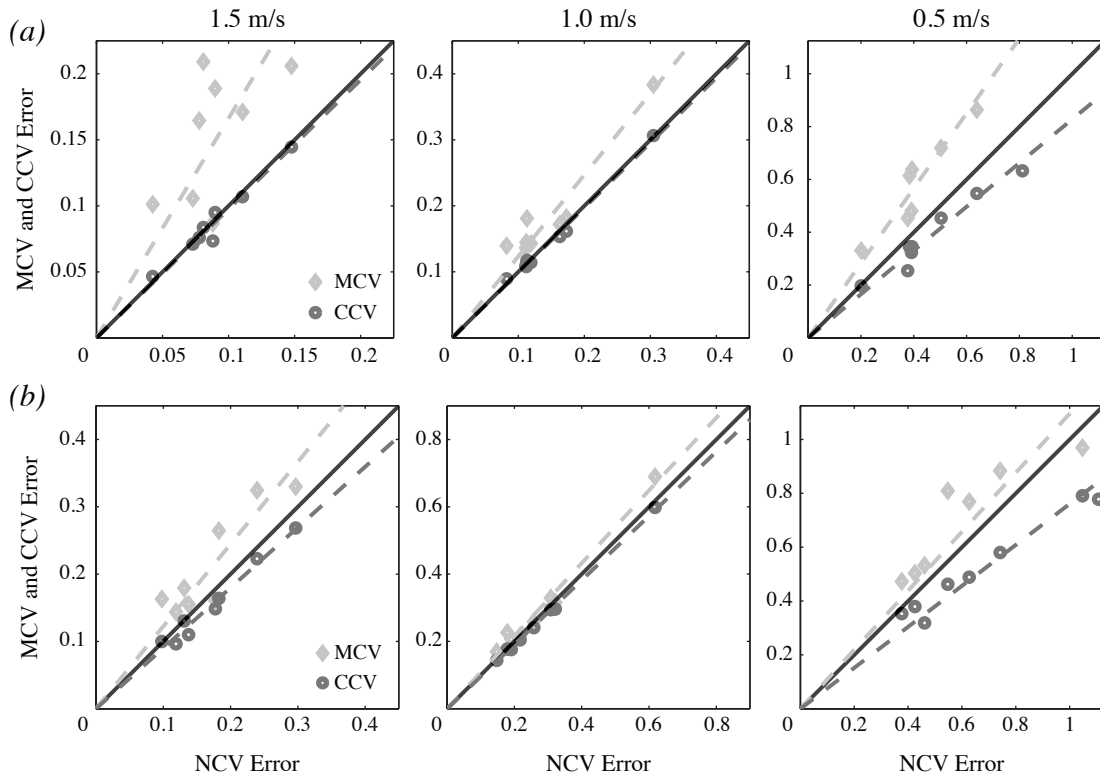


Figure 3.5: **Walking is asymmetric, but neglecting this can nevertheless improve fitting.** (a) Step-to-step maps. At all speeds, the mean mirrored cross validation errors (light grey diamonds) were significantly worse than for normal cross validation, indicating that steps were indeed asymmetric. Despite this left–right asymmetry, the mean combined cross validation errors were not significantly different than for normal cross validation at the two fastest walking speeds tested, and, more surprisingly, were actually *lower* at the slowest walking speed. The slopes of the fitted lines (dashed) determine the relative increase ( $m > 1$ ) or decrease ( $m < 1$ ) in CV error relative to the NCV error. (b) Stride-to-stride maps. By the same statistical measure, strides were also asymmetric at all speeds, but less substantially so. Moreover, the mean CCV error was lower than mean NCV error at all speeds.

## CHAPTER 3. WALKING DYNAMICS ARE SYMMETRIC (ENOUGH)

stride-to-stride data is statistically asymmetric. The NCV and CCV errors were also compared in order to compare the symmetric and asymmetric modeling approaches.

Fig. 3.5(b) compares the MCV and CCV errors to NCV error for stride-to-stride data. MCV errors were higher (on average) than NCV errors for all speeds and these differences were statistically significant ( $p_{1.5m/s} = 0.0391$ ,  $p_{1m/s} = 0.0117$  and  $p_{0.5m/s} = 0.0039$ ; paired one-sided Wilcoxon rank-sign test). This shows that our data is dynamically asymmetric between  $L \mapsto L$  and  $R \mapsto R$ .

However, the comparison of NCV and CCV errors in stride-to-stride data is more striking than in the step-to-step case in that CCV errors were statistically significantly lower than the NCV errors at all three speeds ( $p_{1.5m/s} = 0.004$ ,  $p_{1m/s} = 0.012$  and  $p_{0.5m/s} = 0.004$ ; paired one-sided Wilcoxon rank-sign test).

### 3.4.1.3 Model Uncertainty

Cross-validation errors are powerful metrics for comparing the effectiveness of symmetric and asymmetric modeling approaches. However, if two models have similar CVEs, the next thing to address is how well the data constrain the two models—i.e. how much *uncertainty* there is in the model parameters [109]. This was particularly important for our step-to-step data because symmetric and asymmetric modeling produced indistinguishable CVEs for 1.5 and 1.0m/s walking. This implies that both modeling approaches are equally powerful from the perspective of CVE. However, the parameters of the fitted section map model may exhibit greater variability for the

### CHAPTER 3. WALKING DYNAMICS ARE SYMMETRIC (ENOUGH)

asymmetric modeling approach since it uses less data for fitting.

In order to measure the uncertainty of the models, we adopted following metric:

$$\Xi = \sum_{i=1}^d \sum_{j=1}^d \sigma_{ij}^2 \quad (3.21)$$

where  $\sigma_{ij}^2$  is the sample variance of  $a_{ij}$ , i.e. element at the  $i^{th}$  row and  $j^{th}$  column of the section map  $A_{\mathcal{F}}$  fit during Monte-Carlo iterations of the extended CV method. Symmetric model uncertainty was computed using the fitted matrix samples of the CCV method. Model uncertainties of the  $\{L \mapsto R\}$  and  $\{R \mapsto L\}$  (and  $\{L \mapsto L\}$  and  $\{R \mapsto R\}$ ) maps were averaged to have a single asymmetric model uncertainty for step maps (and stride maps).

We found that by neglecting asymmetry and fitting a single return map, there was a substantial reduction in model uncertainty for both the step-to-step and stride-to-stride data. See Figure 3.6. Thus, even though in a few cases, the CV errors were similar for NCV and CCV, the models produced using CCV (that is, neglecting asymmetry and pooling the data) are substantially less variable.

For step maps, assuming symmetry substantially lowers model uncertainty: we saw 56%, 54%, and 72% improvement with symmetric approach for speeds 1.5, 1.0 and 0.5 m/s respectively. All improvements were statistically significant ( $p = 0.0039$ , one-sided Wilcoxon signed-rank test). We observed the same trend with stride maps: 61%, 58%, and 74% improvement with symmetric approach for speeds 1.5, 1.0 and 0.5

## CHAPTER 3. WALKING DYNAMICS ARE SYMMETRIC (ENOUGH)

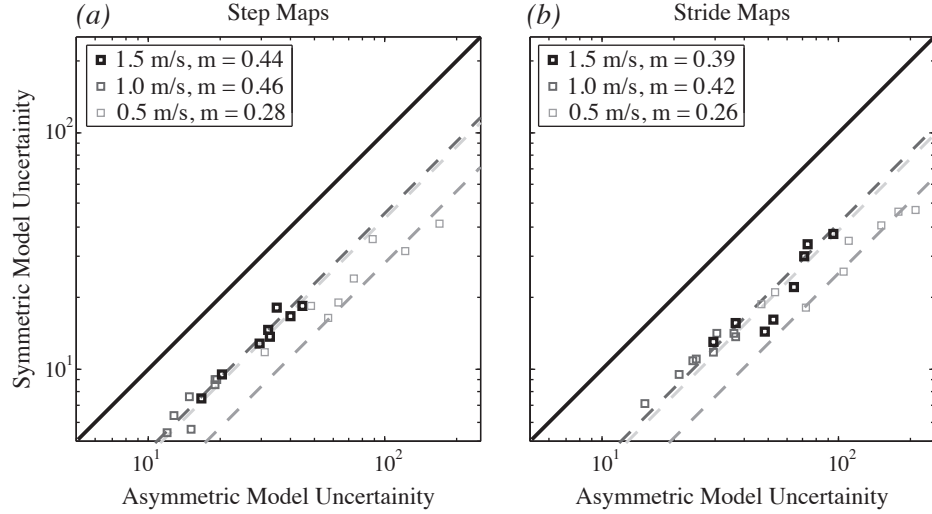


Figure 3.6: **Model uncertainty at all three speeds was lower when symmetry was assumed in both (A) step-to-step and (B) stride-to-stride maps.** Each marker compares the model uncertainty with asymmetry and with symmetry of a single individual. Dashed line denotes the best fitted line (passing through the origin) to the comparison markers. The percentage improvement is given by  $(1 - m) \times 100$ , where  $m$  is the slope of the fitted line.

m/s respectively ( $p = 0.0039$ , one-sided Wilcoxon signed-rank test). See Figure 3.6.

### 3.4.2 Step Return Maps vs. Stride Return Maps

One of the advantages of assuming dynamical bilateral symmetry (i.e. neglecting asymmetry) is that one step becomes the fundamental period of the system: the mapping from step to step defines the return map of the dynamics. On the contrary, if we embrace the asymmetry, the stride becomes the fundamental period. The disadvantage of using stride-to-stride return maps compared to step-to-step maps is a potential loss of signal-to-noise ratio due to the fact that stride maps reduce the temporal resolution. Thus, one can expect that stride-to-stride return maps would

have lower predictive power in the CV setting.

In order to compare the predictive powers of step and stride return maps, we analyzed the CVEs by assuming symmetry and fitting lumped return maps to both step and stride data. Specifically we compared the CCV errors of step and stride data in our method. In order to estimate CCV error of step return map, we take the mean of CCV errors of  $\{L \mapsto R\}$  and  $\{R \mapsto L\}$ . Likewise, in order to estimate CCV error of stride return map, we take the mean of CCV errors of  $\{L \mapsto L\}$  and  $\{R \mapsto R\}$ .

The results illustrated in Fig. 3.7 show that there is a dramatic signal-to-noise ratio loss with stride-to-stride return maps and that step-to-step return maps have more predictive power in the CV setting. CCV errors of stride return maps are significantly higher than the ones with step return maps: 79%, 87%, and 31% more CV error with stride return maps for speeds 1.5, 1.0, and 0.5 m/s respectively. The differences are statistically significant ( $p = 0.0039$ , one-sided Wilcoxon signed-rank test).

## 3.5 Discussion

In this chapter, we focused our attention on bilateral dynamic asymmetry in human walking. Specifically, we introduced a statistical framework based on applying cross validation techniques and fitting linear maps to the data associated with the heel strike events. Our statistical methods allowed us to examine the “wrongness”

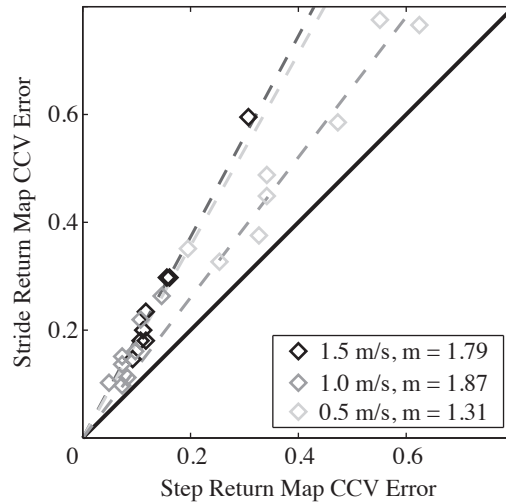


Figure 3.7: **Illustration of the CCV errors of step return maps and stride return maps.** Each marker compares the CCV errors of step and stride return maps of a single individual. Dashed lines illustrate the best fitted lines (passing through the origin) to the comparison markers with  $m$  being the associated slope of the line.

and “usefulness” of neglecting bilateral dynamic asymmetry.

We applied our methods to data obtained from eight different individuals walking at three different speeds. Based on the results obtained with this data set, we observed that dynamical asymmetry in walking is significant and statistically distinguishable. These results underscore what several studies have previously observed on steady-state parameters [1, 45, 59, 77, 103, 105, 122, 151].

Despite the existence of significant asymmetry, we show that ignoring this and modeling human walking dynamics as symmetric produces significantly more consistent models (see Fig. 3.6). Moreover, the predictive power of these symmetric models is higher than (or at worst equal to) their asymmetric counterparts (see Fig. 3.5). This shows that neglecting bilateral asymmetry—an inescapable characteristic of the

### CHAPTER 3. WALKING DYNAMICS ARE SYMMETRIC (ENOUGH)

human form—not only provides modeling convenience but, more importantly, produces better models in terms of consistency and predictive power. It is not only “OK” to neglect asymmetry; in some cases, it is better.

One should also note that the slight differences between two “symmetrically” placed sensors (e.g. load cells) can generate an appearance of asymmetry that is not related to the actual system. However, we suspect that these asymmetries dominantly affect the limit-cycle symmetry—because their effects are persistent and almost same for each cycle—and by approaching the problem from the dynamical symmetry perspective, we minimize asymmetries in the data associated with the measurement bias. In our case, this point is moot: despite possible measurement asymmetries that would likely exacerbate asymmetries in modeling, a symmetric dynamic model was still preferable for our data.

Even though we applied our methods to human walking data, they are directly applicable to a wide range of rhythmic dynamical systems in biology and robotics. Specifically, we are interested in behaviors that exhibit alternating (out of phase) gait patterns but are symmetric via reversing the left–right axis for half the stride. This class includes bipedal walking, running, and sprinting [39, 110]; quadrupedal walking, trotting, and pacing [21, 38]; hexapedal alternating tripod gait [63, 136]; and even swimming [91, 142].

In the context of robotics, our methods can be used for diagnostics and calibration since symmetry is considered a desirable property in the design and development

### CHAPTER 3. WALKING DYNAMICS ARE SYMMETRIC (ENOUGH)

of robotic systems. Asymmetric robotic gaits can potentially increase energy expenditure, reduce performance, and introduce a steering bias, hindering the control and operation of the robot. It may be possible to eliminate this steering bias by using existing gait adaptation methods [64, 164] which, to date, requires external instrumentation and specialized arenas. However, our method relies on only internal kinematic measurements, which are directly available in most robotic systems, and so perhaps the methods presented in this chapter can be used to develop fast and effective calibration methods for field robotics.

On the biological side, there is scientific value in investigating dynamical symmetry across species. Models of biological locomotion can be decomposed into two components: the mechanics of the locomotion (plant), and the neural feedback (controller) [132]. A “less wrong” model of the plant provides better understanding of the controller, and vice-versa [40, 41]. The locomotor pattern of a behaving animal is the closed-loop interaction of the plant and controller. Investigating dynamical symmetry (or asymmetry) in the locomotor gait as well as symmetry (or asymmetry) of the kinematics allows us to better predict the structure of the corresponding neural controller.

With regard to human health in particular, our tools may be useful for understanding motor deficits during locomotion. Specifically, these methods provide an important extension to those that center on kinematic symmetry and its relations to human physiology [57, 126]. Individuals with damage to the musculoskeletal system

### CHAPTER 3. WALKING DYNAMICS ARE SYMMETRIC (ENOUGH)

or nervous system often use asymmetric kinematic walking patterns (e.g. amputees, stroke patients). The kinematic asymmetry can be in the amount of time standing on one leg versus the other, the extent of limb movements, or some combination. An understanding of the underlying dynamical asymmetry (or even symmetry) in these cases would provide more information about the nature of the deficit, and perhaps suggest new targets for focusing rehabilitation treatments.

Finally, an interesting extension of our methods would be analyzing *dynamical* asymmetry in gaits with categorically asymmetric steady-state kinematics such as quadrupedal galloping and bounding. The steady-state limit-cycles of such gaits are obviously asymmetric, but the dynamics around those limit-cycles may be symmetric (enough).

## Chapter 4

# System Identification of Rhythmic Systems

Few tools exist for identifying the dynamics of rhythmic systems from input–output data. This chapter investigates the system identification of stable, rhythmic hybrid dynamical systems, i.e. systems possessing a stable limit cycle but that can be perturbed away from the limit cycle by a set of external inputs, and measured at a set of system outputs. By choosing a set of Poincaré sections, we show that such a system can be (locally) approximated as a linear discrete-time periodic system. To perform input–output system identification, we transform the system into the frequency domain using discrete-time harmonic transfer functions. Using this formulation, we present a set of stimuli and analysis techniques to recover the components of the HTFs nonparametrically. We demonstrate the framework using a hybrid

spring-mass hopper. Finally, we fit a parametric approximation to the fundamental harmonic transfer function and show that the poles coincide with the eigenvalues of the Poincaré return map.

## 4.1 Introduction

In this chapter, we propose a framework for system identification of rhythmic hybrid dynamical systems around their limit cycles. Rhythmic dynamic behaviors can be observed in a wide variety of biological and robotics systems, such as terrestrial locomotion [19, 39, 136, 150] and juggling [10, 22, 137]. Such behaviors often include hybrid characteristics in that they exhibit both smooth flows punctuated by discrete jumps and are often modeled as hybrid dynamical systems [26, 86].

Powerful analytical and numerical tools have been developed in order to control and analyze such hybrid dynamical systems and behaviors [3, 4, 29, 86]. However, these tools are limited to the case when we have a full (and preferably simple) mathematical model—typically derived from first principles—that can accurately describe the system dynamics, but such modeling requires many creative decisions about what to neglect. More critically, it is impossible to derive equations, from first principles, that capture the influence of the nervous system on these hybrid dynamics [40, 132, 158].

In the context of non-rhythmic dynamical systems near equilibria, system identification is a mature field [108, 149]. System ID provides a very powerful complement to

## CHAPTER 4. IDENTIFICATION OF RHYTHMIC SYSTEMS VIA HTF

modeling systems using first principles. A system identification method can solely rely on data driven approaches, these class of algorithms are called “black-box” methods, or it can combine a data driven approach with some priori information (which may be provided by first principles) and these kind of algorithms are called “grey-box” methods.

By contrast, system ID for rhythmic and/or hybrid systems remains radically limited. Several researchers have addressed system ID and analysis of rhythmic systems by studying the steady state behavior and synthesizing these results using dynamical systems language [95]. Most popular of such an approach is using SLIP (spring-loaded intervened pendulum) and its extensions for modeling legged locomotion in animals [7, 61, 68]. However, this type of approach is extremely limited for answering the question of such as how these systems recover from perturbations.

There are also recent studies that attempt to estimate and quantify the dynamics around the limit cycles of such systems from data [10, 127, 129]. The most popular mathematical framework used in such analysis is based on Poincaré return maps which reduce the rhythmic dynamical system to a lower dimensional discrete-time system that describes the behavior in terms of its cycle-to-cycle transitions. Linearization of this reduced system yields a discrete time LTI system. The power of Poincaré theory is that it connects rhythmic dynamical systems to LTI systems theory, affording rich and powerful tools for both analysis and identification. However, the obvious limitation of this approach is that only one measurement per cycle is used. But, there

## CHAPTER 4. IDENTIFICATION OF RHYTHMIC SYSTEMS VIA HTF

are other limitations to this approach. The approach lumps all effects within a cycle together, making it difficult to relate system-level dynamics with the roles of individual component-level details. Relatedly, there is a severe loss in temporal resolution. In addition, the approach presumes access to *all* state variables, an assumption not realistic when dealing with neural control systems.

In order to resolve some of these issues, Revzen et al. [127] introduced an identification framework inspired by Floquet theory and it utilizes multiple sections within a cycle and identifies mappings between them. However, this approach is “input free” and the identification is performed only based on the output measurements (and thus doesn’t address the problem of hidden states). Typically, for the identification of dynamical systems input–output methods are more powerful and accurate compared to output only methods.

Kiemel et al. [93] proposed a new formulation that addresses the input–output identification of rhythmic systems around their limit cycles in the frequency domain. Specifically they approximate the dynamics near the limit cycle as a linear time-periodic (LTP) system. In this framework, they non-parametrically estimate LTP dynamics in frequency domain using harmonic transfer functions [117, 166]. However, the assumption of smooth dynamics does not readily apply to many rhythmic behaviors that involve hybrid dynamic characteristics.

In order to fill these gaps, we propose a new formulation for hybrid rhythmic dynamic systems using discrete time harmonic transfer functions that enables us to

perform input–output system ID in frequency domain.

### 4.1.1 Dissemination

Some figures and the portions of text presented in Chapter 3 have been reported in a conference paper [6].

## 4.2 Hybrid Dynamical System Formulation with Exogenous Input

The section follows briefly summarizes the development of [86] and modifies it to include exogenous inputs.

The state space of a hybrid system is a union

$$V = \bigcup_{\alpha \in \mathcal{I}} V_{\alpha}$$

where  $\mathcal{I}$  is a finite *index set* and each  $V_{\alpha}$  is an open, connected subset of  $\mathbb{R}^{n_{\alpha}}$ . Each element of this union, i.e.  $V_{\alpha}$ , is called a *chart*. Note that for some  $\alpha, \beta \in \mathcal{I}$  it is possible to have a nonempty intersection set, i.e.  $V_{\alpha} \cap V_{\beta} \neq \emptyset$  and there is no continuity requirement on these intersection sets. The dimension of the charts can typically depend on  $\alpha$  [25, 26, 165]. A state of the overall hybrid dynamical system consists of an index  $\alpha$  together with a point in the chart  $V_{\alpha}$ . We assume that a

## CHAPTER 4. IDENTIFICATION OF RHYTHMIC SYSTEMS VIA HTF

(smooth) continuous time dynamical system is defined on each chart. Since  $V_\alpha \subset \mathbb{R}^{n_\alpha}$  we can represent the smooth dynamical system on each chart using

$$\dot{q}_\alpha = f_\alpha(q_\alpha, u_\alpha, t) \quad (4.1)$$

where  $\dot{q}_\alpha \in V_\alpha$  is the state of the vector-field associated with chart  $\alpha$  and  $u \in \mathbb{R}^{l_\alpha}$  represents the small external perturbations used for system identification. One should also note that, similar to the state vector  $q_\alpha$ , dimension of the exogenous input may depend on  $\alpha$  for hybrid dynamical systems. Indeed, exogenous inputs may not available ( $l_\alpha = 0$ ) for some charts. As a convenience of notation, and without loss of generality we assume that there exists a  $\hat{u} \in \mathbb{R}^{l_{\max}}$  which can be freely controlled by the experimenter, and a set of coordinate dependent mappings,  $g_\alpha : \mathbb{R}^{l_{\max}} \rightarrow \mathbb{R}^{l_\alpha}$ , such that  $l_{\max} = \max_{\alpha \in \mathcal{I}} l_\alpha$  and  $u_\alpha = g_\alpha(\hat{u}), \forall \alpha$ . These maps should be locally onto (so as not to throw away “useful” perturbation inputs), and without loss of generality,  $g_\alpha(0) = 0$ . On charts for which  $l_{\max} > l_\alpha$ , the extra inputs are “thrown away” by the dynamics. Under these constraints (4.1) takes the form

$$\dot{q}_\alpha = f_\alpha(q_\alpha, \hat{u}, t) \quad (4.2)$$

We assume that for each  $\alpha \in I$ , there exists a finite set of real-valued piecewise-smooth threshold functions,  $h_\alpha^{\beta_i}(q_\alpha, \hat{u})$ . Zero crossings of a threshold function is called an *event* which triggers the transition to a new chart indexed by  $\beta_i$ . We further assume that

## CHAPTER 4. IDENTIFICATION OF RHYTHMIC SYSTEMS VIA HTF

there are transition maps,  $q_\beta = T_\alpha(q_\alpha, \hat{u})$  that apply a transformation to the points at an event. The images of the transition maps are taken as initial conditions for the continuous-time trajectory inside the new chart. Conceptually, the evolution of the system is viewed as a sequence of trajectory segments where the endpoint of one segment is connected to the initial point of the next by a transition map.

Given an input  $\hat{u}(t)$ , an initial chart  $\alpha_0$ , and initial condition on that chart  $q_{\alpha_0}(t_0)$ , we define a trajectory on the interval  $[t_0, t_n]$  as follows. Denote events  $t_1, \dots, t_{n-1}$ , such that  $t_0 < t_1 < \dots < t_n$ . Each event time corresponds to a hybrid transition, giving rise to a sequence of discrete states  $\alpha_0, \dots, \alpha_{n-1}$  and smooth trajectories  $q_{\alpha_i}(t) \in V_{\alpha_i}$ ,  $t \in [t_i, t_{i+1}]$ , such that each  $q_{\alpha_i}$  is a trajectory of the continuous-time dynamical system on  $V_{\alpha_i}$  given in (4.2). Further, the initial condition for each trajectory is given by  $q_{\alpha_i}$ , and for  $i = 1, \dots, n-1$ , these are calculated via the transition map:  $q_{\alpha_i}(t_i) = T_{\alpha_{i-1}}(q_{\alpha_{i-1}}(t_i), \hat{u}(t_i))$ .

In the absence of external inputs i.e.  $\hat{u}(t) = 0 \forall t$ , we assume the existence of an isolated, hybrid period orbit, or limit cycle,  $\gamma(t) \in V$ , that satisfies

$$\lim_{\hat{t} \rightarrow t^-} [\gamma(\hat{t}) - \gamma(\hat{t} + T)] = 0,$$

$$\lim_{\hat{t} \rightarrow t^+} [\gamma(\hat{t}) - \gamma(\hat{t} + T)] = 0.$$

Similar to the previous work on rhythmic hybrid dynamical systems [26], we limit our attention to hybrid systems undergoing a finite number of isolated hybrid transitions

near the limit cycle. We also assume that in a local neighborhood of the limit cycle that the number and order of hybrid transitions is fixed (although the transition times can and typically will vary) and both the threshold functions and transition maps associated with these transitions are locally smooth.

### 4.3 Mapping Between Poincaré Sections

A Poincaré section,  $\Sigma_i \subset V$ , is an embedded submanifold that intersects the periodic orbit at exactly one point [26]:

$$\{(\epsilon_i, \alpha_i)\} = \gamma \cap \Sigma_i, \quad \alpha_i \in \mathcal{I}, \epsilon_i \in V_{\alpha_i},$$

$$\dim(\Sigma_i) = \dim(V_{\alpha_i}) - 1$$

where  $(\epsilon_i, \alpha_i)$  is called the fixed point of  $\Sigma_i$ . The flow should be transverse to  $\Sigma_i$  in a neighborhood of  $\epsilon_i$  for all sufficiently small inputs. Let  $W_i \subset \Sigma_i$  be an open subset containing  $\epsilon_i$ .

Let  $\Sigma_j$  be another Poincaré section with associated fixed point  $(\epsilon_j, \alpha_j)$ . We define a mapping,  $P_{i \rightarrow j} : W_i \times R^{l_{\max}} \rightarrow \Sigma_j$  by assuming  $\hat{u} = u_i$  is constant (i.e. a “zero-order hold”) and tracing the hybrid trajectories from  $q_i \in W_i$  forward in time until it intersects  $\Sigma_j$  at  $q_j$ :

$$q_j = P_{i \rightarrow j}(q_i, u_i). \tag{4.3}$$

We assume that  $P_{i \rightarrow j}$  is a well-defined and smooth map around  $(\epsilon_i, 0)$ . If  $\Sigma_i = \Sigma_j$  and

CHAPTER 4. IDENTIFICATION OF RHYTHMIC SYSTEMS VIA HTF

$u_i = 0$  this maps becomes the more familiar Poincaré *return* map. It is natural to assume that our measurements of states  $q_i$  are indirect and through a smooth mapping:

$$z_i = h_i(q_i, u_i). \quad (4.4)$$

Linearizing state and output mappings in (4.3) and (4.4) around  $(q_i, q_j, u_i) = (\epsilon_i, \epsilon_j, 0)$  yields

$$\begin{aligned} x_j &= A_i x_i + B_i u_i, \\ y_i &= C_i x_i + D_i u_i. \end{aligned} \quad (4.5)$$

It is worth noting that  $A_i$  need not be square, depending on the dimensions of  $\Sigma_i$  and  $\Sigma_j$ . Now assume that we have  $N$  distinct isolated sequential (in the order they are punctuated by the limit cycle) Poincaré sections indexed by  $\{0, 1, \dots, N - 1\}$ ; see Fig. 4.1. We formulate the linearized mapping between consecutive sections using

$$\begin{aligned} x[n + 1] &= A[n]x[n] + B[n]u[n], \\ y[n] &= C[n]x[n] + D[n]u[n], \end{aligned} \quad (4.6)$$

where  $A[n] = A[n + N]$  (and likewise for  $B, C, D$ ).

The linearized mappings between successive Poincaré sections forms a linear discrete time periodic (LDTP) dynamical system which facilitates input–output modeling. Using (4.6) we can compute the linearized Poincaré return map at any section.

CHAPTER 4. IDENTIFICATION OF RHYTHMIC SYSTEMS VIA HTF

Let  $i \in \{0, \dots, N - 1\}$  be the section that we are interested. Then,

$$DP_{i \rightarrow i} = \prod_{k=i+N-1}^i A[k] = A[i + N - 1] \cdots A[i] \quad (4.7)$$

yields the linearized Poincaré return map at that section. It is obvious that for hybrid systems in which the dimension of charts ( $\dim(V_\alpha)$ ) changes with  $\alpha$ , the linearized Poincaré return map in (4.7) is always rank-deficient for some  $i \in \{0, \dots, N - 1\}$  [165]. It has been shown that the rank of a Poincaré return map is bounded above by the minimum dimension of all of the charts, i.e.

$$\text{rank}(DP_{i \rightarrow i}) \leq \min_{\alpha \in \mathcal{I}} \dim(V_\alpha) \quad (4.8)$$

or equivalently

$$\text{rank}(DP_{i \rightarrow i}) \leq \min_{j \in \{0, \dots, 1\}} d_j, \quad x_j \in R^{d_j}, \quad (4.9)$$

if there exists at least one Poincaré section in the chart with the minimum dimension.

Even with rank deficiencies and the dimension of  $x[n]$  is time varying, the linear time varying dynamics in (4.6) is suitable for deriving harmonic transfer functions using impulse response representation.

## 4.4 Harmonic Transfer Functions (HTF) for LDTP Systems

The computations above in Section 4.3 demonstrate that hybrid dynamical systems, operating near a limit cycle, can be approximated using a LDTP system. However, a transfer function representation may be more amenable to input-output system identification. In this section we will reformulate the derivations in [117] to suit LDTP systems. Any (causal) LDTP systems such as in (4.6) can be represented using time-periodic impulse response

$$y[n] = \sum_{k=0}^n H[n, k]u[k], \quad (4.10)$$

where  $H[n, k] = H[n - N, k - N]$ . For the sake of clarity of derivations, throughout the chapter we assume that  $N$  is even (easily relaxed). Let  $k = n - r$  then  $H[n, k] \mapsto H[n, n - r]$  which is periodic in  $n$  for any fixed  $r$  thus can be expressed as a Fourier series:

$$H[n, n - r] = \sum_{m=-\frac{N}{2}}^{\frac{N}{2}-1} H_m[r] e^{i\frac{2\pi m}{N}n}, \quad (4.11)$$

where

$$H_m[r] = \frac{1}{N} \sum_{n=-\frac{N}{2}}^{\frac{N}{2}-1} H[n, n - r] e^{-i\frac{2\pi m}{N}n}. \quad (4.12)$$

CHAPTER 4. IDENTIFICATION OF RHYTHMIC SYSTEMS VIA HTF

Plugging  $r = n - k$  gives

$$H[n, k] = \sum_{m=-\frac{N}{2}}^{\frac{N}{2}-1} H_m[n - k] e^{i\frac{2\pi m}{N}n}. \quad (4.13)$$

Combining (4.10) and (4.13),  $y[n]$  can be written as

$$\begin{aligned} y[n] &= \sum_{k=0}^n \sum_{m=-\frac{N}{2}}^{\frac{N}{2}-1} H_m[n - k] e^{i\frac{2\pi m}{N}n} u[k] \\ &= \sum_{m=-\frac{N}{2}}^{\frac{N}{2}-1} \sum_{k=0}^n H_m[n - k] e^{i\frac{2\pi m}{N}n} u[k] \\ &= \sum_{m=-\frac{N}{2}}^{\frac{N}{2}-1} \sum_{k=0}^n H_m[n - k] e^{i\frac{2\pi m}{N}(n-k)} u[k] e^{i\frac{2\pi m}{N}k} \\ y[n] &= \sum_{m=-\frac{N}{2}}^{\frac{N}{2}-1} \left( H_m[n] e^{i\frac{2\pi m}{N}n} * u[n] e^{i\frac{2\pi m}{N}n} \right). \end{aligned}$$

Taking the Z-transform of  $y[n]$ ,

$$Y(z) = \sum_{m=-\frac{N}{2}}^{\frac{N}{2}-1} H_m \left( z e^{-i\frac{2\pi m}{N}} \right) U \left( z e^{-i\frac{2\pi m}{N}} \right) \quad (4.14)$$

where

$$H_m(z) = \mathcal{Z} \{ H_m[n] \}. \quad (4.15)$$

We can obtain the frequency response version of the HTF equation in (4.14) using the mapping  $z \mapsto e^{iw}$ :

$$Y(\omega) = \sum_{m=-\frac{N}{2}}^{\frac{N}{2}-1} H_m \left( \omega - \frac{2\pi m}{N} \right) U \left( \omega - \frac{2\pi m}{N} \right). \quad (4.16)$$

$H_m(z)$  (or  $H_m(w)$ ) is the  $m^{\text{th}}$  harmonic of the HTF structure that defines the coupling between the output at frequency  $w$  (or  $w + \frac{2\pi m}{N}$ ) and the input at frequency  $w - \frac{2\pi m}{N}$  (or  $w$ ).

## 4.5 Identification of HTF of LDTP Systems

### 4.5.1 Identification via Single Cosine Inputs

In this section we show how harmonic transfer functions can be estimated using single cosine inputs and the limitations of this approach. Let the input be a (real) phase shifted cosine signal  $u[n] = \frac{a}{\pi} \cos(\bar{\omega}n + \phi)$ ,  $\bar{\omega} \in [0, \pi)$ . If we use the HTF

CHAPTER 4. IDENTIFICATION OF RHYTHMIC SYSTEMS VIA HTF

structure in (4.16), the response to  $u[n]$  can be computed in frequency domain as

$$Y(\omega) = \sum_{m=-\frac{N}{2}}^{\frac{N}{2}-1} H_m \left( \omega - \frac{2\pi m}{N} \right) a e^{i\phi} \delta \left( \omega - \frac{2\pi m}{N} - \bar{\omega} \right) \\ + \sum_{m=-\frac{N}{2}}^{\frac{N}{2}-1} H_m \left( \omega - \frac{2\pi m}{N} \right) a e^{-i\phi} \delta \left( \omega - \frac{2\pi m}{N} + \bar{\omega} \right)$$

Let us analyze the steady-state frequency response for  $\omega = \bar{\omega} + \frac{2\pi l}{N}$  where  $l \in \{-N/2, \dots, N/2\}$ :

$$Y \left( \bar{\omega} + \frac{2\pi l}{N} \right) = H_l(\bar{\omega}) a e^{i\phi} \\ + \operatorname{sgn}(m^*) H_{l-m^*} \left( \bar{\omega} + \frac{2\pi m^*}{N} \right) a e^{-i\phi}$$

where

$$m^* = \begin{cases} \frac{\bar{\omega}N}{\pi}, & \text{if } \frac{\bar{\omega}N}{\pi} \in \mathbb{Z}^+ \\ 0, & \text{otherwise} \end{cases}$$

If  $m^* \neq 0$  then, there exist two unknowns, thus it is not possible to identify neither  $H_l(\bar{\omega})$  nor  $H_{l-m^*}(\bar{\omega} + \frac{2\pi m^*}{N})$  using a single cosine input. However if  $m^* = 0$  (or equivalently  $\frac{\bar{\omega}N}{\pi} \notin \mathbb{Z}^+$ ), then we can identify  $H_l(\bar{\omega})$  via

$$H_l(\bar{\omega}) = \frac{Y \left( \bar{\omega} + \frac{2\pi l}{N} \right)}{a e^{i\phi}}.$$

## CHAPTER 4. IDENTIFICATION OF RHYTHMIC SYSTEMS VIA HTF

In conclusion, in order to identify the elements of HTF using single cosine inputs (for each frequency), the input frequency must not be an integer multiple of half of the so-called “pumping frequency” ( $\omega_p = \frac{2\pi}{N}$ ), i.e.,  $\frac{\bar{\omega}N}{\pi} \notin \mathbb{Z}^+$ .

Note that it is possible to identify the elements of the HTF at these harmonics by simply exciting the system using two cosine inputs (same frequency, different phase) [89]. However, if we assume the HTFs are smooth and the resolution of the DFT frequencies are high enough, the HTFs at these frequencies can be interpolated in order not to increase the number of experiments.

### 4.5.2 Identification via Sums of Cosine Inputs

In this section our goal is to determine the rules such that elements of the HTF can be estimated uniquely (assuming no noise) from the experiments where the input stimulus is the sum of cosine inputs. Let  $\{\bar{\omega}_1, \dots, \bar{\omega}_K\}$ ,  $\{\phi_1, \dots, \phi_K\}$ , and  $\{\frac{a_1}{\pi}, \dots, \frac{a_K}{\pi}\}$  be the set of input frequencies, phase shifts, and magnitudes respectively. The input signal for the experiment can be constructed as

$$u[n] = \sum_{k=1}^K \frac{a_k}{\pi} \cos(\bar{\omega}_k n + \phi_k). \quad (4.17)$$

## CHAPTER 4. IDENTIFICATION OF RHYTHMIC SYSTEMS VIA HTF

Since single sine experiment is a special case of a sum of sine experiment, the obvious first rule for the identification is

$$\frac{\bar{\omega}_k N}{\pi} \notin \mathbb{Z}^+ \quad \forall k \quad (4.18)$$

For the sake of clarity let's assume that  $K = 2$ . Then frequency response of the system to the input (4.17) at the frequency  $\omega = \bar{\omega}_1$  takes the form

$$\begin{aligned} Y(\bar{\omega}_1) &= H_0(\bar{\omega}_1) a_1 e_1^{i\phi} \\ &+ \operatorname{sgn}(m_1^*) H_{m_1^*} \left( \bar{\omega}_1 - \frac{2\pi m_1^*}{N} \right) a_2 e^{i\phi_2} \\ &+ \operatorname{sgn}(m_2^*) H_{m_2^*} \left( \bar{\omega}_1 - \frac{2\pi m_2^*}{N} \right) a_2 e^{-i\phi_2} \end{aligned}$$

where

$$\begin{aligned} m_1^* &= \begin{cases} \frac{(\bar{\omega}_1 - \bar{\omega}_2)N}{2\pi}, & \text{if } \frac{|\bar{\omega}_1 - \bar{\omega}_2|N}{2\pi} \in \mathbb{Z}^+ \\ 0, & \text{otherwise} \end{cases} \\ m_2^* &= \begin{cases} \frac{(\bar{\omega}_1 + \bar{\omega}_2)N}{2\pi}, & \text{if } \frac{(\bar{\omega}_1 + \bar{\omega}_2)N}{2\pi} \in \mathbb{Z}^+ \\ 0, & \text{otherwise} \end{cases} \end{aligned}$$

Similar structure is obtained if we extend to arbitrary  $K$  and observe the response at  $\omega = \bar{\omega}_k + \frac{2\pi l}{N}$ . From this result, we observe that in order to identify the elements of the HTF uniquely, in addition to the constraint on each individual frequency in

## CHAPTER 4. IDENTIFICATION OF RHYTHMIC SYSTEMS VIA HTF

(4.18), we also require that the difference and the sum of any two frequencies in the input stimulus must not be an integer multiple of the pumping frequency. Under these rules elements of the HTF structure can be estimated using

$$H_l(\bar{\omega}_k) = \frac{Y(\bar{\omega}_k + \frac{2\pi l}{N})}{a_k e^{i\phi_k}}.$$

Under these rules our system identification procedure using sum-of-sine inputs is as follows:

- Define the frequency band of interest,  $\bar{\omega}_k \in (0, \omega_{max}]$  and compute the resolution,  $\omega_{res}$ , of the DFT frequencies based on the length of the input-output data.
- Construct a global set of frequencies,  $\Omega = \{\omega_{res}, 2\omega_{res}, 3\omega_{res}, \dots, \omega_{max}\}$ .
- Remove the frequencies that are the integer multiples of half of the pumping frequency, i.e.  $\bar{\Omega} = \Omega - \{\frac{\pi}{N}, \frac{2\pi}{N}, \frac{3\pi}{N}, \dots\}$ .
- Partition  $\Omega$  in to  $S$  sub sets,  $\bar{\Omega} = \Omega_1 \cup \Omega_2 \dots \cup \Omega_S$ , such that for each  $\Omega_s$  following condition is satisfied:

$$\frac{|\bar{\omega}_i - \bar{\omega}_j|N}{2\pi} \notin \mathbb{Z}^+ \ \& \ \frac{(\bar{\omega}_i + \bar{\omega}_j)N}{2\pi} \notin \mathbb{Z}^+$$

$$\forall \bar{\omega}_i, \bar{\omega}_j \in \Omega_s$$

- For each subset construct an input stimulus

$$u_s[n] = \sum_{\bar{\omega}_k \in \Omega_s} \frac{a_k}{\pi} \cos(\bar{\omega}_k + \phi_k),$$

and perform the experiment to compute the elements of HTF.

## 4.6 Results and Discussion

### 4.6.1 Example Model System

We apply our system identification framework to the vertical hopper model illustrated in Fig. 4.2. We adopted the model from [25] and added an exogenous input  $u$  acting on the upper body mass  $M$  to be used for system identification. The “clock-driven” hopper alternates between flight ( $\alpha = 0$ ) and stance ( $\alpha = 1$ ) charts during

hopping. Flight and stance dynamics of the hopper are

$$\text{Flight : } \alpha = 0, \quad q_0 = [\phi, y_M, \dot{y}_M, y_m, \dot{y}_m]^T \in V_0$$

$$\dot{\phi} = 2\pi, \quad f = a \sin(\phi),$$

$$\dot{y}_M = \frac{-k(y_M + y_m - l_0) + f + u}{M} - g$$

$$\dot{y}_m = \frac{k(y_M + y_m - l_0) - c\dot{y}_m - f}{m} - g$$

$$\text{Stance : } \alpha = 1, \quad q_1 = [\phi, y_M, \dot{y}_M]^T \in V_1$$

$$\dot{\phi} = 2\pi, \quad f = a \sin(\phi),$$

$$\dot{y}_M = \frac{-k(y_M + y_m - l_0) + f + u}{M} - g$$

The touchdown event defines the transition from flight to stance chart. The zero crossing of the threshold function,  $h_o(q_0) = y_m$ , triggers the transition and the states of the new chart is defined by the transformation  $q_0 \mapsto T_0(q_0)$  where  $T_0(q_0) = [I_{3 \times 3} \ 0_{3 \times 2}] q_0$ . The liftoff event defines the transition from stance to flight, which is triggered by the zero crossing of the threshold function  $h_1(q_1) = k(l_0 - y_M) + f + mg$ . The initial state of the new flight chart is determined by the transformation  $q_1 \mapsto T_1(q_1)$  where  $T_1(q_1) = [I_{3 \times 3} \ 0_{3 \times 2}]^T q_1$ . We simulated the hybrid hopper model in MATLAB (Mathworks, Inc.), using a custom hybrid dynamical simulation toolkit [4,5] with the sample parameters  $([m \ M \ k \ bl_0 \ a \ g]^T = [1 \ 210 \ 5 \ 2 \ 20 \ 2])$  used in [25]. We verified with our simulation toolkit that this set of parameters (when external input  $u = 0$ ) produces a stable limit cycle. The non-zero eigenvalues of the Poincaré maps of the

system are  $\lambda_{1,2} = 0.25 \pm 0.7i$ , computed via the numerical Jacobian of the return map.

## 4.6.2 Phase Coordinates and Set of Poincaré Sections

As detailed in Sec. 4.3 our system identification method relies on mappings between selected discrete phase coordinates (i.e. set of Poincaré Sections). We expect that the structure of HTF depends on the selected phase coordinates.

In this chapter, we utilized two “causal” phase definitions to select Poincaré sections. Existence of exogenous input and its dependence on phase coordinates makes the straight forward implementation of non-causal methods [128] impossible. The hybrid system we are analyzing is an asymptotically stable clock-driven model, thus one natural way of selecting Poincaré sections is using the isochrons [73] which are directly given by the phase of the clock. We select  $N$  equally spaced Poincaré sections within  $\phi \in [0, 2\pi)$ . The phase of the  $i^{th}$  Poincaré section corresponds to  $\phi_i = \frac{2\pi}{N}i$ . As expected this definition of phase results in discretizing the time samples with a fixed time step  $\Delta t = 1/N$  (since the pumping frequency is 1Hz). In a class of legged robotic platforms [65, 135, 136], there exist an central architecture (CPG) that generates an open-loop time periodic pattern and all other sub-level controllers are synchronized to this clock. For these kind platforms phase of the center clock can be used to define

isochrons and our HTF based identification method can be easily applied.

However, the majority of rhythmic hybrid system models are not driven by an open-loop clock thus there is no straightforward way of accessing the isochrons, especially using a causal method. The main advantage of our method is that it works with any set of well defined Poincaré sections. In addition to isochrons, we use a definition similar to the kinematic phase used in [127]. Using the states  $y_M, \dot{y}_M$ , we define a phase variable:

$$r_p = \frac{y_M - o_p}{s_p}, \quad r_v = \frac{\dot{y}_M - o_v}{s_v}$$

$$\hat{\phi} = \phi r_p + i r_v, \quad \hat{\phi} \in S^1$$

where  $(o_p, o_v)$  and  $(s_p, s_v)$  simply shifts the origin and scales the coordinates, respectively. Based on this definition of phase, we select equally spaced  $N$  Poincaré sections within  $\hat{\phi} \in [0, 2\pi)$ . In our simulations, for both isochrons and kinematic phase, we choose  $N = 32$  and align the  $\phi = 0$  and  $\hat{\phi} = 0$  events on the limit cycle.

### 4.6.3 Simulation Results

#### 4.6.3.1 Non-parametric Harmonic Transfer Functions

In this section we present the estimated non-parametric harmonic transfer functions based on three different phase coordinates: isochrons and kinematic phase I

## CHAPTER 4. IDENTIFICATION OF RHYTHMIC SYSTEMS VIA HTF

with  $(o_p, o_v, s_p, s_v) = (1.9, 0, 0.3, 1.9)$ , and kinematic phase II with  $(o_p, o_v, s_p, s_v) = (1.95, 0, 0.3, 1.9)$ .

We identify the HTF blocks from  $u[n]$  to  $y[n]$ , where  $y$  is either taken as the deviation of the height from the fixed point, namely  $\delta y_M$ , or the deviation of the vertical velocity from the fixed point,  $\delta \dot{y}_M$ . In order to compute the limit-cycles, we run the hybrid simulation script in the absence of any external input for 60s and use the last cycle of this simulation as the baseline for the limit cycle. We use the method proposed in 4.5.2 and excite the system with inputs that are sums of cosine signals. The length of the each sums of cosines experiment is 84 cycles, however we only use the last 64 cycles in order not to capture any transient effects on the frequency response data. 64 cycles of data with  $N = 32$  provides a frequency resolution of  $f_{\text{res}} = \frac{1}{32}$  (or  $\omega_{\text{res}} = \frac{\pi}{16} \text{rad/s}$ ).  $f$  is the normalized frequency with units of cycles per fundamental period. We compute the HTFs in the frequency band  $f \in (0, 10)$ . As explained in Sec.4.5.1 we remove the frequencies that are the prime multiple of the  $f = 0.5$  (or  $\omega = \frac{\pi}{32}$ ) and we were left with 620 frequencies for which we need to identify the HTF components. We divide these 620 frequencies into 80 subsets randomly following the rules derived in Sec. 4.5.2. For each subset we construct an input signal, perform the experiment, and compute the HTF components associated with those frequencies.

Fig. 4.3 illustrates the magnitude plots of the empirical HTFs. For all phase coordinates we found that the magnitude of the components,  $H_i$ , for  $|i| \geq 2$  were

negligible compared to  $|H_0(z)|$ ,  $|H_1(z)|$  &  $|H_{-1}(z)|$  thus we only illustrate those three responses. This is somewhat surprising, because even for a hybrid system for which the dimension of charts are not constant three harmonics can accurately describe the dynamics around the limit cycle.

### 4.6.3.2 Phase Coordinates Affect Zeros, not Poles

If we compare the HTFs from different phase coordinates, we can see that the structure of the HTF is indeed affected by the choice of Poincaré sections. In the context of  $H_0(z)$  the gain is doubled if we use isochrons instead of the kinematic phase definition (note the vertical shift in Fig. 4.3 in the blue curve). The phase coordinates affects the harmonics  $H_1(z)$  and  $H_{-1}(z)$  structurally (red and dashed red curves). However, it seems that the “resonant” frequencies (peaks of the magnitude plots) are located at approximately same locations for all phase coordinates. We suspect that this is because choice of Poincaré sections do not move the pole dynamics of the HTF but instead changes the zeros.

### 4.6.3.3 Estimation of Poincaré Return Map Eigenvalues

In this section, we present an approximate parametric estimation approach for the non-zero eigenvalues of the Poincaré return map through parametric identification of the fundamental transfer function, i.e.  $H_0(z)$ . If we observe the bode plots of  $H_0(z)$  illustrated in Fig. 4.4, we see that all of them approximately look like transfer

## CHAPTER 4. IDENTIFICATION OF RHYTHMIC SYSTEMS VIA HTF

functions with two poles, so we assumed a second-order transfer function with one zero and two poles. From the results we see that the parametric transfer functions fit the frequency response data very well except some higher order “bumps” around  $f = 2\text{Hz}$ , i.e. twice the system pumping frequency. Since we have a parametric estimation of  $H_0(z)$  we can now recover the eigenvalues of the Poincaré return map. Let  $p$  be a pole of the HTF, then the eigenvalues of the Poincaré return map can be computed simply  $\lambda = p^N$ . All of the six parametric transfer functions were correctly estimated the true eigenvalues of the system  $\lambda_{1,2} = 0.25 \pm 0.70i$  (with numerical errors at the third significant digit).

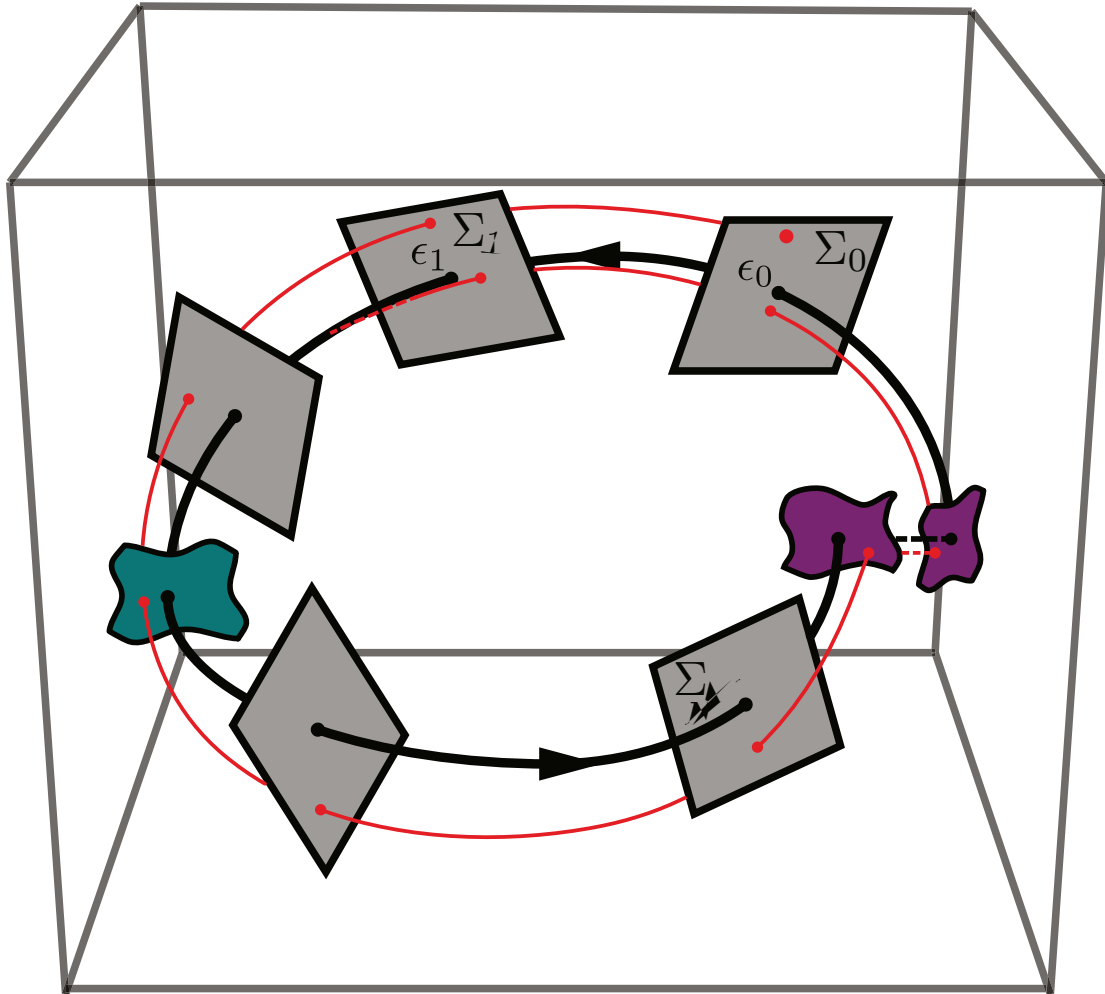


Figure 4.1: **Illustration of a stable rhythmic hybrid dynamical system with two charts, i.e.  $\mathcal{I} = \{0, 1\}$ .** For simplicity, each chart has the same dimension, and is a subset of  $\mathbb{R}^3$ . The limit cycle of the system (black) is discontinuous. The two-dimensional surface (green) illustrates a hybrid transition (patch) boundary in which the transition is continuous (no jump in continuous variables of the state space) but not necessarily differentiable. The pair of surfaces (purple) connected by dashed lines illustrate a hybrid transition boundary in which the transition is discontinuous. The two-dimensional cross-sections (grey) illustrate the  $N$  Poincaré sections chosen by the experimenter. (These can be the hybrid boundaries, but in this example are chosen not to be.) The red curve represents a sample trajectory starting from an initial condition located at  $\Sigma_0$ . As illustrated in the figure, in the absence of external inputs trajectory converges to the limit cycle.

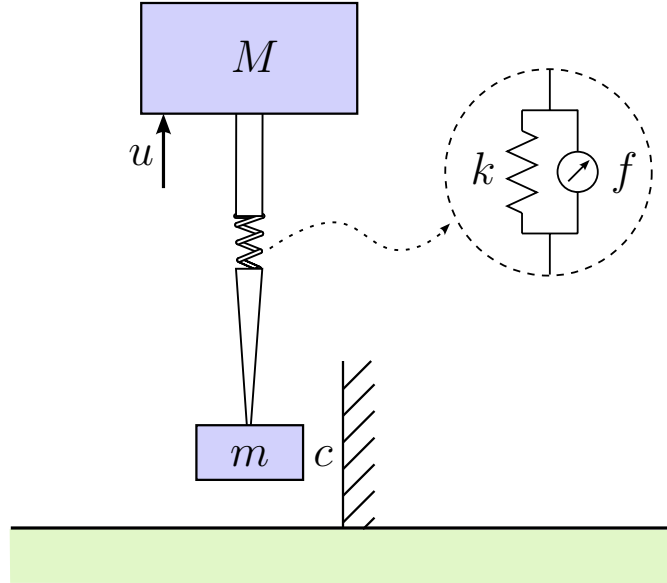


Figure 4.2: Schematic of the hopper model

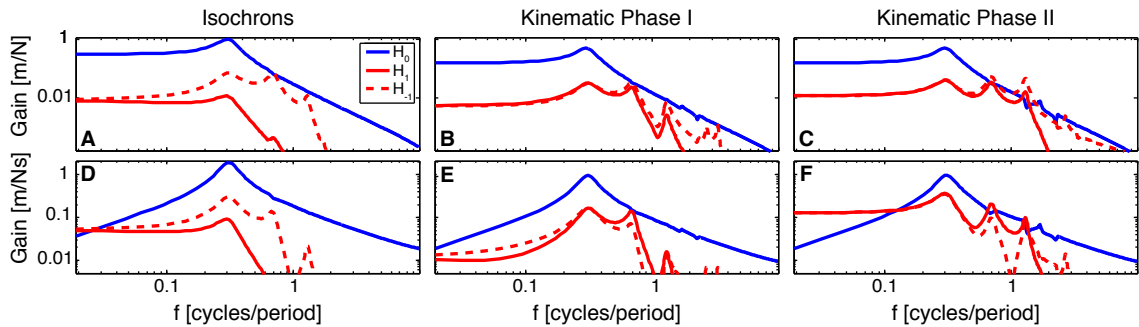


Figure 4.3: **Non-parametric estimates of  $|H_0(z)|$ ,  $|H_1(z)|$  and  $|H_{-1}(z)|$ .** Magnitude plots in the top row (A, B, and C) represents the HTFs between the input and  $\delta y_M$ , where as bottom row (D, E, and F) belongs to the HTFs between the input and  $\delta \dot{y}_M$ . First (A and D), second (B and E) and third column (C and F) represents the HTFs where the phase coordinates are selected using isochrons, kinematic phase I, and kinematic phase II respectively.

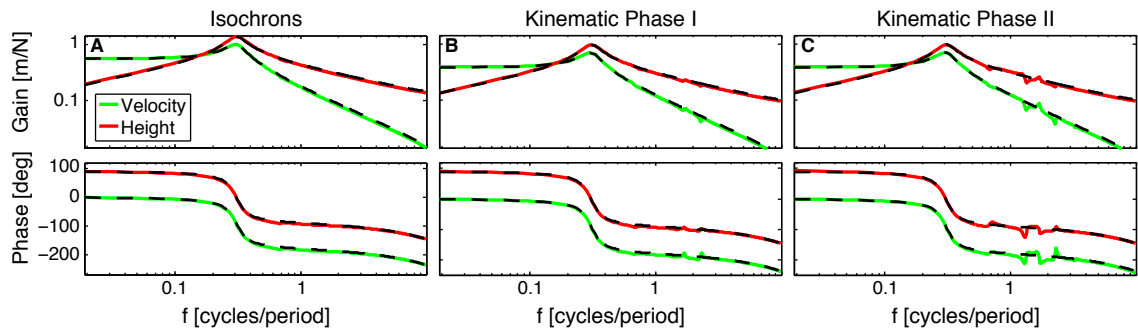


Figure 4.4: **Non-parametric and parametric estimates of  $|H_0(z)|_s$ .** Figures in the top row indicates the magnitude plots, whereas the ones in the bottom row indicates the phase plots. Green and red curves represents the magnitude and phase plots for the HTFs from input to  $\delta y_M$  and from input to  $\delta \dot{y}_M$  respectively. Black curves the magnitude and phase plots of the estimated parametric transfer functions. First (A), second (B), and third column (C) represents the HTFs where the phase coordinates are selected using isochrons, kinematic phase I, and kinematic phase II respectively.

# Chapter 5

## Conclusion

In this dissertation, we described three important baby steps towards the ultimate goal of discovering the rules by which the human nervous system controls rhythmic behaviors such as circadian cycles, heartbeats, juggling, and locomotion. Specifically we investigated three key features—variability, symmetry, and dynamics—in human rhythmic motor control by using two different experimental paradigms, i.e. paddle juggling (Chapter 2) and walking (Chapter 3). In order to achieve our goals, we adopted and developed new statistical and theoretical tools, such as mean-first-passage time in Section 2.2.6, extended cross validation in Section 3.3.1, and discrete time harmonic transfer functions in Section 4.4.

In Chapter 2, we sought answers to this question: how does haptic (“touch”) feedback during hybrid transitions, such as heel-strike event during walking, enhance rhythmic behavior? To determine the effect of haptic cues on rhythmic motor perfor-

## CHAPTER 5. CONCLUSION

mance, we investigated a simplified “virtual paddle juggling” behavior. We showed that haptic feedback, in the form of a force impulse to the hand at the moment of ball–paddle impact, categorically improves performance over visual feedback alone, not by regulating the rate of convergence to steady state (e.g. via higher gain feedback control or reshaping the nominal hand motion), but rather by reducing cycle-to-cycle variability of the stochastic juggling behavior. Based on this result, we speculated that the timing and state information provided by haptic feedback decreases the nervous system’s uncertainty (i.e. variability) of the ball’s state to enable more “accurate” control, but that the feedback and feedforward controllers are unaltered.

In Chapter 3, we showed that neglecting an evident characteristic of a system can be more than a modeling convenience, it can also produce a better model. We focused our attention on bilateral dynamic symmetry (or asymmetry) in human walking. We proposed a statistical framework which is a simple extension of the classical Monte Carlo cross-validation method. We applied this method to data obtained from eight different healthy individuals walking at three different speeds. We observed that the asymmetry in walking dynamics is statistically significant. Despite the existence of significant asymmetries, we showed that by ignoring these asymmetries and modeling walking dynamics as symmetric produces models that have more predictive power and are more precise than the models in which asymmetry is enforced. Indeed, we showed it is not only “OK” to neglect asymmetry; in this cases, it is better.

In Chapter 4, we introduced a new method for the system identification of rhyth-

## CHAPTER 5. CONCLUSION

mic systems. Our motivation was the fact that few tools exist for identifying the dynamics of rhythmic hybrid dynamical systems from input–output data, even though it is critical to many applications in robotics and biology. We proposed a new formulation that addresses the system identification problem of rhythmic hybrid dynamical systems in the frequency domain using discrete-time harmonic transfer functions. In order to show the feasibility and important features of our approach, we tested our method on a simulated hybrid hopper model.

# Appendix A

## Appendix for Chapter 2

### A.1 Virtual Versus Physical Paddle Juggling

Our preference toward virtual juggling [47,130,131,162,163] over physical juggling [137,152] stems from our ability to control the physical dynamics that the human interacts with during control. Indeed, these dynamics play a critical role in decoding and understanding neural circuits that control motion [34,41,83,158].

One of the main limitations of the physical juggling used in [137,152] was that it required two experimental systems, one that displays haptic feedback, and a distinct system that did not. Specifically, with haptic feedback, the subject controlled the motion of a physical paddle whose surface remained horizontal via a mechani-

## APPENDIX A. APPENDIX FOR CHAPTER 2

cal linkage, and the paddle hit a table tennis ball that was fixed to a hinged boom. Because the linkage was mechanical, impact forces were transmitted nearly instantaneously to the user’s hand. To create the no-haptic-feedback condition, by contrast, a telerobotic system mechanically decoupled the user’s hand from the paddle. The user’s hand motions provided a reference trajectory that was tracked by a robotically controlled paddle. In this case, haptic feedback regarding the ball–paddle collision was not transmitted back to the user’s hand. This setup introduced a confound: the setup without haptic feedback included an entire tele-robotic system with its own dynamics (including potential filtering and phase lags), which likely affected results. Indeed we show below (in the specific context of offline filtering), that subtle differences to filtering dynamics can dramatically alter estimates of impact acceleration. Therefore, in this thesis we re-examine the role of haptic feedback in a context where the two experimental conditions (with versus without haptic feedback) are directly related.

Estimating the time of the ball–paddle collision, and the acceleration of the paddle at that instant, is coupled in the physical apparatus. When the ball bounces, it imparts significant (negative) momentum to paddle. The time at which the ball reaches a local minimum is used to estimate impact time [137,152]. Because the ball’s rapid positive acceleration and reversal is concomitant with the negative momentum changes to the paddle, the point in time corresponding to a local minimum in the ball height also corresponds to a moment when the paddle has already necessarily accel-

erated downward. The detection of impact time and the estimation of acceleration at impact are fundamentally coupled in this physical juggling system in a way that leads to a negative bias in the estimated impact accelerations for the haptic condition, a bias consistent with previous findings [152].

The coupling of detecting the moment of ball–paddle impact and estimating acceleration at impact can be eliminated in virtual juggling since the computer can detect the (virtual) impact, and only then impart the force to the haptic paddle. This allows us to (causally) determine impact acceleration without being potentially biased by our method for detecting impact time based on physical accelerations of the paddle and/or ball.

## A.2 Causal vs Non-causal Impact Acceleration Estimation

As described in Methods, in order to estimate the acceleration of the paddle at the time of impact we follow a causal method and only the kinematic information before the time of impact is used. As an alternative to our filtering method, one might have used simple non-causal filters [131, 137, 152, 162, 163] which have the benefit of introducing zero phase lag and thus are quite commonly used in data analysis.

However, the force that we applied to the paddle during the impact instant generated a small but significant negative acceleration at the hand, and non-causal filters

## APPENDIX A. APPENDIX FOR CHAPTER 2

therefore produced consistent biases to acceleration estimates at the impact instant. For smoothly changing data, non-causal filters typically provide accurate estimates so we developed a causal filter that, for the no-haptic feedback case (without force impulse generation), our scheme provided similar results to a well-tuned causal filter. Fig. A.1 illustrates our comparison of causal and non-causal mean impact acceleration estimates of each individual and for both haptic conditions. For the data without haptic feedback both estimation methods agree showing no statistically significant difference ( $p > 0.3$  Paired t-test). However, in the haptic case the non-causal estimation method resulted in significant negative bias compared to causal estimation method ( $p < 1e - 6$ , Paired one sided t-test). These results show that non-causal impact acceleration estimation methods can generate misleading negative acceleration.

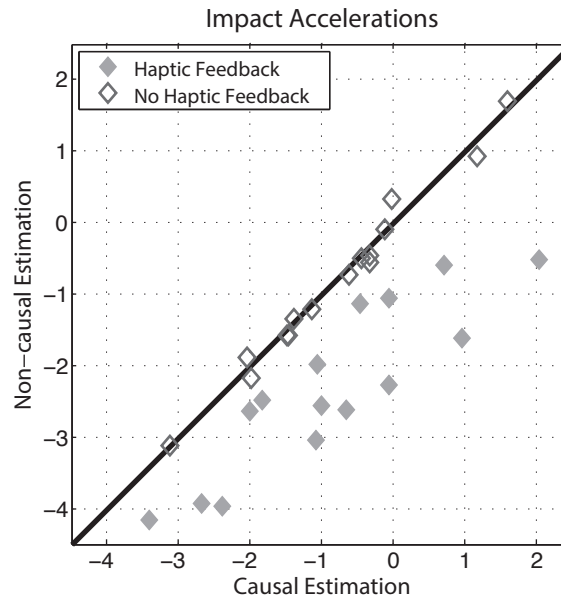


Figure A.1: **Non-causal filtering biases the estimate of impact acceleration with haptic feedback.** Markers indicate estimated impact accelerations (abscissa and ordinate belong to causal and non-causal estimates, respectively). Hollow dark markers and solid light markers correspond to scenarios without and with haptic feedback, respectively. The 45° solid black line would indicate ideal agreement between causal and non-causal estimates.

# Appendix B

## Appendix for Chapter 3

### B.1 Verification of Results by Extended Leave-One-Out (LOO) Bootstrap

Model selection methods based on bootstrap sampling [53, 54, 146] offer a powerful set of alternatives to cross validation. In order to examine these as well as validate our scientific results, we performed a parallel analysis using a bootstrap sampling approach. Similar to our approach in applying cross-validation methods (Sec. 3.3.1), we extended a bootstrap method, specifically LOO bootstrap [52]. We chose LOO bootstrap because it has a critical feature—the ability to isolate a validation sample from the test sample—that is necessary to test our statistical question at hand, specifically to test mirrored and combined data against normal data.

## Classical Leave-one-out Bootstrap

Consider  $n$  pairs of input–output data,  $(x_i, y_i)$ , where  $i \in \mathcal{I} = \{1, 2, 3, \dots, n\}$ . Draw  $B$  bootstrap samples  $\mathcal{I}_b^* = \{1_b^*, 2_b^*, 3_b^*, \dots, n_b^*\}$ ,  $b = \{1, 2, 3, \dots, B\}$ , where  $i_b^*$ s are randomly sampled from  $\mathcal{I}$  with replacement. For each bootstrap sample,  $\mathcal{I}_b^*$ , construct the bootstrap analogs of  $X_b^*$  and  $Y_b^*$  matrices as follows:

$$\begin{aligned} X_b^* &= [x_{1_b^*}, \dots, x_{n_b^*}]^T, \\ Y_b^* &= [y_{1_b^*}, \dots, y_{n_b^*}]^T, \end{aligned} \tag{B.1}$$

and using these matrices find the bootstrap analog of the least squares solution in (3.16),  $A_b^* = (X_b^{* \dagger} Y_b^*)^T$ . Then leave-one-out bootstrap prediction error can be computed as

$$E_{\text{LB}} = \frac{1}{n} \sum_{i=1}^n \frac{1}{|\mathcal{B}_{-i}|} \sum_{b \in \mathcal{B}_{-i}} \frac{\|y_i - A_b^* x_i\|^2}{\|y_i\|^2}, \tag{B.2}$$

where  $\mathcal{B}_{-i}$  is set of indices of bootstrap samples that does not contain observation  $i$  and  $|\mathcal{B}_{-i}|$  is the cardinality of this set.

## Extending LOO Bootstrap

Using the same approach that we performed for the extension of cross-validation, we can extend classical LOO bootstrap. In classical LOO bootstrap, one bootstrap error is computed using Eq. (B.2), whereas in our method we compute three types of bootstrap errors. Each application of extended LOO bootstrap requires a normal set,

APPENDIX B. APPENDIX FOR CHAPTER 3

$\mathcal{N}$ , and an equal-sized mirrored set,  $\mathcal{M}$ . The normal and mirrored sets *each* include  $n$  mutually exclusive input–output pairs, denoted by  $(x_i, y_i) \in \mathcal{N}$  and  $(\hat{x}_i, \hat{y}_i) \in \mathcal{M}$ , respectively where  $i \in \mathcal{I} = \{1, 2, \dots, n\}$ . As for classical LOO bootstrap, we start with drawing  $B$  bootstrap samples  $\mathcal{I}_b^* = \{1_b^*, 2_b^*, 3_b^*, \dots, n_b^*\}$ ,  $b = \{1, 2, 3, \dots, B\}$ .

Again similar to extended CV, the validation samples for computing all three bootstrap errors are selected from  $\mathcal{N}$ .

**Normal LOO Bootstrap (NLB)** is the same as LOO bootstrap, in that bootstrap analogs of input–output matrices in (B.1) are constructed from  $\mathcal{N}$  using the bootstrap index set samples,  $\mathcal{I}_b^*$ . Thus, for each bootstrap sample the bootstrap analog of the model matrix,  $A_{b\text{NLB}}^*$ , is computed as

$$\begin{aligned} (x_{i_b^*}, y_{i_b^*}) &\in \mathcal{N}, \\ X_b^* &= [x_{1_b^*}, \dots, x_{n_b^*}]^T, \\ Y_b^* &= [y_{1_b^*}, \dots, y_{n_b^*}]^T, \\ A_{b\text{NLB}}^* &= (X_b^{*\dagger} Y_b^*)^T. \end{aligned} \tag{B.3}$$

Then NLB prediction error is computed as

$$E_{\text{NLB}} = \frac{1}{n} \sum_{i=1}^n \frac{1}{|\mathcal{B}_{-i}|} \sum_{b \in \mathcal{B}_{-i}} \frac{\|y_i - A_{b\text{NLB}}^* x_i\|^2}{\|y_i\|^2}. \tag{B.4}$$

**Mirrored LOO Bootstrap (MLB)** constructs the bootstrap analogs of the input–output matrices in (B.1) from the mirrored dataset  $\mathcal{M}$ , using the same boot-

APPENDIX B. APPENDIX FOR CHAPTER 3

strapped index set samples,  $\mathcal{I}_b^*$ . Thus, for each bootstrap sample the bootstrap analog of the model matrix,  $A_{b\text{MLB}}^*$  is computed as

$$\begin{aligned}
 (\hat{x}_{i_b^*}, \hat{y}_{i_b^*}) &\in \mathcal{M} \\
 \hat{X}_b^* &= [\hat{x}_{1_b^*}, \dots, \hat{x}_{n_b^*}]^T \\
 \hat{Y}_b^* &= [\hat{y}_{1_b^*}, \dots, \hat{y}_{n_b^*}]^T \\
 A_{b\text{MLB}}^* &= (\hat{X}_b^{*\dagger} \hat{Y}_b^*)^T.
 \end{aligned} \tag{B.5}$$

Then MLB prediction error is computed as

$$E_{\text{MLB}} = \frac{1}{n} \sum_{i=1}^n \frac{1}{|\mathcal{B}_{-i}|} \sum_{b \in \mathcal{B}_{-i}} \frac{\|y_i - A_{b\text{MLB}}^* x_i\|^2}{\|y_i\|^2} \tag{B.6}$$

**Combined LOO Bootstrap (CLB)** constructs the bootstrap analogs of the matrices in (B.1) from both the normal  $\mathcal{N}$  and mirrored  $\mathcal{M}$  data sets, using the same bootstrapped index set samples,  $\mathcal{I}_b^*$ . Thus, for each bootstrap sample the bootstrap analog of the model matrix,  $A_{b\text{CLB}}^*$ , is computed as

$$A_{b\text{CLB}}^* = \left( \begin{pmatrix} \begin{bmatrix} X_b^* \\ \hat{X}_b^* \end{bmatrix} \dagger \begin{bmatrix} Y_b^* \\ \hat{Y}_b^* \end{bmatrix} \end{pmatrix} \right)^T. \tag{B.7}$$

Then CLB prediction error is computed as

$$E_{\text{CLB}} = \frac{1}{n} \sum_{i=1}^n \frac{1}{|\mathcal{B}_{-i}|} \sum_{b \in \mathcal{B}_{-i}} \frac{\|y_i - A_{b\text{CLB}}^* x_i\|^2}{\|y_i\|^2}. \quad (\text{B.8})$$

## B.2 Results for LOO Bootstrap

### B.2.1 Symmetric vs Asymmetric Modeling

In Sec. 3.4.1, we tested the statistical consequences of symmetric and asymmetric modeling assumptions in the dynamics of human walking, by comparing NCV, MCV, and CCV errors. Likewise, our parallel analysis compared NLB, MLB, and CLB errors.

Fig. B.1(a) compares MLB and CLB errors to NLB error for the step-to-step data. MLB errors are (statistically) significantly higher than NLB errors at all speeds ( $p_{1.5m/s} = 0.004$ ,  $p_{1m/s} = 0.004$  and  $p_{0.5m/s} = 0.004$ ; one-sided Wilcoxon rank-sign test). This shows that the bootstrap-based method also detects a dynamical asymmetry between  $L \mapsto R$  and  $R \mapsto L$ . On the other hand, the comparison of CLB and NLB errors illuminates a different perspective (Fig. B.1(a)). Surprisingly, the average CLB error was (statistically) significantly lower than the average NLB error at all speeds ( $p_{1.5m/s} = 0.02$ ,  $p_{1m/s} = 0.02$ , and  $p_{0m/s} = 0.004$ ; one-sided Wilcoxon rank-sign test), which indicates an even stronger gain by neglecting symmetry than

what we observed with CV errors (Fig. 3.5(a)).

Fig. B.1(b) compares the MLB and CLB errors to NLB error for stride-to-stride data. MLB errors were higher (on average) than NLB errors for all speeds and these differences were statistically significant ( $p_{1.5m/s} = 0.004$ ,  $p_{1m/s} = 0.004$  and  $p_{0.5m/s} = 0.004$ ; paired one-sided Wilcoxon rank-sign test). This result verifies that our data is dynamically asymmetric between  $L \mapsto L$  and  $R \mapsto R$ . In agreement with the CV case (Fig. 3.5(b)), the comparison of NLB and CLB errors in stride-to-stride data shows that CLB errors were statistically significantly lower than the NLB errors at all three speeds ( $p_{1.5m/s} = 0.004$ ,  $p_{1m/s} = 0.004$  and  $p_{0.5m/s} = 0.004$ ; paired one-sided Wilcoxon rank-sign test).

To summarize, even though there were distinguishable asymmetries in our data, we always gain (for all speeds and both step-to-step and stride-to-stride data) statistically significant predictive power by assuming symmetry in modeling human walking. These results further strengthen our claim that neglecting dynamical asymmetry (an evident and also statistically significant feature) produces stronger models in terms of predictive power.

## Model Uncertainty

Here, we computed the the model uncertainty in (3.21) using the bootstrap samples for both symmetric and asymmetric modeling approaches. The qualitative results are similar to those presented in Sec. 3.4.1.3; for fitting a single return map, there was

APPENDIX B. APPENDIX FOR CHAPTER 3

a substantial reduction in model uncertainty for both the step-to-step and stride-to-stride data. On the other hand, quantitative results based on bootstrap samples are very close to the ones obtained with Monte-Carlo samples which are reported in Figure. 3.6. Model uncertainty results obtained from both CV samples and bootstrap samples are reported in Table B.1. All improvements were statistically significant ( $p = 0.0039$ , one-sided Wilcoxon signed-rank test).

Table B.1: Percentage decrease of model uncertainty when using symmetric modeling (and therefore doubling the data set).

	CV Samples		Bootstrap Samples	
	Step Maps	Stride Maps	Step Maps	Stride Maps
1.5 m/s	56%	61%	51%	57%
1.0 m/s	54%	58%	53%	58%
0.5 m/s	72%	74%	72%	75%

### B.2.2 Step Return Maps vs. Stride Return Maps

In order to measure the loss of signal-to-noise ratio based on the extended LOO Bootstrap method, we analyzed the bootstrap errors by assuming symmetry and fitting return maps to both step and stride data. Specifically we compared LOO bootstrap errors of both step and stride data in our method. The qualitative results from both CV based and LOO bootstrap methods match. There is dramatic signal-to-noise ratio loss with stride-to-stride return maps. Moreover, step-to-step return maps have more predictive power in both the CV setting and bootstrap setting.

## APPENDIX B. APPENDIX FOR CHAPTER 3

Quantitative results are summarized in Table B.2 for both settings.

Table B.2: Percentage increase in prediction error when using stride maps instead of step maps.

	CV	LOO Boot.
1.5 m/s	79%	64%
1.0 m/s	87%	64%
0.5 m/s	31%	24%

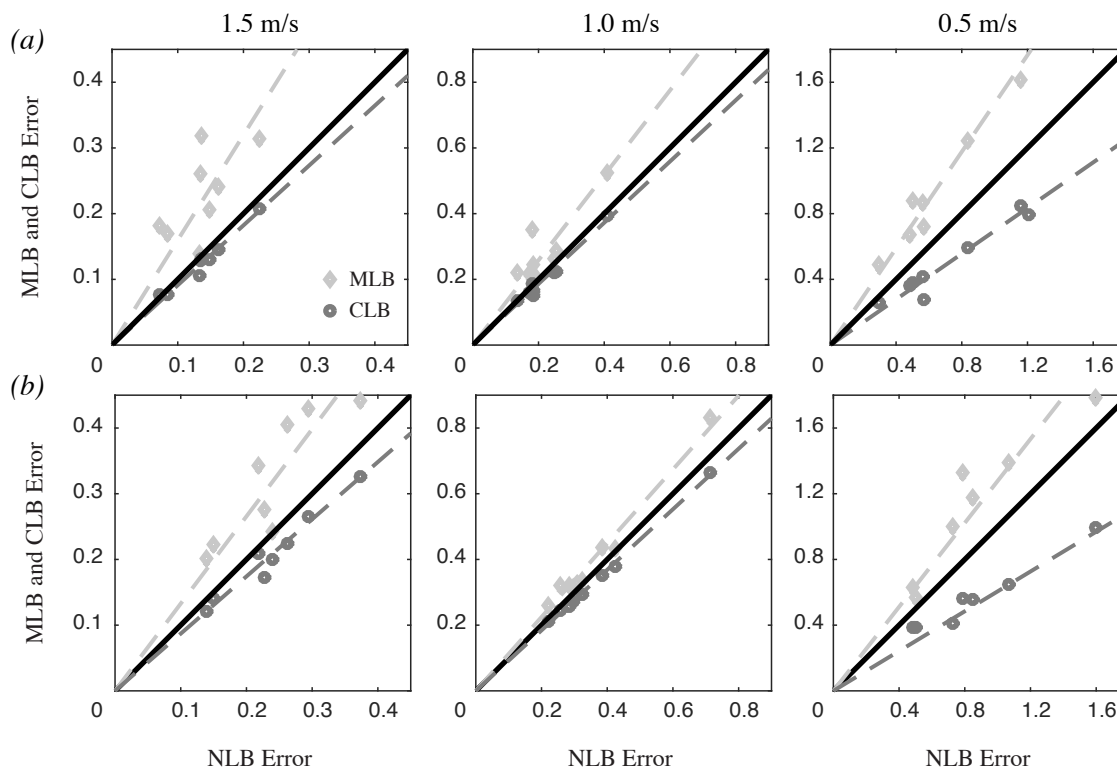


Figure B.1: **We reach the same conclusion if compare bootstrap based results, illustrated in this figure, and cross-validation-based results, illustrated in Fig 3.5.** Walking dynamics is statistically asymmetric, but neglecting this by training a model on the combined data can nevertheless improve statistical performance. (a) Step-to-step maps. At all speeds, the mean mirrored LOO bootstrap errors (light grey diamonds) were significantly worse than for normal cross validation, indicating that steps were indeed asymmetric. Despite this left-right asymmetry, the mean combined LOO bootstrap errors are significantly *lower* at all speeds. The slopes of the fitted lines (dashed) determine the relative increase ( $m > 1$ ) or decrease ( $m < 1$ ) in LOO Bootstrap error relative to the Normal LOO Bootstrap error. (b) Stride-to-stride maps. By the same statistical measure, strides were also asymmetric at all speeds, but less substantially so. Moreover, the mean CLB error was lower than mean NLB error at all speeds.

# Bibliography

- [1] P. Allard, R. Lachance, R. Aissaoui, and M. Duhaime. Simultaneous bilateral 3-d able-bodied gait. *Human Movement Science*, 15(3):327–346, 1996.
- [2] R. Altendorfer, D. E. Koditschek, and P. Holmes. Stability analysis of legged locomotion models by symmetry-factored return maps. *Int J Robot Res*, 23(10-11):979–999, 2004.
- [3] A. D. Ames, R. D. Gregg, E. D. Wendel, and S. Sastry. On the geometric reduction of controlled three-dimensional bipedal robotic walkers. In *Lagrangian and Hamiltonian Methods for Nonlinear Control 2006*, pages 183–196. Springer, 2007.
- [4] M. Ankarali and U. Saranli. Control of underactuated planar pronking through an embedded spring-mass hopper template. *Auton. Robot.*, 30:217–231, 2011.
- [5] M. Ankarali, E. Sayginer, Y. Yazicioglu, A. Saranli, and U. Saranli. A dynamic model of running with a half-circular compliant leg. In *Adaptive Mobile Robotics: Proceedings of the 15th International Conference on Climbing and*

## BIBLIOGRAPHY

- Walking Robots and the Support Technologies for Mobile Machines, Baltimore, USA, 23-26 July, 2012*, page 425. World Scientific, 2012.
- [6] M. M. Ankarali and N. J. Cowan. System identification of rhythmic hybrid dynamical systems via discrete time harmonic transfer functions. In *Proc IEEE Int Conf on Decision Control*, Los Angeles, CA, USA, December 2014.
- [7] M. M. Ankarali, N. J. Cowan, and U. Saranli. Td-slip: A better predictive model for human running. In *Dynamic Walking*, Pensacola, FL, USA, May 2012.
- [8] M. M. Ankarali and U. Saranli. Stride-to-stride energy regulation for robust self-stability of a torque-actuated dissipative spring-mass hopper. *Chaos*, 20(3), Sep. 2010.
- [9] M. M. Ankarali, S. Sefati, M. S. Madhav, A. Long, A. J. Bastian, and N. J. Cowan. Walking dynamics are symmetric (enough). *Submitted to the Journal of the Royal Society Interface. Preprint arXiv:1407.8541*, 2014.
- [10] M. M. Ankarali, H. T. Şen, A. De, A. M. Okamura, and N. J. Cowan. Haptic feedback enhances rhythmic motor control by reducing variability, not improving convergence rate. *J Neurophysiol*, 111(6):1286–1299, 2014.
- [11] M. M. Ankarali, H. T. Sen, A. M. Okamura, and N. J. Cowan. Role of haptic

## BIBLIOGRAPHY

- feedback in a rhythmic task: Paddle juggling. In *JHU Sensorimotor Research Day*, 2011.
- [12] M. M. Ankarali, H. T. Sen, A. M. Okamura, and N. J. Cowan. Haptic feedback enhances rhythmic motor control performance. In *The Society for Neuroscience*, 2012.
- [13] S. Arlot and A. Celisse. A survey of cross-validation procedures for model selection. *Statistics Surveys*, 4:40–79, 2010.
- [14] A. Arsenault, D. Winter, and R. Marteniuk. Is there a ‘normal’ profile of emg activity in gait? *Medical and Biological Engineering and Computing*, 24(4):337–343, 1986.
- [15] M. Athans. The role and use of the stochastic linear-quadratic-gaussian problem in control system design. *IEEE Trans Autom Control*, 16(6):529–552, 1971.
- [16] S. Balakrishnan and A. Thornton-Trump. Integral parameters in human locomotion. In *Proceeding of the Second Biannual Conference of the Canadian Society for Biomechanics, Human Locomotion II*, pages 12–3, 1982.
- [17] J. L. Barclay, A. H. Tsang, and H. Oster. Interaction of central and peripheral clocks in physiological regulation. *Prog. Brain. Res.*, 199:163–181, 2012.
- [18] M. M. Bienkiewicz, M. W. Rodger, and C. M. Craig. Timekeeping strategies

## BIBLIOGRAPHY

- operate independently from spatial and accuracy demands in beat-interception movements. *Exp Brain Res*, 222(3):241–253, 2012.
- [19] R. Blickhan and R. J. Full. Similarity in multilegged locomotion: Bouncing like a monopode. *J Comp Physiol A*, 173(5):509–517, 1993.
- [20] G. E. P. Box and N. R. Draper. *Empirical Model-Building and Response Surfaces*. Wiley, 1987.
- [21] M. Buehler, R. Battaglia, A. Cocosco, G. Hawker, J. Sarkis, and K. Yamazaki. Scout: A simple quadruped that walks, climbs, and runs. In *IEEE International Conference on Robotics and Automation*, volume 2, pages 1707–1712. IEEE, 1998.
- [22] M. Buehler, D. E. Koditschek, and P. J. Kindlmann. Planning and control of robotic juggling and catching tasks. *Int J Robot Res*, 13(2):101–118, 1994.
- [23] M. Buhler, D. E. Koditschek, and P. J. Kindlmann. A family of robot control strategies for intermittent dynamical environments. *IEEE Contr Syst Mag*, 10(2):16–22, 1990.
- [24] D. V. Buonomano and U. R. Karmarkar. How do we tell time? *The Neuroscientist*, 8(1):42–51, 2002.
- [25] S. Burden, S. Revzen, and S. S. Sastry. Dimension reduction near periodic orbits

## BIBLIOGRAPHY

- of hybrid systems. In *Decision and Control and European Control Conference (CDC-ECC), 2011 50th IEEE Conference on*, pages 6116–6121. IEEE, 2011.
- [26] S. A. Burden, S. Revzen, and S. S. Sastry. Model reduction near periodic orbits of hybrid dynamical systems. *arXiv preprint arXiv:1308.4158*, 2013.
- [27] K. Byl and R. Tedrake. Metastable walking machines. *Int J Robot Res*, 28(8):1040–1064, 2009.
- [28] S. Carlsöö, A. Dahlöf, and J. Holm. Kinetic analysis of the gait in patients with hemiparesis and in patients with intermittent claudication. *Scandinavian journal of rehabilitation medicine*, 6(4):166–179, 1973.
- [29] S. G. Carver, N. J. Cowan, and J. M. Guckenheimer. Lateral stability of the spring-mass hopper suggests a two step control strategy for running. *Chaos*, 19(2), 2009.
- [30] S. G. Carver, E. S. Fortune, and N. J. Cowan. State-estimation and cooperative control with uncertain time. In *Proc Amer Control Conf*, pages 2990–2995, Washington, DC, USA, June 2013. IEEE.
- [31] S. G. Carver, T. Kiemel, N. J. Cowan, and J. J. Jeka. Optimal motor control may mask sensory dynamics. *Biol Cybern*, 101(1):35–42, 2009. PMC2778031.
- [32] A. Chatterjee, R. Pratap, C. Reddy, and A. Ruina. Persistent passive hopping

## BIBLIOGRAPHY

- and juggling is possible even with plastic collisions. *Int J Robot Res*, 21(7):621–634, 2002.
- [33] C. Chevallereau, J. W. Grizzle, and C.-L. Shih. Asymptotically stable walking of a five-link underactuated 3-d bipedal robot. *IEEE Trans. Robot.*, 25(1):37–50, 2009.
- [34] H. J. Chiel, L. H. Ting, Ö. Ekeberg, and M. J. Hartmann. The brain in its body: motor control and sensing in a biomechanical context. *J Neurosci*, 29(41):12807–12814, 2009.
- [35] J. Chodera. Analysis of gait from footprints. *Physiotherapy*, 60(6):179, 1974.
- [36] J. Chodera and R. Levell. Footprint patterns during walking. *Perspectives in biomedical engineering*, pages 81–90, 1973.
- [37] A. H. Cohen, P. J. Holmes, and R. H. Rand. The nature of the coupling between segmental oscillators of the lamprey spinal generator for locomotion: a mathematical model. *J Math Biol*, 13(3):345–369, 1982.
- [38] J. J. Collins and I. N. Stewart. Coupled nonlinear oscillators and the symmetries of animal gaits. *J. Nonlinear Science*, 3:349–392, 1993.
- [39] S. Collins, A. Ruina, R. Tedrake, and M. Wisse. Efficient bipedal robots based on passive-dynamic walkers. *Science*, 307(5712):1082–5, Feb. 2005.

## BIBLIOGRAPHY

- [40] N. J. Cowan, M. M. Ankarali, J. P. Dyhr, M. S. Madhav, E. Roth, S. Sefati, S. Sponberg, S. A. Stamper, E. S. Fortune, and T. L. Daniel. Feedback control as a framework for understanding tradeoffs in biology. *Integr Comp Biol*, 54(2):223–237, June 2014.
- [41] N. J. Cowan and E. S. Fortune. The critical role of locomotion mechanics in decoding sensory systems. *J Neurosci*, 27(5):1123–1128, 2007.
- [42] A. Crowe, P. Schiereck, R. de Boer, and W. Keessen. Characterization of gait of young adult females by means of body centre of mass oscillations derived from ground reaction forces. *Gait & Posture*, 1(1):61–68, 1993.
- [43] A. Crowe, P. Schiereck, R. De Boer, and W. Keessen. Characterization of human gait by means of body center of mass oscillations derived from ground reaction forces. *Biomedical Engineering, IEEE Transactions on*, 42(3):293–303, 1995.
- [44] N. Dale and F. Kuenzi. Ionic currents, transmitters and models of motor pattern generators. *Curr Opin Neurobiol*, 7(6):790–796, 1997.
- [45] V. Damholt and N. Termansen. Asymmetry of plantar flexion strength in the foot. *Acta orthopaedica*, 49(2):215–219, 1978.
- [46] A. De and D. E. Koditschek. The penn jerboa: A platform for exploring parallel composition of templates. *arXiv preprint arXiv:1502.05347*, 2015.

## BIBLIOGRAPHY

- [47] A. de Rugy, K. Wei, H. Müller, and D. Sternad. Actively tracking “passive” stability in a ball bouncing task. *Brain Res.*, 982(1):64–78, 2003.
- [48] M. H. Dickinson, C. T. Farley, R. J. Full, M. R. Koehl, R. Kram, and S. L. Lehman. How animals move: An integrative view. *Science*, 288(5463):100–106, 2000.
- [49] J. M. Donelan, R. Kram, and A. D. Kuo. Mechanical work for step-to-step transitions is a major determinant of the metabolic cost of human walking. *J Exp Biol*, 205(Pt 23):3717–3727, Dec. 2002.
- [50] V. Duindam and S. Stramigioli. Modeling and analysis of walking robots. In *Modeling and Control for Efficient Bipedal Walking Robots*, pages 93–127. Springer, 2009.
- [51] D. M. Eagleman. Human time perception and its illusions. *Curr Opin Neurobiol*, 18(2):131–136, 2008.
- [52] B. Efron. Estimating the error rate of a prediction rule: improvement on cross-validation. *J. Am. Statist. Assoc.*, 78(382):316–331, 1983.
- [53] B. Efron. The estimation of prediction error. *J. Am. Statist. Assoc.*, 99(467), 2004.
- [54] B. Efron and R. Tibshirani. Improvements on cross-validation: the 632+ bootstrap method. *J. Am. Statist. Assoc.*, 92(438):548–560, 1997.

## BIBLIOGRAPHY

- [55] M. T. Elliott, A. M. Wing, and A. E. Welchman. Multisensory cues improve sensorimotor synchronisation. *Eur J Neurosci*, 31(10):1828–1835, 2010.
- [56] M. O. Ernst and M. S. Banks. Humans integrate visual and haptic information in a statistically optimal fashion. *Nature*, 415(6870):429–433, 2002.
- [57] J. M. Finley, A. J. Bastian, and J. S. Gottschall. Learning to be economical: the energy cost of walking tracks motor adaptation. *J. Physiol.*, 591(4):1081–1095, 2013.
- [58] J. R. Finnerty, K. Pang, P. Burton, D. Paulson, and M. Q. Martindale. Origins of bilateral symmetry: Hox and dpp expression in a sea anemone. *Science*, 304(5675):1335–1337, 2004.
- [59] W. Forczek and R. Staszkievicz. An evaluation of symmetry in the lower limb joints during the able-bodied gait of women and men. *Journal of human kinetics*, 35(December):47–57, Dec. 2012.
- [60] B. A. Forsyth and K. E. Maclean. Predictive haptic guidance: intelligent user assistance for the control of dynamic tasks. *IEEE Trans. Vis. Comput. Graphics*, 12(1):103–113, 2006.
- [61] R. J. Full and D. E. Koditschek. Templates and anchors: neuromechanical hypotheses of legged locomotion on land. *J Exp Biol*, 202(23):3325–3332, 1999.

## BIBLIOGRAPHY

- [62] R. J. Full, T. M. Kubow, J. Schmitt, P. Holmes, and D. E. Koditschek. Quantifying dynamic stability and maneuverability in legged locomotion. *Integr Comp Biol*, 42(1):149–157, 2002.
- [63] R. J. Full and M. S. Tu. Mechanics of six-legged runners. *J Exp Biol*, 148:129–146, 1990.
- [64] K. Galloway, J. Clark, M. Yim, and D. Koditschek. Experimental investigations into the role of passive variable compliant legs for dynamic robotic locomotion. In *IEEE International Conference on Robotics and Automation*, pages 1243–1249, May 2011.
- [65] K. C. Galloway, G. C. Haynes, B. D. Ilhan, A. M. Johnson, R. Knopf, G. Lynch, B. Plotnick, M. White, and D. E. Koditschek. X-rhex: A highly mobile hexapedal robot for sensorimotor tasks. Technical report, University of Pennsylvania, 2010.
- [66] M. Garcia, A. Chatterjee, A. Ruina, and M. Coleman. The simplest walking model: Stability, complexity and scaling. *J Biomech Eng-T ASME*, 120(2):281–288, 1998.
- [67] H. Geyer, A. Seyfarth, and R. Blickhan. Spring-mass running: simple approximate solution and application to gait stability. *J Theor Biol*, 232(3):315–328, 2005.

## BIBLIOGRAPHY

- [68] H. Geyer, A. Seyfarth, and R. Blickhan. Compliant leg behaviour explains basic dynamics of walking and running. *Proceedings of the Royal Society B: Biological Sciences*, 273(1603):2861–2867, 2006.
- [69] R. M. Ghigliazza, R. Altendorfer, P. Holmes, and D. E. Koditschek. A simply stabilized running model. *SIAM J. on Applied Dynamical Systems*, 2003.
- [70] G. Giakas and V. Baltzopoulos. Time and frequency domain analysis of ground reaction forces during walking: an investigation of variability and symmetry. *Gait & Posture*, 5(3):189–197, 1997.
- [71] J. W. Grizzle, G. Abba, and F. Plestan. Asymptotically stable walking for biped robots: Analysis via systems with impulse effects. *IEEE Trans Autom Control*, 46(1):51–64, 2001.
- [72] J. Guckenheimer and P. Holmes. *Nonlinear Oscillations, Dynamical Systems, and Bifurcations of Vector Fields*. Springer, 1991.
- [73] J. M. Guckenheimer. Isochrons and phaseless sets. *J Math Biol*, 1:259–273, 1975.
- [74] J. M. Guckenheimer. A robust hybrid stabilization strategy for equilibria. *IEEE Trans Autom Control*, 40(2):321–326, 1995.
- [75] J. M. Guckenheimer and P. J. Holmes. *Nonlinear Oscillations, Dynamical Systems, and Bifurcations of Vector Fields*. Springer-Verlag, New York, USA, 1983.

## BIBLIOGRAPHY

- [76] J. M. Guckenheimer and S. Johnson. Planar hybrid systems. In *Hybrid Systems II*, volume 999 of *Lect. Notes. Comput. Sc.*, pages 202–225. Springer Berlin / Heidelberg, 1995.
- [77] L. A. Gundersen, D. R. Valle, A. E. Barr, J. V. Danoff, S. J. Stanhope, and L. Snyder-Mackler. Bilateral analysis of the knee and ankle during gait: an examination of the relationship between lateral dominance and symmetry. *Physical therapy*, 69(8):640–50, Aug. 1989.
- [78] O. Gur and U. Saranlı. Model-based proprioceptive state estimation for spring-mass running. In *Robotics: Science and Systems VII*, pages 105–112, 2012.
- [79] J. Hamill, B. Bates, and K. Knutzen. Ground reaction force symmetry during walking and running. *Research Quarterly for Exercise and Sport*, 55(3):289–293, 1984.
- [80] R. Hannah, J. Morrison, and A. Chapman. Kinematic symmetry of the lower limbs. *Archives of physical medicine and rehabilitation*, 65(4):155–158, 1984.
- [81] C. Harris and D. Wolpert. Signal-dependent noise determines motor planning. *Nature*, 394(6695):780–784, 1998.
- [82] R. M. Harris-Warrick and A. H. Cohen. Serotonin modulates the central pattern generator for locomotion in the isolated lamprey spinal cord. *J Exp Biol*, 116:27–46, 1985.

## BIBLIOGRAPHY

- [83] T. L. Hedrick and A. K. Robinson. Within-wingbeat damping: dynamics of continuous free-flight yaw turns in *manduca sexta*. *Biol Letters*, 6(3):422–425, 2010.
- [84] W. Herzog, B. M. Nigg, L. J. Read, and E. Olsson. Asymmetries in ground reaction force patterns in normal human gait. *Medicine and science in sports and exercise*, 21(1):110–4, Feb. 1989.
- [85] P. J. Holmes. Poincaré, celestial mechanics, dynamical-systems theory and “chaos”. *Phys. Rep.*, 193:137–163, September 1990.
- [86] P. J. Holmes, R. J. Full, D. E. Koditschek, and J. Guckenheimer. The dynamics of legged locomotion: Models, analyses, and challenges. *SIAM Rev*, 48(2):207–304, 2006.
- [87] E. T. Hsiao-Wecksler, J. D. Polk, K. S. Rosengren, J. J. Sosnoff, and S. Hong. A review of new analytic techniques for quantifying symmetry in locomotion. *Symmetry*, 2(2):1135–1155, 2010.
- [88] F. C. Huang, R. B. Gillespie, and A. D. Kuo. Visual and haptic feedback contribute to tuning and online control during object manipulation. *J Motor Behav*, 39(3):179–193, 2007.
- [89] S. Hwang. *Frequency domain system identification of helicopter rotor dynamics*

## BIBLIOGRAPHY

- incorporating models with time periodic coefficients*. PhD thesis, University of Maryland College Park, 1997.
- [90] A. J. Ijspeert. Central pattern generators for locomotion control in animals and robots: a review. *Neural Networks*, 21(4):642–653, 2008.
- [91] A. J. Ijspeert, A. Crespi, D. Ryczko, and J.-M. Cabelguen. From swimming to walking with a salamander robot driven by a spinal cord model. *Science*, 315(5817):1416–1420, 2007.
- [92] K. Karamanidis, A. Arampatzis, and G. P. Bruggemann. Symmetry and reproducibility of kinematic parameters during various running techniques. *Med. Sci. Sports. Exerc.*, 35(6):1009–1016, 2003.
- [93] T. Kiemel, D. Logan, and J. J. Jeka. Using perturbations to probe the neural control of rhythmic movements, 2014. In preperation.
- [94] T. Kiemel, Y. Zhang, and J. Jeka. Identification of neural feedback for upright stance in humans: stabilization rather than sway minimization. *J Neurosci*, 31(42):15144–15153, 2011.
- [95] D. E. Koditschek, R. J. Full, and M. Buehler. Mechanical aspects of legged locomotion control. *Arthropod Structure & Development*, 33:251–272, 2004.
- [96] R. Kohavi. A study of cross-validation and bootstrap for accuracy estimation

## BIBLIOGRAPHY

- and model selection. In *Proc. of the Int. Joint Conf. on Artificial Intelligence*, volume 14, pages 1137–1145, 1995.
- [97] A. D. Kuo. The relative roles of feedforward and feedback in the control of rhythmic movements. *Motor Control*, 6(2):129–145, 2002.
- [98] A. D. Kuo. An optimal state estimation model of sensory integration in human postural balance. *J Neural Eng*, 2(3):235–249, 2005.
- [99] A. D. Kuo, J. M. Donelan, and A. Ruina. Energetic consequences of walking like an inverted pendulum: step-to-step transitions. *Exerc. Sport Sci. Rev.*, 33(2):88–97, 2005.
- [100] K.-A. Lai, C.-J. Lin, I. Jou, F.-C. Su, et al. Gait analysis after total hip arthroplasty with leg-length equalization in women with unilateral congenital complete dislocation of the hip—comparison with untreated patients. *Journal of orthopaedic research*, 19(6):1147–1152, 2001.
- [101] A. Lamperski and N. J. Cowan. Time-changed linear quadratic regulators. In *Proc Euro Control Conf*, Zurich, Switzerland, July 2013.
- [102] A. Lamperski and N. J. Cowan. Optimal control with noisy time. *IEEE Trans Autom Control*, 2014. Accepted; Preprint available at <http://arxiv.org/abs/1401.0202>.
- [103] R. L. Lathrop-Lambach, J. L. Asay, S. T. Jamison, X. Pan, L. C. Schmitt,

## BIBLIOGRAPHY

- K. Blazek, R. a. Siston, T. P. Andriacchi, and A. M. W. Chaudhari. Evidence for joint moment asymmetry in healthy populations during gait. *Gait & posture*, 40(4):526–31, Sept. 2014.
- [104] S. M. LaValle and M. B. Egerstedt. On time: Clocks, chronometers, and open-loop control. In *Proceedings of the 46th IEEE Conference on Decision and Control*, pages 1916–1922, 2007.
- [105] H. Law. Microcomputer-based low-cost method for measurement of spatial and temporal parameters of gait. *Journal of biomedical engineering*, 9(2):115–120, 1987.
- [106] J. Lee, S. N. Sponberg, O. Y. Loh, A. G. Lamperski, R. J. Full, and N. J. Cowan. Templates and anchors for antenna-based wall following in cockroaches and robots. *IEEE Trans Robot*, 24(1):130–143, Feb. 2008.
- [107] P.-C. Lin, H. Komsuoglu, and D. E. Koditschek. A leg configuration measurement system for full-body pose estimates in a hexapod robot. *IEEE Trans Robot*, 21(3):411–422, 2005.
- [108] L. Ljung. *System Identification: Theory for the User*. Prentice-Hall, Englewood Cliffs, NJ, second edition, 1999.
- [109] M. S. Madhav, S. A. Stamper, E. S. Fortune, and N. J. Cowan. Closed-loop

## BIBLIOGRAPHY

- stabilization of the jamming avoidance response reveals its locally unstable and globally nonlinear dynamics. *J Exp Biol*, 216(22):4272–4284, 2013.
- [110] R. A. Mann and J. Hagy. Biomechanics of walking, running, and sprinting. *Am. J. Sports Med.*, 8(5):345–350, 1980.
- [111] M. Marks and G. G. Hirschberg. Analysis of the hemiplegic gait. *Annals of the New York Academy of Sciences*, 74(1):59–77, 1958.
- [112] S. J. Mattes, P. E. Martin, and T. D. Royer. Walking symmetry and energy cost in persons with unilateral transtibial amputations: matching prosthetic and intact limb inertial properties. *Arch. Phys. Med. Rehabil.*, 81(5):561–568, 2000.
- [113] T. McGeer. Passive bipedal running. *Proc R Soc B*, 240(1297):107–134, 1990.
- [114] M. R. Menard, M. E. McBride, D. J. Sanderson, and D. D. Murray. Comparative biomechanical analysis of energy-storing prosthetic feet. *Arch Phys Med Rehabil*, 73(5):451–58, 1992.
- [115] J. G. Milton, J. L. Cabrera, T. Ohira, S. Tajima, Y. Tonosaki, C. W. Eurich, and S. A. Campbell. The time-delayed inverted pendulum: implications for human balance control. *Chaos*, 19(2), 2009.
- [116] J. G. Milton, T. Ohira, J. L. Cabrera, R. M. Fraiser, J. B. Gyorffy, F. K. Ruiz, M. A. Strauss, E. C. Balch, P. J. Marin, and J. L. Alexander. Balancing with

## BIBLIOGRAPHY

- vibration: a prelude for drift and act balance control. *PLoS One*, 4(10):e7427, 2009.
- [117] E. Möllerstedt. *Dynamic analysis of harmonics in electrical systems*. PhD thesis, Department of Automatic Control, Lund Institute of Technology, 2000.
- [118] A. Morice, I. Siegler, B. Bardy, and W. Warren. Learning new perception-action solutions in virtual ball bouncing. *Exp Brain Res*, 181:249–265, 2007.
- [119] G. D. Muir and I. Q. Whishaw. Complete locomotor recovery following corticospinal tract lesions: measurement of ground reaction forces during overground locomotion in rats. *Behav. Brain. Res*, 103(1):45–53, 1999.
- [120] B. Mulloney and C. Smarandache. Fifty years of CPGs: Two neuroethological papers that shaped the course of neuroscience. *Front. Behav. Neurosci.*, 4(45), 2010.
- [121] S. M. O’Connor and J. M. Donelan. Fast visual prediction and slow optimization of preferred walking speed. *J Neurophysiol*, 107(9):2549–2559, 2012.
- [122] S. Öunpuu and D. A. Winter. Bilateral electromyographical analysis of the lower limbs during walking in normal adults. *Electroencephalography and clinical neurophysiology*, 72(5):429–438, 1989.
- [123] P. Pourcelot, F. Audigie, C. Degueurce, J. Denoix, and D. Geiger. Kinematic

## BIBLIOGRAPHY

- symmetry index: a method for quantifying the horse locomotion symmetry using kinematic data. *Vet. Res.*, 28(6):525, 1997.
- [124] J. Pratt and R. Tedrake. Velocity-based stability margins for fast bipedal walking. In M. Diehl and K. Mombaur, editors, *Fast Motions in Biomechanics and Robotics*, volume 340 of *Lecture Notes in Control and Information Sciences*, pages 299–324. Springer Berlin / Heidelberg, 2006.
- [125] C. Rao and Y. Wu. Linear model selection by cross-validation. *J. Statist. Plann. Inference*, 128(1):231–240, 2005.
- [126] D. S. Reisman, R. Wityk, K. Silver, and A. J. Bastian. Locomotor adaptation on a split-belt treadmill can improve walking symmetry post-stroke. *Brain*, 130(7):1861–1872, July 2007.
- [127] S. Revzen. *Neuromechanical Control Architectures of Arthropod Locomotion*. PhD thesis, University of California, Berkeley, 2009.
- [128] S. Revzen and J. M. Guckenheimer. Estimating the phase of synchronized oscillators. *Phys Rev E*, 78(5 Pt 1):051907–051918, 2008.
- [129] S. Revzen and J. M. Guckenheimer. Finding the dimension of slow dynamics in a rhythmic system. *J. R. Soc. Interface*, 9(70):957–971, 2011.
- [130] R. Ronsse and D. Sternad. Bouncing between model and data: Stability, passivity, and optimality in hybrid dynamics. *J Motor Behav*, 42(6):389–399, 2010.

## BIBLIOGRAPHY

- [131] R. Ronsse, K. Wei, and D. Sternad. Optimal control of a hybrid rhythmic-discrete task: The bouncing ball revisited. *J Neurophysiol*, 103(5):2482–2493, 2010.
- [132] E. Roth, S. Sponberg, and N. J. Cowan. A comparative approach to closed-loop computation. *Curr Opin Neurobiol*, 25:54–62, April 2014.
- [133] H. Sadeghi, P. Allard, F. Prince, and H. Labelle. Symmetry and limb dominance in able-bodied gait: a review. *Gait & Posture*, 12(1):34–45, Sept. 2000.
- [134] U. Saranli, O. Arslan, M. M. Ankarali, and O. Morgul. Approximate analytic solutions to non-symmetric stance trajectories of the passive spring-loaded inverted pendulum with damping. *Nonlinear Dynam.*, 62(4):729–742, 2010.
- [135] U. Saranli, A. Avci, and M. ztrk. A modular real-time fieldbus architecture for mobile robotic platforms. *Instrumentation and Measurement, IEEE Transactions on*, 60(3):916–927, 2011.
- [136] U. Saranli, M. Buehler, and D. E. Koditschek. RHex: A simple and highly mobile hexapod robot. *Int J Robot Res*, 20(7):616–631, 2001.
- [137] S. Schaal, C. G. Atkeson, and D. Sternad. One-handed juggling: A dynamical approach to a rhythmic movement task. *J Motor Behav*, 28(2):165–183, 1996.
- [138] S. Schaal, P. Mohajjerian, and A. Ijspeert. Dynamics systems vs. optimal control—a unifying view. *Prog Brain Res*, 165:425–445, 2007.

## BIBLIOGRAPHY

- [139] S. Schaal, D. Sternad, R. Osu, and M. Kawato. Rhythmic arm movement is not discrete. *Nat. Neurosci.*, 7(10):1136–1143, 2004.
- [140] W. J. Schwind and D. E. Koditschek. Approximating the stance map of a 2-dof monoped runner. *J. Nonlinear Science*, 10(5):533–568, 2000.
- [141] A. Seyfarth, H. Geyer, and H. Herr. Swing-leg retraction: a simple control model for stable running. *J Exp Biol*, 206:2547–2555, Aug. 2003.
- [142] M. Sfakiotakis, D. M. Lane, and J. B. C. Davies. Review of fish swimming modes for aquatic locomotion. *IEEE J Ocean Eng*, 24(2):237–252, 1999.
- [143] R. Shadmehr, J. J. O. de Xivry, M. Xu-Wilson, and T.-Y. Shih. Temporal discounting of reward and the cost of time in motor control. *J Neurosci*, 30(31):10507–10516, 2010.
- [144] R. Shadmehr and J. W. Krakauer. A computational neuroanatomy for motor control. *Exp Brain Res*, 185(3):359–381, 2008.
- [145] J. Shao. Linear model selection by cross-validation. *J. Am. Statist. Assoc.*, 88(422):486–494, 1993.
- [146] J. Shao. Bootstrap model selection. *J. Am. Statist. Assoc.*, 91(434):655–665, 1996.
- [147] I. Siegler, B. G. Bardy, and W. H. Warren. Passive vs. active control of rhyth-

## BIBLIOGRAPHY

- mic ball bouncing: the role of visual information. *J. Exp. Psychol. Human*, 36(3):729–50, 2010.
- [148] I. Siegler, C. Bazile, and W. H. Warren. Mixed control for perception and action: timing and error correction in rhythmic ball-bouncing. *Exp Brain Res*, pages 1–13, 2013.
- [149] T. Söderström and P. Stoica. *System Identification*. Systems and Control Engineering. Prentice Hall International, 1989. Out of print.
- [150] J. C. Spagna, D. I. Goldman, P.-C. Lin, D. E. Koditschek, and R. J. Full. Distributed mechanical feedback in arthropods and robots simplifies control of rapid running on challenging terrain. *Bioinspiration & Biomimetics*, 2(1):9–18, 2007.
- [151] D. J. Stefanyshyn and J. R. Engsberg. Right to left differences in the ankle joint complex range of motion. *Medicine and science in sports and exercise*, 26(5):551–555, 1994.
- [152] D. Sternad, M. Duarte, H. Katsumata, and S. Schaal. Dynamics of a bouncing ball in human performance. *Phys. Rev. E. Stat. Nonlin. Soft Matter Phys.*, 63(1):011902, Jan. 2001.
- [153] B. E. Studenka, H. N. Zelaznik, and R. Balasubramaniam. The distinction between tapping and circle drawing with and without tactile feedback: An

## BIBLIOGRAPHY

- examination of the sources of timing variance. *Q. J. Exp. Psychol.*, 65(6):1086–1100, 2012.
- [154] P. Talkner, P. Hiinggi, E. Freidkin, and D. Trautmann. Discrete dynamics and metastability: Mean first passage times and escape rates. *J. Stat. Phys.*, 48:231–254, 1987.
- [155] E. Todorov. Stochastic optimal control and estimation methods adapted to the noise characteristics of the sensorimotor system. *Neural Comput*, 17(5):1084–1108, 2005.
- [156] E. Todorov and M. I. Jordan. Optimal feedback control as a theory of motor coordination. *Nature Neuroscience*, 2002.
- [157] N. B. Tufillaro and A. M. Albano. Chaotic dynamics of a bouncing ball. *Am. J. Phys.*, 54:939–944, Oct. 1986.
- [158] E. D. Tytell, P. J. Holmes, and A. H. Cohen. Spikes alone do not behavior make: why neuroscience needs biomechanics. *Curr Opin Neurobiol*, 21(5):816–822, 2011.
- [159] J. Van der Straaten and P. Scholton. Symmetry and periodicity in gait patterns of normal and hemiplegic children. In *Biomechanics VI: proceedings of the Sixth International Congress of Biomechanics, Copenhagen, Denmark*, volume 1, page 287. University Park Press, 1978.

## BIBLIOGRAPHY

- [160] C. L. Vaughan. Are joint torques the Holy Grail of human gait analysis? *Human Movement Science*, 15(3):423–443, 1996.
- [161] M. Venkadesan, J. Guckenheimer, and F. J. Valero-Cuevas. Manipulating the edge of instability. *J Biomech*, 40(8):1653–1661, 2007.
- [162] K. Wei, T. M. H. Dijkstra, and D. Sternad. Passive stability and active control in a rhythmic task. *J Neurophysiol*, 98(5):2633–2646, 2007.
- [163] K. Wei, T. M. H. Dijkstra, and D. Sternad. Stability and variability: Indicators for passive stability and active control in a rhythmic task. *J Neurophysiol*, 99(6):3027–3041, 2008.
- [164] J. Weingarten, G. A. D. Lopes, M. Buehler, R. E. Groff, and D. Koditschek. Automated gait adaptation for legged robots. In *IEEE International Conference on Robotics and Automation*, volume 3, pages 2153–2158, April 2004.
- [165] E. Wendel and A. D. Ames. Rank deficiency and superstability of hybrid systems. *Nonlinear Analysis: Hybrid Systems*, 6(2):787–805, 2012.
- [166] N. M. Wereley. *Analysis and Control of Linear Periodically Time Varying Systems*. PhD thesis, Massachusetts Institute of Technology, 1990.
- [167] E. Westervelt, J. Grizzle, and D. Koditschek. Hybrid zero dynamics of planar biped walkers. *IEEE Trans. Automat. Contr.*, 48(1):42–56, January 2003.

## BIBLIOGRAPHY

- [168] A. M. Wing, M. Dumas, and A. E. Welchman. Combining multisensory temporal information for movement synchronisation. *Exp Brain Res*, 200(3-4):277–282, 2010.
- [169] J.-i. Yamanishi, M. Kawato, and R. Suzuki. Studies on human finger tapping neural networks by phase transition curves. *Biol Cybern*, 33:199–208, 1979.
- [170] Y. Yang. Consistency of cross validation for comparing regression procedures. *Ann. Stat.*, pages 2450–2473, 2007.
- [171] A. Zavala-Rio and B. Brogliato. Direct adaptive control design for one-degree-of-freedom complementary-slackness jugglers. *Automatica*, 37(7):1117–1123, 2001.

# Vita



M. Mert Ankaral received his B.Sc. degree in Mechanical Engineering and minor certificate in Mechatronics from the Middle East Technical University, Turkey in 2007, and 2008, respectively. He received his M.Sc. degree in Electrical & Electronics Engineering from METU in 2010. Throughout his M.Sc. studies at METU, he worked on developing high-performance control algorithms, physically realistic simulations, and analytical models for dynamically capable legged robotic platforms under the supervisions of Dr. Afsar Saranli and Dr. Uluc Saranli. Manu joined Dr. Noah Cowan's Locomotion in Mechanical and Biological Systems (LIMBS) lab to pursue his Ph.D. in 2010. His research at Hopkins has been devoted to discovering the mechanisms by which the human nervous system controls rhythmic dynamical behaviors. In 2012, Mert received the Creel Family Teaching award, which recognizes the best teaching assistants in Mechanical Engineering. He was also named to the 2015 class of Siebel Scholars which is awarded

## VITA

annually for academic excellence and demonstrated leadership to 85 top students from worlds leading graduate schools.